國　立　清　華　大　學

博　士　論　文

應用於高效率小型風力發電系統之新型無感測式最大功率追蹤控制器

A NOVEL SENSORLESS MPPT CONTROLLER FOR A HIGH EFFICIENCY SMALL-SCALE WIND POWER GENERATION SYSTEM

系所別：電機工程學系博士　　組別：電力組

學號姓名：927901 阮昱霖 (Yu-Ling Juan)

指導教授：潘晴財 博士 (Prof. Ching-Tsai Pan)

中　華　民　國　九　十　九　年　一　月

中文摘要

在現行的小型風力發電系統中，大多採用由二極體整流器與直流轉換器所組成的二級式交直流轉換器。其主要缺點為在發電機側將會產生嚴重的電流諧波失真，其不僅會降低效率亦會對風力機造成額外的機械應力進而產生擾人的機械噪音。此外，在現有的最大功率控制法中，最佳轉矩控制法廣泛應用於小型風力發電系統中。但其只考量到系統於穩態下之情況，並未考慮於風速變化下之系統動態特性。因此，在風速快速變化時，由於機械轉動慣量所造成的緩慢動態響應便會減少風力機的發電量。為了克服上述的缺點且在兼顧發電效能與成本考量下，本論文提出一新型無感測式最大功率追蹤控制器及一高效率單級式交直流轉換器。主要的貢獻可摘要如下：

首先提出一新型無感測式動態最佳轉矩最大功率追蹤控制器，其中利用所提的虛擬慣量調整法來改善風力機的動態響應進而增加其發電量。接著為改善電力品質及轉換效率，本論文提出一高效率單級式交直流轉換器來取代習用的二級式交直流轉換器。如此不僅可將發電機電流的總諧波失真大大的降低至約 5%以下，同時也減小了風力機的機械應力與擾人的噪音。隨後本論文更提出一半同步整流技術來進一步降低由背接二極體所造成的導通損。另外，為了更進一步降低於不連續導通控制法下開關的切換損失，本論文遂將連續導通控制、不連續導通控制及半同步整流技術整合為一整合式控制法。本論文並實際建構一測試平台用以驗證所提理論之可行性與效能。最後，由實測結果可知本論文所提之系統整體效率能有效提升 12%至 15%，回收年限則能縮短 11%至 13%。

關鍵詞：小型風力發電系統、最大功率追蹤、可調式虛擬慣量、半同步整流

ABSTRACT

A well-known two-stage ac to dc converter composed of a diode bridge rectifier and a dc converter is widely used in the existing small wind power generation system (WPGS). However, due to the nonlinearity of the diode bridge rectifier, there will be significant total harmonics distortion (THD) in the generator currents which will not only reduce the efficiency but also result in additional mechanical stress and undesired acoustic noise. As to the maximum power point tracking (MPPT) controller, the widely adopted optimal torque control algorithm only concerns about the steady state characteristics of the wind turbine. However, the poor dynamic response due to the mechanical inertia effect will result in reduction of the wind turbine efficiency under rapidly changing wind speed situations. To overcome the above disadvantages, a novel sensorless dynamic MPPT controller and a high efficiency single-stage ac to dc converter are proposed in this dissertation as a compromise of both performance and cost for a small WPGS.

Basically, the major contributions of this dissertation can be briefly outlined as follows. First, a novel sensorless dynamic optimal torque MPPT control with adjustable virtual inertia technique is proposed to improve the wind turbine dynamic response and increase the output power. In addition, since the proposed novel MPPT control contains no mechanical sensors, both the reliability and cost performance index can be further improved. Second, a single-stage converter with three active switches is proposed to replace the conventional two-stage converter for improving the power quality and efficiency. The generator current THD is greatly reduced to around 5% which can reduce the corresponding mechanical stress and acoustic noise as well. Third, a novel quasi-synchronous rectification technique is proposed to further reduce the conduction losses of the body diodes. Moreover, a hybrid control composed of partial CCM, partial DCM and QSR techniques is proposed for the corresponding single-stage converter to reduce the losses. From the experimental results, one can see that the total efficiency of the whole system can be increased by 12% to 15% and the payback period is reduced by 11% to 13% approximately.

Keywords: small-scale wind power generation system, maximum power point tracking, adjustable virtual inertia, quasi-synchronous rectification

ACKNOWLEDGEMENTS

I sincerely appreciate my dear advisor Professor Ching-Tsai Pan for his generous guidance, support and encourage throughout this working toward the Ph. D. degree. His way of getting along with people and serious attitude toward scientific research has been a reference model for me.

I would like to express my sincere gratitude to Professor Sheng-Fuu Lin, Professor Ying-Yu Tzou, Professor Pau-Lo Hsu, Professor Chang-Ming Liaw, and Professor Chia-Chi Chu for giving me many helpful comments and suggestions on this dissertation. Their comments make this dissertation more complete.

Special thanks also go to all students studying in Power Electronics Lab at National Tsing Hua University for their aid and encourage. It has been my great pleasure to work with them.

I would also like to thank Professor Tsai-Rong Chen for providing the excellent measurement instrument, Yokogawa precision power analyzer WT3000 to help me complete all the experiments.

In addition, I would like to thank my dear wife, Chieh-Hua Chen, for her great support and patience in the past eight years and my mother, Shu-Mei Lyu, for the parenting grace. Finally, I would like to dedicate this dissertation to all my family.

CONTENTS

LIST OF FIGURES

LIST OF TABLES

CHAPTER 1

INTRODUCTION

1.1 Motivation

Due to the first shock of fossil fuel price in the early 1970s, the renewable energy resources attracted peoples' great attention. Recently, because of the global environmental issues, such as air pollution, acid rain and greenhouse effects, worldwide countries have focused on the research and development of renewable energy systems which are pollution-free and inexhaustible. The wind power generation system (WPGS) converting the wind power into any demanded forms of electricity is one of the most effective renewable power generation systems. For considering about the cost performance index, most of wind power systems are built with large-scale wind turbines. However, in the last decade, small-scale turbines have also become attractive because of low initial cost, easy maintenance and good suitability for distributed power systems, such as individual households and small-scale industries.

In U.K., the application of small-scale wind power generation systems in urban environment has become a new technique industry. According to a recent small wind turbine market study report of made by American Wind Energy Association [1][2], the U.S. small wind turbine market grew 14% since 2006 and about 7000 sets of small wind power systems are purchase in 2006. Presently, in Taiwan, there are about 30 manufacturers of small-scale wind turbine and about 5000 small wind turbines (300W – 5kW) can be produced per year. Therefore, the manufacturers in Taiwan are very competitive in the global small wind turbine market.

However, the common small wind power generation system is usually composed

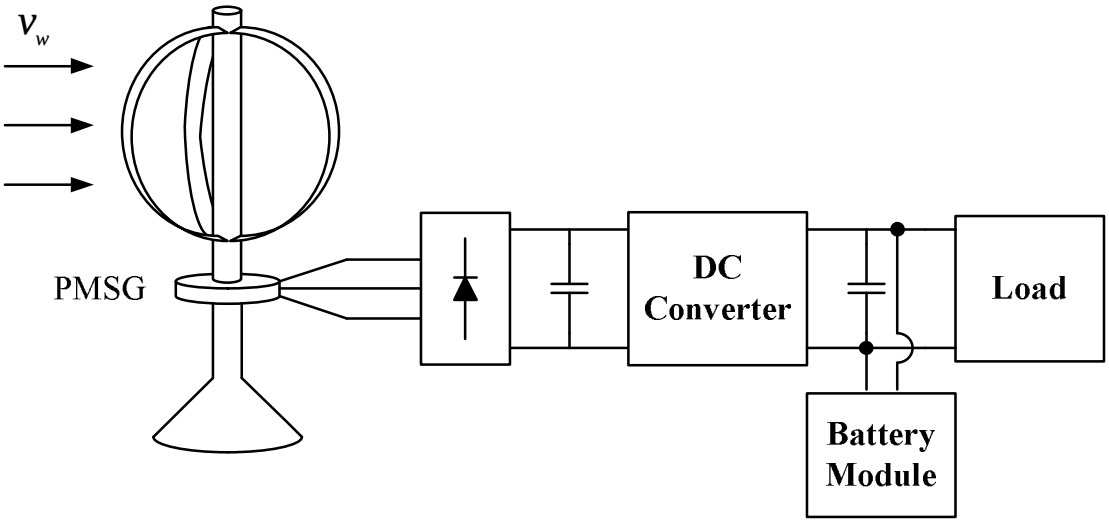

Fig. 1.1 Configuration of a conventional small-scale wind power generation system.

of a fixed pitch wind turbine, a permanent magnet generator, a diode bridge rectifier, a dc converter, a battery power module and a load as shown in Fig. 1.1. In such a conventional configuration, there will be significant harmonic distortion in generator currents which will cause additional power losses, mechanical stress on the shaft and unpleasant acoustic noise. It is also well known that the efficiency of a two-stage converter is always poorer than that of a single-stage converter. Moreover, if a wide-used steady state optimal torque maximum power point tracking (MPPT) control is adopted [3][4], the wind turbine efficiency under rapidly changing wind speed situations will become worse especially in low wind speed range.

Therefore, to overcome the above disadvantages, a high efficiency small wind power generation system with a novel dynamic MPPT control is proposed in this dissertation. The configuration of the proposed small-scale wind power generation system is shown in Fig. 1.2. A single-stage ac to dc converter with only three active switches and three diodes is proposed to replace the conventional two-stage converter for improving current THD and efficiency.

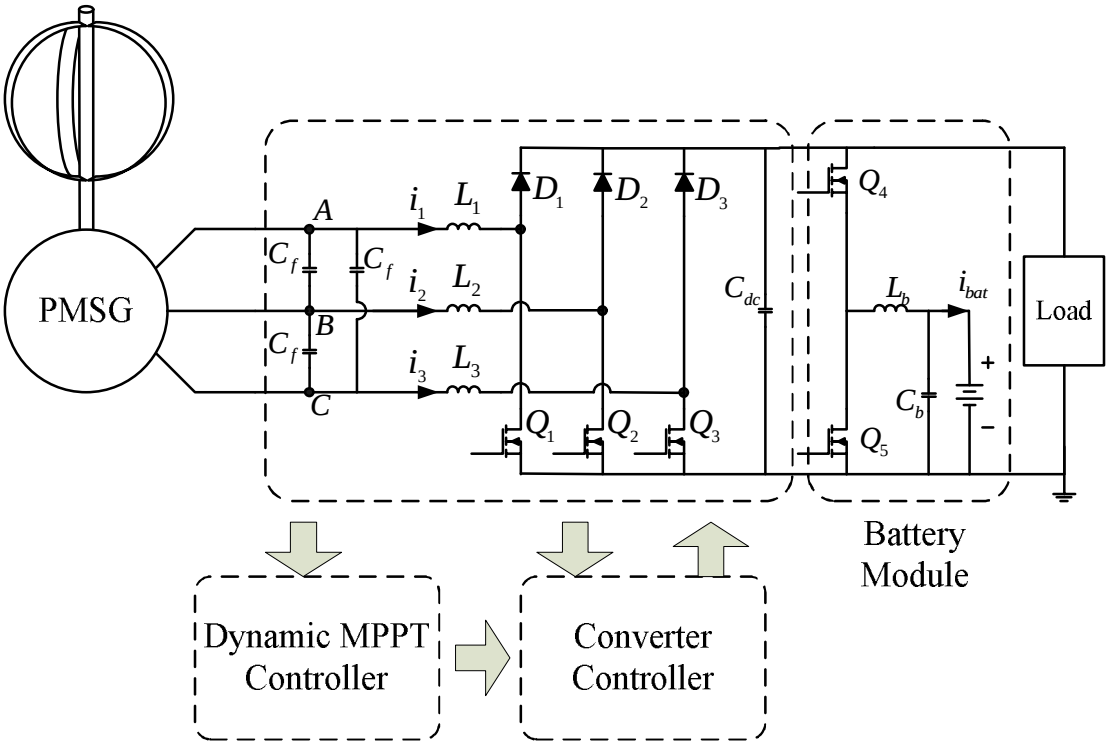

Fig. 1.2 Configuration of the proposed small-scale WPGS.

1.2 Literature Review

The MPPT control is one of the most important issues of the WPGS research. A MPPT control is necessary for maximizing the output power of a wind turbine. Basically, the MPPT techniques can roughly be classified into the following four strategies, namely the tip speed ratio (TSR) control [9], the optimal torque (OT) control [3][4], the power mapping control [5][6], and the perturbation and observation (P&O) searching control [7][8].

For the TSR control, an expensive anemometer is required to achieve maximum output control. As to the OT control strategy, the well known optimal torque, namely kw_m^2, is adopted as the command signal for controlling the generator torque to maximize the output power. Similarly, for the power mapping control, the well know

optimal output power command, namely kw_m^3, is adopted for controlling the generator output power. Practically, the wind velocity is changing all the time. The steady state wind velocity is in fact very unusual. Hence, as the wind speed is either increased or decreased, if the rotor speed of the generator cannot track the variation of the wind speed closely, then the extracted wind energy will be reduced greatly. In fact, to the authors' best knowledge, most existing papers consider only the tracking along the maximum power trajectory of kw_m^3 or the optimal torque trajectory of kw_m^2. Very few papers concern about the effect of the WPGS inertia on the wind energy capturing. As to the P&O control, although it has the advantage of simplicity and flexibility, the oscillating control around the optimal point will certainly sacrifice the efficiency of the WPGS. However, for a micro-scale WPGS, the power coefficient function of the turbine can be measured easily, which enables one to obtain the k-coefficient of the optimal torque. Hence, the mechanical sensorless optimal torque control can be implemented easily to reduce cost.

On the other hand, due to cost reduction consideration, a full diode bridge rectifier is always adopted to convert the three phase ac voltage of the generator into dc voltage [3][5-7]. Then, a dc converter is needed as the second stage to achieve MPPT control. It is well known that the efficiency of a two stage converter is always poorer than a single stage due to the twice power conversions. Moreover, the diode voltage drops and the significant current THD will also reduce the efficiency of the WPGS significantly [15]. Although the full-controlled ac to dc converter can provide greatly power quality and efficiency, its cost is usually much higher than the conventional two-stage converter mentioned above and its control strategy is more complex as well [4][8]. A half-controlled ac to dc converter composed only three active switches and three diodes is simpler and cheaper than the full-controlled ac to dc converter.

However, if the half-controlled converter is operated in CCM, the source currents are still with signification distortions in the negative half cycle [38]. The well-known DCM PFC [20-24] is a simple and effective technique for improving the power quality, but the turn-off switching losses of the active switches cannot be neglected.

In view of the above drawbacks, it is the major motivation of this paper to propose a novel MPPT controller and a QSR single stage ac to dc converter for a small-scale WPGS such that more wind energy can be extracted while the wind speed is under variation and less electrical energy is dissipated in the ac to dc converter with little additional cost. A novel hybrid control is also proposed to reduce the switching losses of the DCM operation. It turns out that with the proposed WPGS, the total generated energy can be increased greatly.

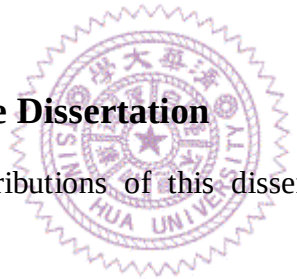

1.3 Contributions of the Dissertation

Basically, the major contributions of this dissertation can be summarized as follows:

(1) Both the reliability and cost performance index are improved because there are no mechanical sensors required, such as anemometers and encoders.

(2) A novel sensorless dynamic optimal torque MPPT control with adjustable virtual inertia technique is proposed to improve the wind turbine dynamic response.

(3) A single-stage converter with three active switches is proposed to replace the conventional two-stage converter for improving the power quality and efficiency.

(4) The total harmonic distortion of generator currents is greatly reduced to around 5% that also results in reductions of mechanical stress and acoustic noise.

(5) A novel quasi-synchronous rectification technique is proposed to further reduce the conduction losses of the body diodes.

(6) A hybrid control is also proposed to reduce the switching losses which is integrated with partial CCM, partial DCM and QSR techniques.

(7) For evaluating the validity and performance of the proposed system, a testing facility is practically constructed to test the implemented prototype system.

(8) The converter efficiency is increased about 6% to 11% depending on the power loading and the amount of extracted wind power can also be increased about 2% to 5% depending on different wind speed variations. As a result, the total efficiency of whole system can then be increased about 12% to 15% and the payback period is reduced about 11% to 13%.

1.4 Configuration of the Dissertation

The contents of this dissertation can be outlined as follows:

In chapter 2, a conventional small wind power generation system is introduced. The characteristics of the wind turbine and generator are first illustrated as a basis. The operational principles of the conventional two-stage converter and the steady state optimal torque maximum power point tracking control are then described as well. Finally, some simulations are carried out for evaluating the performance of the conventional system. It can be seen that the harmonic distortion of generator currents is significant because of the nonlinearity of diode bridge rectifier. Moreover, the dynamic response of the conventional WPGS with steady state optimal torque MPPT controller is poor under wind speed variations.

Therefore, in chapter 3, a novel sensorless dynamic optimal torque MPPT control is proposed. An adjustable virtual inertia technique is integrated to reduce the inertia effect on the mechanical dynamic response. To achieve sensorless control, a

two-phase type PLL which is independent of speed is adopted for estimating the phase and frequency of generator EMFs. Additionally, a reduced-order estimator is used to observe the input torque from the wind turbine instead of using a torque transducer. Finally, from the simulation results given in the last section, it can been seen that the proposed dynamic MPPT control can provide excellent improvement of wind turbine dynamic response and extracted amount of wind power during wind speed variations.

Furthermore, to improve the converter efficiency, a three phase single stage converter with quasi-synchronous rectification technique is proposed in chapter 4. The corresponding duty ratios of the switches operated in DCM control are extended by the proposed QSR technique. The analytic expressions of the duty ratios are derived as well. Moreover, a hybrid control that is integrated with CCM, DCM and QSR techniques is also proposed to further reduce the switching losses. At the last section, some simulations are performed to evaluate performance of the proposed converter.

The prototype system and a testing facility are constructed and illustrated in chapter 5. All the control algorithms are implemented with a digital signal processor, TMS320 F2812. Some experimental results are given to evaluate the validity and performance of the proposed WPGS.

Finally, some conclusions and future works are offered in the last chapter.

CHAPTER 2

CONVENTIONAL SMALL WPGS WITH STEADY STATE OPTIMAL TORQUE MPPT CONTROL

2.1 Introduction

In this chapter, a conventional small wind power generation system with steady state optimal torque MPPT control is introduced as a basis. A conventional small wind power generation system basically consists of a small scale wind turbine, a permanent magnet generator, a two-stage ac to dc converter composed of a diode bridge rectifier, a dc converter, a battery module and a dc load or an inverter.

First, the characteristics of the small wind turbine are described. For realizing the power conversion between mechanical power and electrical power, the model of the permanent magnet generator is then introduced in section 2.3. Configuration and operational principles of the conventional small WPGS are illustrated in section 2.4 in detail as well as the steady state optimal torque MPPT control. Finally, some simulation results are given to evaluate the performance of the conventional system.

2.2 Characteristics of the Small Wind Turbine

The kinetic energy of the wind with a velocity v_w can be determined as [9]

$$E = \frac{1}{2} m v_w^2 \tag{2.1}$$

where m is the mass of the moving air which can be expressed as following equation.

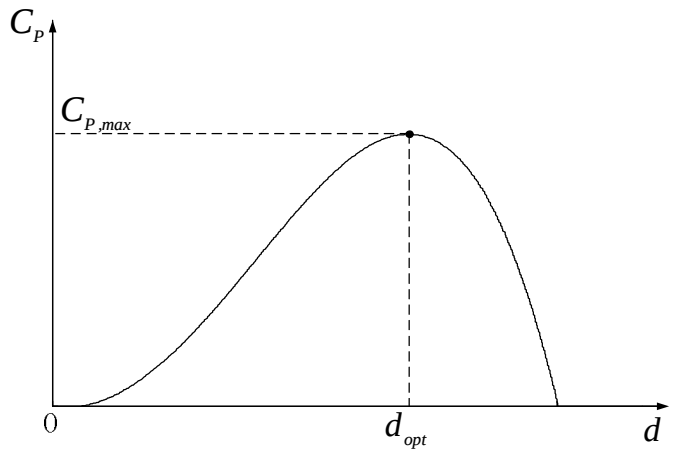

Fig. 2.1 A typical curve of the power coefficient of a small wind turbine.

$$m = r A v_w t \tag{2.2}$$

where r is the air density, A is the effective area swept by the wind turbine and t denotes the time. Then, the power of the moving air with constant velocity is expressed as

$$P_{air} = \frac{dE_{air}}{dt} = \frac{d}{dt}(\frac{1}{2} m v_w^2) = \frac{1}{2} r A v_w^3 \tag{2.3}$$

By utilizing the wind turbine, part of the aerodynamic power expressed in (2.3) can be converted into mechanical power. The conversion efficiency between the aerodynamic power and mechanical power is depended on the geometric structure of wind turbine. The mechanical power output from the wind turbine, i.e., the extracted wind power, can be defined as

$$P_w = \frac{1}{2} r A C_p v_w^3 \tag{2.4}$$

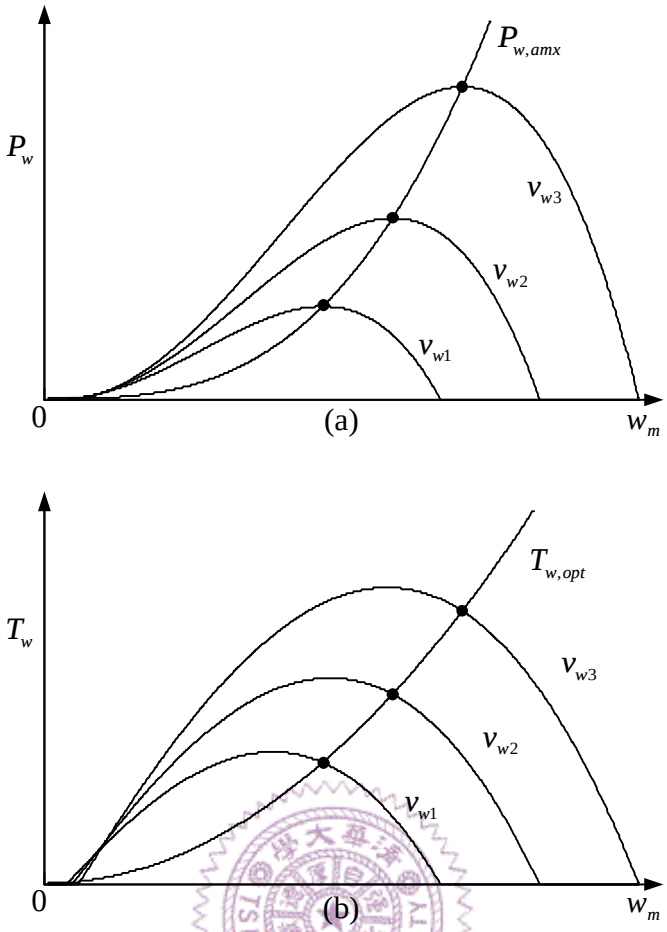

Fig. 2.2 Characteristic curves of wind turbine. (a) Output power, (b)output torque.

where $C_p < 1$ is the power coefficient which is defined as the ratio of the extracted wind power to the aerodynamic power. Normally, the power coefficient is a function of tip speed ratio (TSR) and pitch angle of the wind turbine. However, the pitch angle of a small wind turbine is usually fixed. Therefore, the power coefficient of a small wind turbine can be expressed as a function only of the TSR which is defined as follows.

$$d = \frac{r \cdot w_m}{v_w} \tag{2.5}$$

where r is the radius of the wind turbine and w_m is the rotating angular speed of the wind turbine. A typical power coefficient curve is shown in Fig. 2.1. It is obvious that the power coefficient will reach the maximum value, $C_{p,\max}$, while the TSR of the wind turbine is controlled to the optimal value, d_{opt}. Hence, we can obtain the maximum captured wind power as follows.

$$P_{w,\max} = k \cdot w_m^3 \tag{2.6}$$

$$k = \frac{r A r^3 C_{p,\max}}{2 d_{opt}^3} \tag{2.7}$$

The optimal output torque of the wind turbine at the maximum power point can also be obtained as follows.

$$T_{w,opt} = \frac{P_{w,\max}}{w_m} = k \cdot w_m^2 \tag{2.8}$$

The power and torque curves of the wind turbine with respect to the rotating angular speed under different wind velocities are shown in Fig. 2.2. For the power mapping MPPT control strategy, the maximum power curve in (2.6) is used as the reference signal for controlling the generator output power. Similarly, in the optimal torque MPPT control strategy, the controller reference signal is obtained from the optimal torque curve as shown in Fig. 2.2(b). To converting the mechanical power from the wind turbine into electrical power, a permanent magnet generator is widely adopted in small systems and usually directly driven by the wind turbine. Typically, a two-stage ac to dc converter is usually connected to the generator for controlling the generator output power. If the generator output torque is controlled to the optimal torque

reference curve, the wind turbine will then be able to extract maximum wind power. The corresponding mechanical dynamic equation is expressed as follows,

$$T_w - T_g = J\frac{dw_m}{dt} + Bw_m \tag{2.9}$$

where J is the inertia of the mechanical shaft and T_g is the generator output torque. It can be seen that, in fact, the wind turbine rotating speed is indirectly controlled by the torque difference between the input torque from wind turbine and generator output torque. If the system is under steady state, the TSR will then be regulated to the optimal value, i.e., the wind turbine is operated at maximum power point.

2.3 Modeling of the Permanent Magnet Generator

In a small system, a permanent magnet synchronous generator is usually adopted because it has many advantages, such as high efficiency, high power density and requiring no additional exciting circuit. Recently, axial flux permanent magnet (AFPM) generators are widely integrated into small vertical axial wind turbines due to the high efficiency and compactness. The typical structure of an axial flux permanent magnet generator is shown in Fig. 2.3. It can be seen from Fig. 2.3 that the permanent magnets are mounted onto the rotor disks to produce an axial magnetic field. The stator is placed between the two rotor disks. For distributed power generation systems, a coreless stator is usually adopted because of the absence of core losses. The dynamic model of the coreless axial flux permanent magnet generator in the stationary reference frame with the space vector notation [10]-[12] is given as follows.

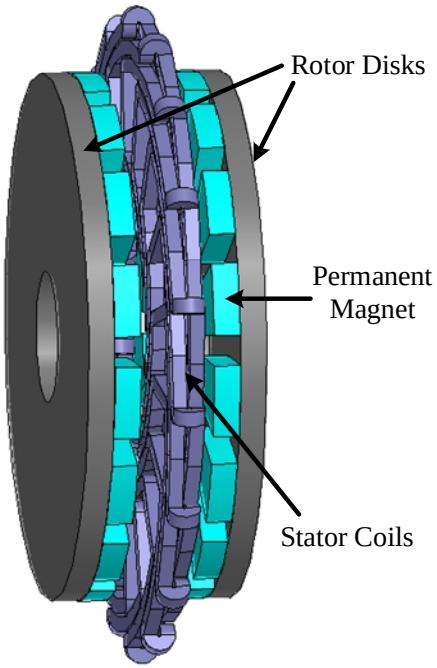

Fig 2.3 Basic structure of a axial flux permanent magnet machine.

$$\mathbf{v}_s^s = -R_s \mathbf{i}_s^s + \frac{d\,\mathbf{l}_s^s}{dt} \tag{2.10}$$

$$\mathbf{l}_s^s = -L_s \mathbf{i}_s^s + \mathbf{l}_r^s \tag{2.11}$$

$$\mathbf{l}_r^s = l_f e^{jq} \tag{2.12}$$

where l_f is the magnitude of the flux linkage due to the permanent magnet, q is the angle between the a-phase magnetic axis of the rotor and the direct axis of the stator, R_s and L_s are the equivalent winding resistance and inductance, respectively. By aligning the direct axis of the synchronous reference frame with the rotor a-phase magnetic axis, one can obtain the transformation between the stationary and the synchronous rotating reference frame as follows.

$$\vec{x}^{s} \cdot e^{-jq} = \vec{x}^{e} \qquad x \in \{v_s, i_s, l_f, l_r\} \tag{2.13}$$

Hence, from (2.10) to (2.13), the dynamic model of the generator in the synchronous reference frame with space vector notation will become

$$\vec{v}_s^{e} = -R_s \vec{i}_s^{e} - L_s \frac{d\vec{i}_s^{e}}{dt} - jL_s \vec{i}_s^{e} \frac{dq}{dt} + j l_f \frac{dq}{dt} \tag{2.14}$$

Then, the corresponding d-axis and q-axis can be obtained as well.

$$v_d = -R_s i_d - L_s \frac{di_d}{dt} + L_s i_q \frac{dq}{dt} \tag{2.15}$$

$$v_q = -R_s i_q - L_s \frac{di_q}{dt} - L_s i_d \frac{dq}{dt} + l_f \frac{dq}{dt} \tag{2.16}$$

For a coreless AFPM generator, there are no core losses due to the absence of the iron cores in the stator windings. However, the eddy-current losses in the stator windings may be remarkable because the wind turbine will be operated at high rotating speed sometimes. To evaluate the performance of the generator more accurately, the eddy-current losses may be taken into account by shunting a equivalent eddy-current loss resistance, R_e, with the EMF of the generator [11]. Then, according to (2.15) and (2.16), one can obtain the corresponding d-axis and q-axis equivalent circuits of the generator in the synchronous reference frame as shown in Fig. 2.4. The relative equivalent circuit of each phase in the stationary reference frame can also be obtained as shown in Fig. 2.5. The EMF is defined as

$$e_a = E_m \cos q \tag{2.17}$$

where $E_m = l_f \frac{dq}{dt}$ is the amplitude of the phase EMF. The electromagnetic torque

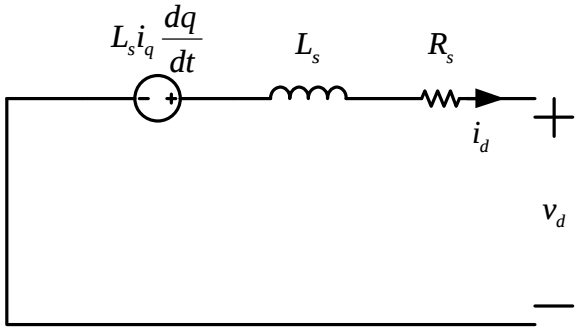

(a)

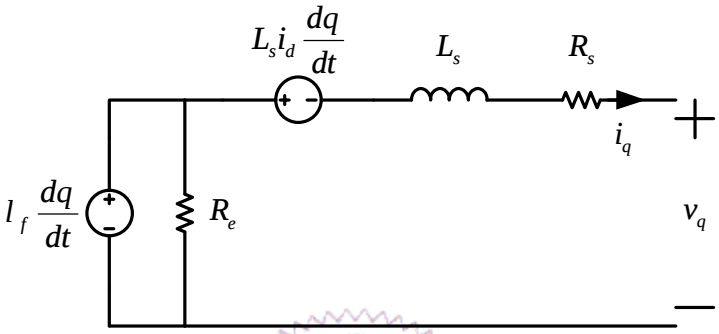

(b)

Fig. 2.4 Equivalent circuits of the generator in the synchronous reference frame. (a) d-axis equivalent circuit, (b) q-axis equivalent circuit.

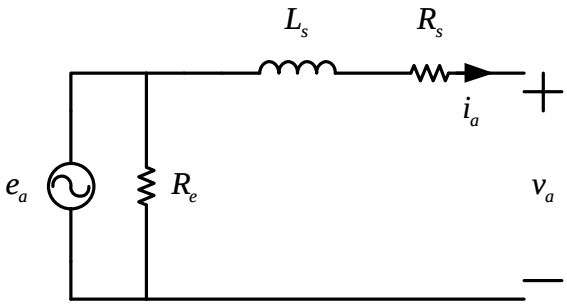

Fig. 2.5 Single phase equivalent circuit of the generator in the stationary reference frame.

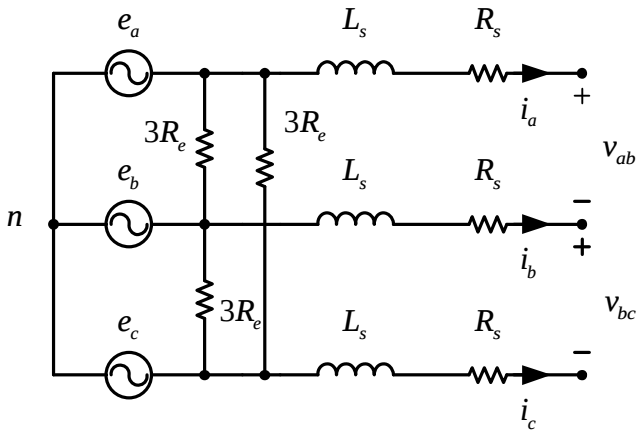

Fig. 2.6 The three phase equivalent circuit of the generator in the stationary reference frame.

induced by the PM generator can be obtained as follows.

$$T_g = \frac{3}{2}\frac{P}{2} l_f I_m \tag{2.18}$$

where P is the number of poles and I_m is the amplitude of the generator output current. If the stator windings are three-phase three-wire star type connected, the corresponding three phase equivalent circuit could be illustrated as Fig. 2.6. The eddy-current loss resistance my be calculated by the following equation,

$$R_e = \frac{3E_m^2}{2P_e} \tag{2.19}$$

where P_e denotes the eddy-current loss. The eddy-current loss may be accurately determined by the methodology proposed in [13]. However, an approximated solution of the eddy-current losses [14] is given as

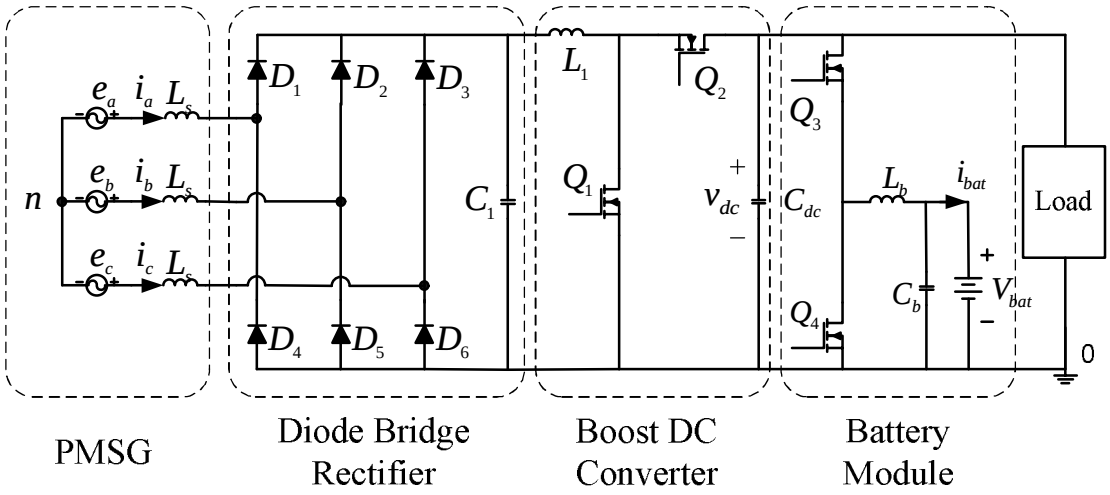

Fig. 2.7 A micro-scale WPGS with a conventional two-stage ac to dc converter.

$$P_e = \frac{p\,\mathbf{l}d^4 w_e^2}{32\,r}(B_x^2 + B_y^2)N_c \tag{2.20}$$

where $\mathbf{l}$ is the conductor length, w_e is the electrical angular frequency, d is the conductor diameter, N_c is the number of the conductors in the generator, B_x and B_y are the peripheral and axial components of the flux density, respectively. Consequently, it is much more convenient to analyze the generator performance with the three-phase equivalent circuit model shown in Fig. 2.6.

2.4 Operation Principles of a Conventional Small WPGS

For a system with some kW rating, a conventional two-stage ac to dc converter composed a diode bridge rectifier and a dc converter as shown in Fig. 2.7 is usually adopted because of cost consideration and easy implementation. A boost dc converter

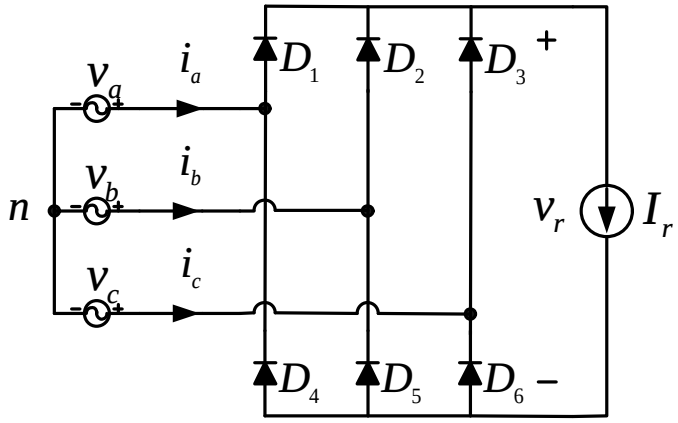

Fig. 2.8 Approximately equivalent circuit of a diode bridge rectifier

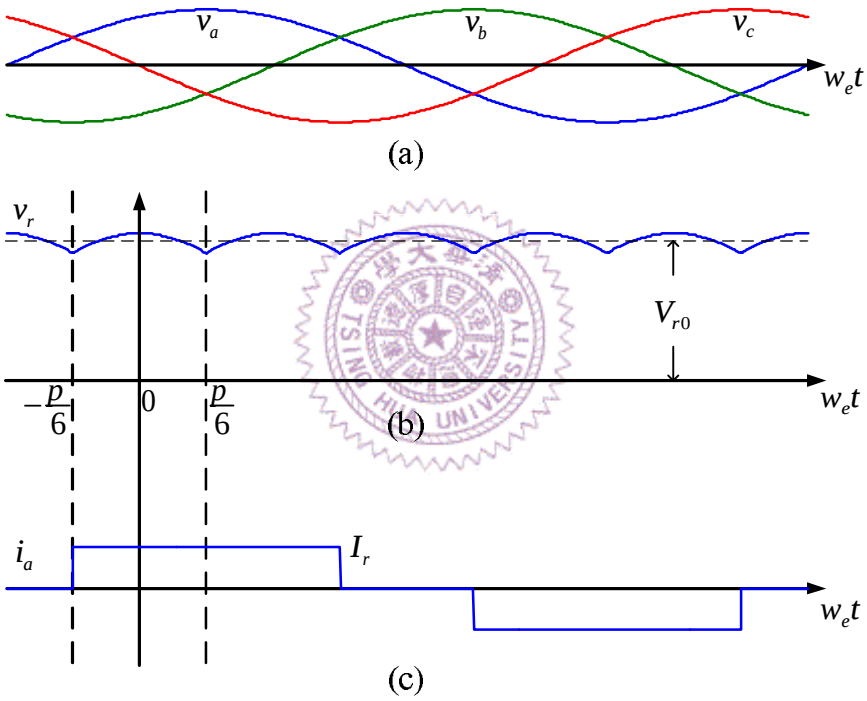

Fig. 2.9 Waveforms of a diode bridge rectifier. (a) Three phase voltages, (b) rectifier output voltage, (c) a-phase current.

is connected to the output side of the front-end diode bridge rectifier. The output voltage of the diode bridge rectifier is then controlled by the second-stage dc converter for achieving MPPT. The dc output voltage v_{dc} of the dc converter is

usually regulated as a constant voltage by a battery module in a stand-alone system or an inverter in a grid-tided system. To reduce the system cost and simplify the controller, the well-known steady state optimal torque MPPT control strategy [2][3] is usually used in small-scale systems without using mechanical sensors such as anemometers and encoders.

2.4.1 The Conventional Two-Stage AC to DC Converter

Because of no external exciting circuit is needed for a PM generator, a diode bridge rectifier is widely be used as the front-end ac to dc converter. Moreover, to achieve MPPT control of wind turbine, a second-stage dc converter is usually adopted. The wind turbine rotating speed can be indirectly controlled by managing the output power of the rectifier. To achieve rotating speed sensorless MPPT control, the information of rotating speed can be obtained by an approximate expression of the relationship between the rotating speed and the diode bridge rectifier output dc voltage.

First, for convenience to analyze the relationship between the rotating speed and rectifier output voltage, the stator inductances are assumed to be zero and a constant load current I_r is used to represent the output load as shown in Fig. 2.8. The waveforms of the output dc voltage v_r and input phase current i_a are shown in Fig. 2.9. From Fig. 2.9(b), the averaged output dc voltage V_{r0} can be obtained from the line to line voltage and expressed as follows [15].

$$V_{r0} = \frac{3}{p}\int_{-\frac{p}{6}}^{\frac{p}{6}} \sqrt{3}V_m \cos w_e t d(w_e t) = \frac{3\sqrt{3}}{p}V_m \tag{2.21}$$

where V_m is the amplitude of the fundamental terminal phase voltage of the generator and w_e is the fundamental electrical angular frequency of the stator. Then, the fundamental phase current can be obtained from Fourier analysis of the phase current as shown in Fig. 2.9(c). The amplitude of the fundamental phase current can then be expressed as follows.

$$I_m = \frac{\sqrt{6}}{p} I_d \tag{2.22}$$

According to [3], the approximated output dc voltage with consideration about the stator inductance effect can be obtained as follows.

$$V_{r0} = \frac{3\sqrt{3}}{p} V_m - \frac{3}{\sqrt{6}} w_e L_s I_m \tag{2.23}$$

The second term in the right side of eq. (2.23) is used to represent the voltage loss due to the current commutation resulting from the stator inductances. The amplitude of the fundamental terminal phase voltage can then be obtained as follows.

$$V_m = E_m - I_m \sqrt{R_s^2 + w_e^2 L_s^2} \tag{2.24}$$

where E_m is the amplitude of the fundamental phase back EMF and R_s is the equivalent stator resistance of the stator windings. It can be seen that, from (2.23) and (2.24), one can calculate the rotating speed of the wind turbine from the output dc voltage of the diode bridge rectifier. Once the rotating speed is calculated, the generator torque command and the dc converter current command can both be derived as well. However, it is well known that there will be significant THD in the generator currents because of the nonlinearity of diode bridge rectifier. The current harmonics are usually neglected for simplifying the system analysis and controller design.

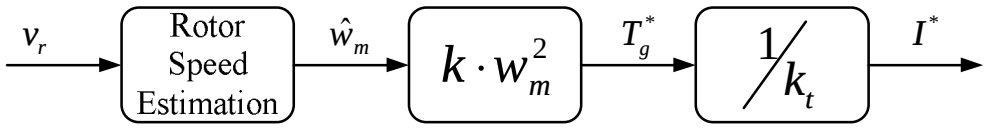

Fig. 2.10 The control block diagram of the optimal torque MPPT control.

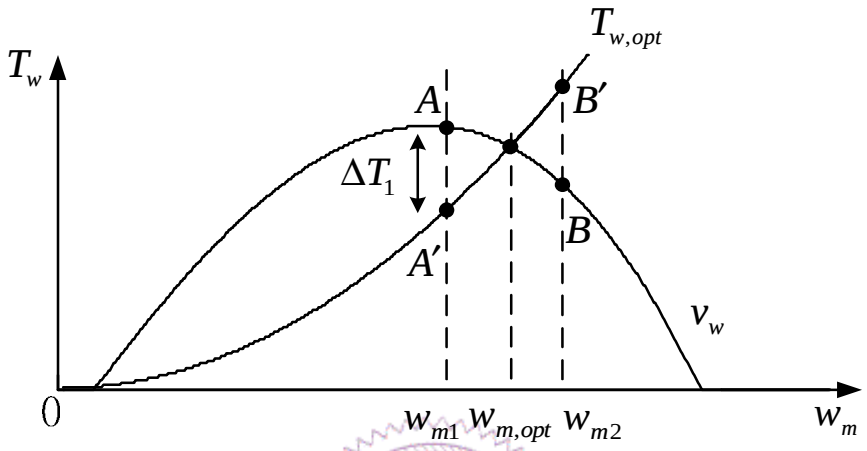

Fig. 2.11 The diagram of the principle of the OT MPPT control.

In fact, it will cause additional power losses, mechanical stress and undesired acoustic noise.

2.4.2 The Steady State Optimal Torque MPPT Control

The well-known steady state optimal torque MPPT control strategy is widely used in wind power generation systems for reducing the system cost and controller complexness because the information of the wind velocity is not required. The control block diagram of the steady state optimal torque MPPT control strategy is shown in Fig. 2.10. First, according to (2.23) and (2.24) the rotating speed can be directly determined from the rectifier output voltage without using any mechanical sensor.

Then, the command signal of the generator output torque is obtained according to (2.8). Also, based on (2.18) and (2.22), the current command of the dc converter can be determined from the torque command of the generator. At the end, while the inductor current of the dc converter is controlled to the reference signal, the wind turbine will finally be operated at maximum power point. Fig. 2.11 shows the curves of the input torque induced by the captured wind power at a constant wind velocity and the optimal torque with respect to the rotating speed. When the wind turbine rotating with angular speed, w_{m1}, then the generator output torque will be controlled to point A', namely $T_{gA'} = k \cdot w_{m1}^2$, and the input torque from the captured wind power will then be at point A, namely $T_{wA} = \frac{r A v_w^3}{2 w_{m1}} C_p(d_1)$. Therefore, the torque difference between the input torque from wind turbine and the generator output torque can then be obtained.

$$\Delta T_1 = T_{w1} - T_{g1} = J \frac{dw_{m1}}{dt} + B w_{m1} > 0 \tag{2.25}$$

It is obviously that the wind turbine will be accelerated by the positive torque difference at rotating speed, w_{m1}. On the contrary, if the wind turbine rotating with angular speed, w_{m2}, faster than the optimal rotating speed at maximum power point. Based on the optimal torque MPPT control algorithm, the generator output torque will be controlled to point B', namely $T_{g2} = k \cdot w_{m2}^2$, which is larger than the input wind power torque, $T_{w2} = \frac{r A v_w^3}{2 w_{m2}} C_p(d_2)$. Hence, the wind turbine will then be decelerated by the negative torque difference. It can be seen that with the above mentioned operation principles, the rotating speed of wind turbine will be converged toward the optimal speed at the maximum power point.

2.5 Simulation Results

A small WPGS with steady state optimal torque MPPT control and a two-stage ac to dc converter is simulated by means of simulation software PSIM. Some simulation results are given to realize the performance of the conventional small WPGS. The model of wind turbine is used to represent a small vertical wind turbine DS-200 which is manufactured by Hi-VAWT Technology Corportion. Fig. 2.12 and Fig. 2.13 show the simulation waveforms of the WPGS operated at 8 m/s wind speed. Fig. 2.14 and Fig. 2.15 show the simulation waveforms of the WPGS while wind speed is changing between 6 m/s and 8 m/s. The generator current contains a lot of harmonic components as shown in Fig. 2.12(b) and (c) which is caused by the nonlinearity of diode bridge rectifier. Moreover, due to the significant current harmonic distortion, the generator output power and torque are influenced. The pulsating torque will cause additional mechanical stress on shaft and serious acoustic noise which is with sixth order frequency of generator fundamental electrical frequency. From Fig. 2.14, one can see that it is impossible to well track the maximum power point because of the mechanical inertia effect.

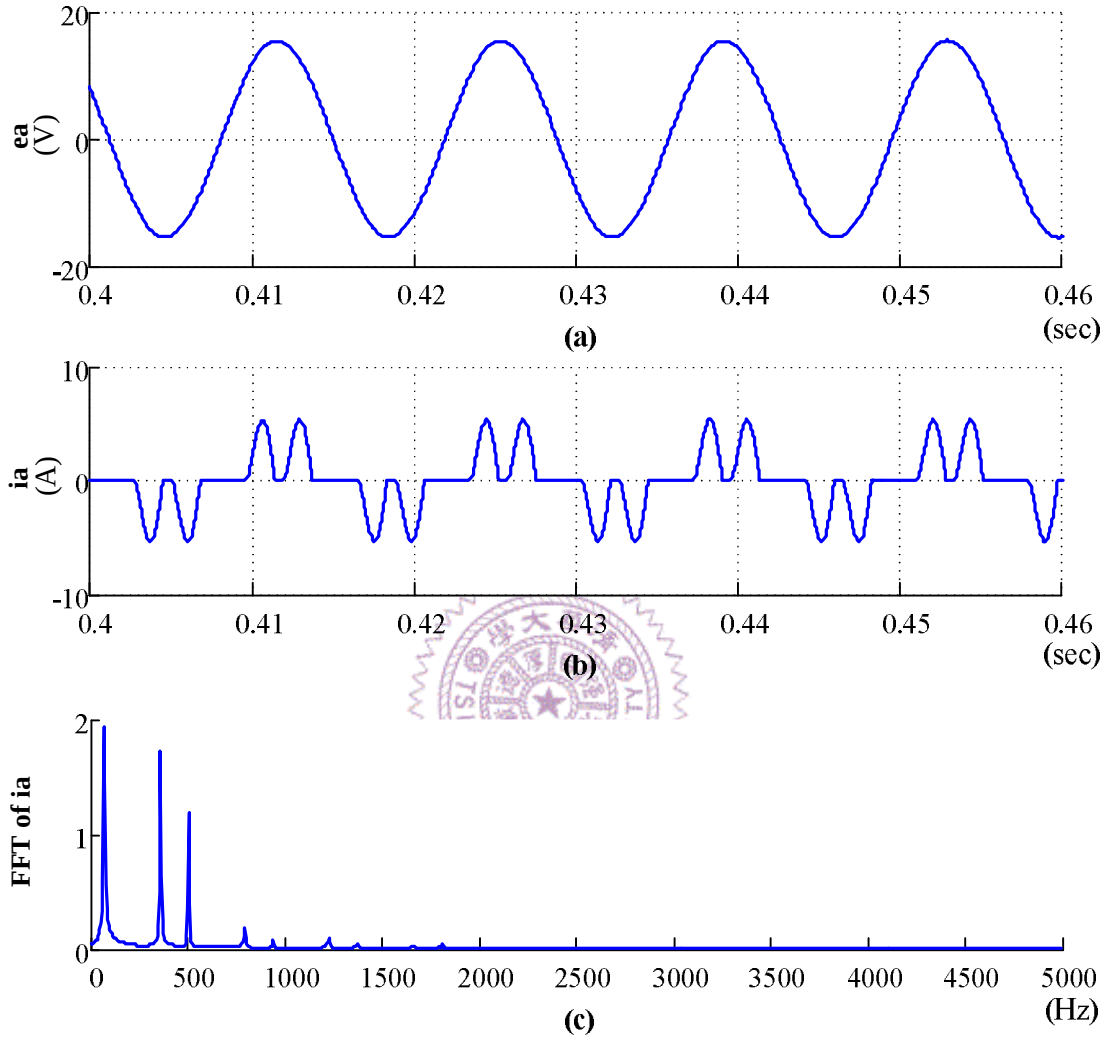

Fig. 2.12 Simulation waveforms. (a) Phase voltage, (b) phase current, (c) FFT of phase current.

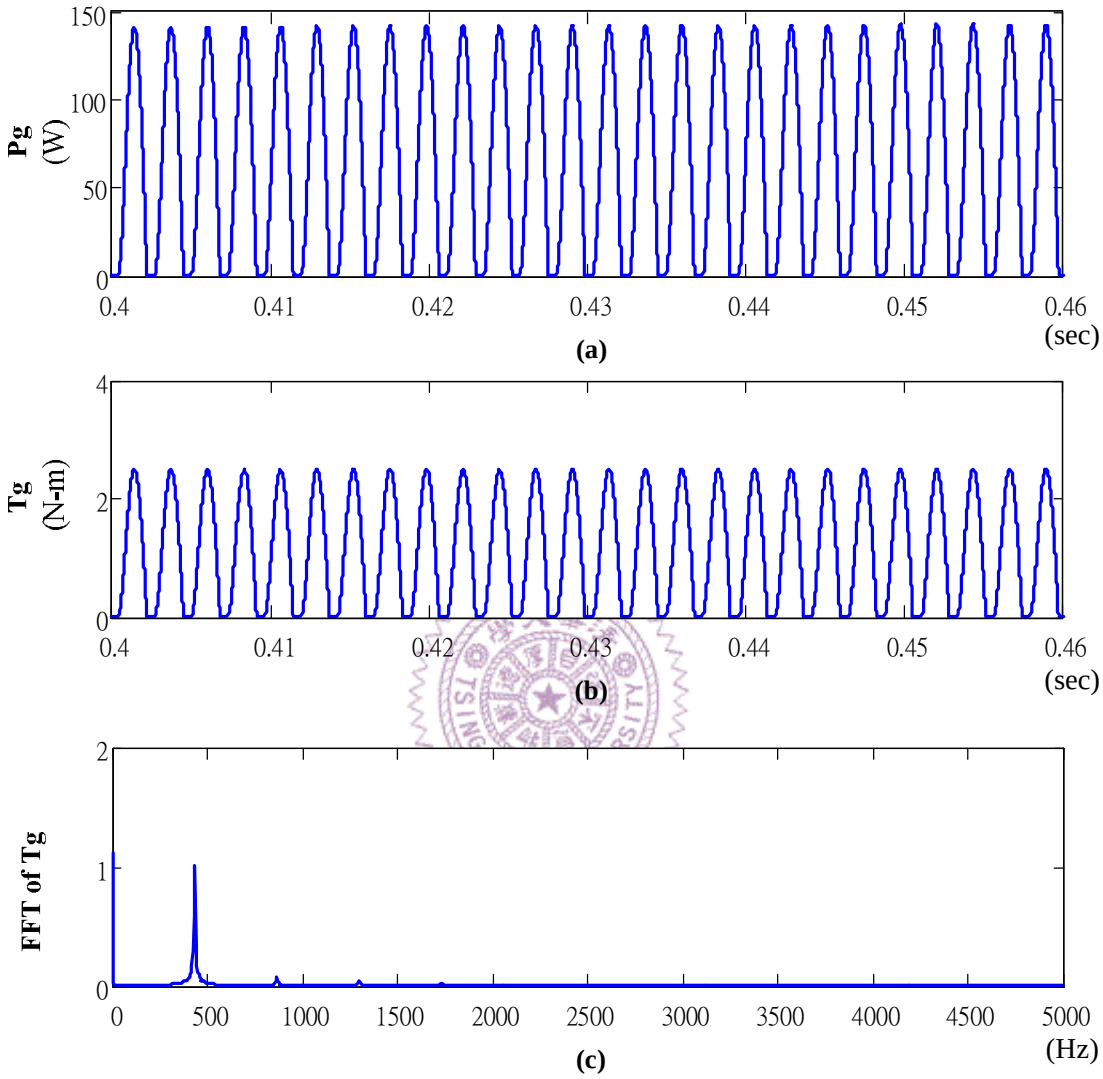

Fig. 2.13 Simulation waveforms. (a) Generator output power, (b) generator output torque, (c) FFT of generator output torque.

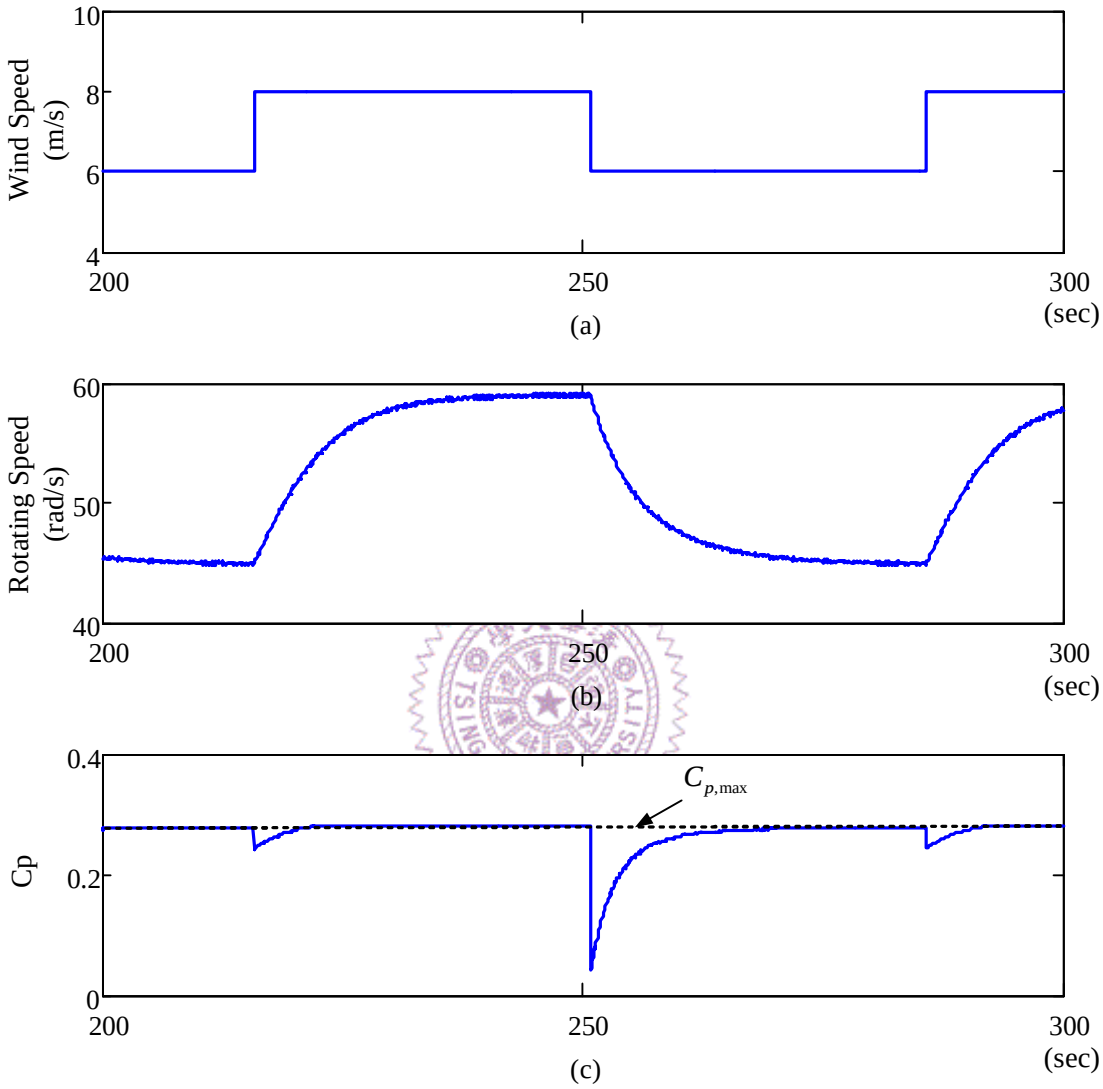

Fig. 2.14 Simulation waveforms. (a) Step changing wind speed, (b) rotating speed of wind turbine, (c) power coefficient.

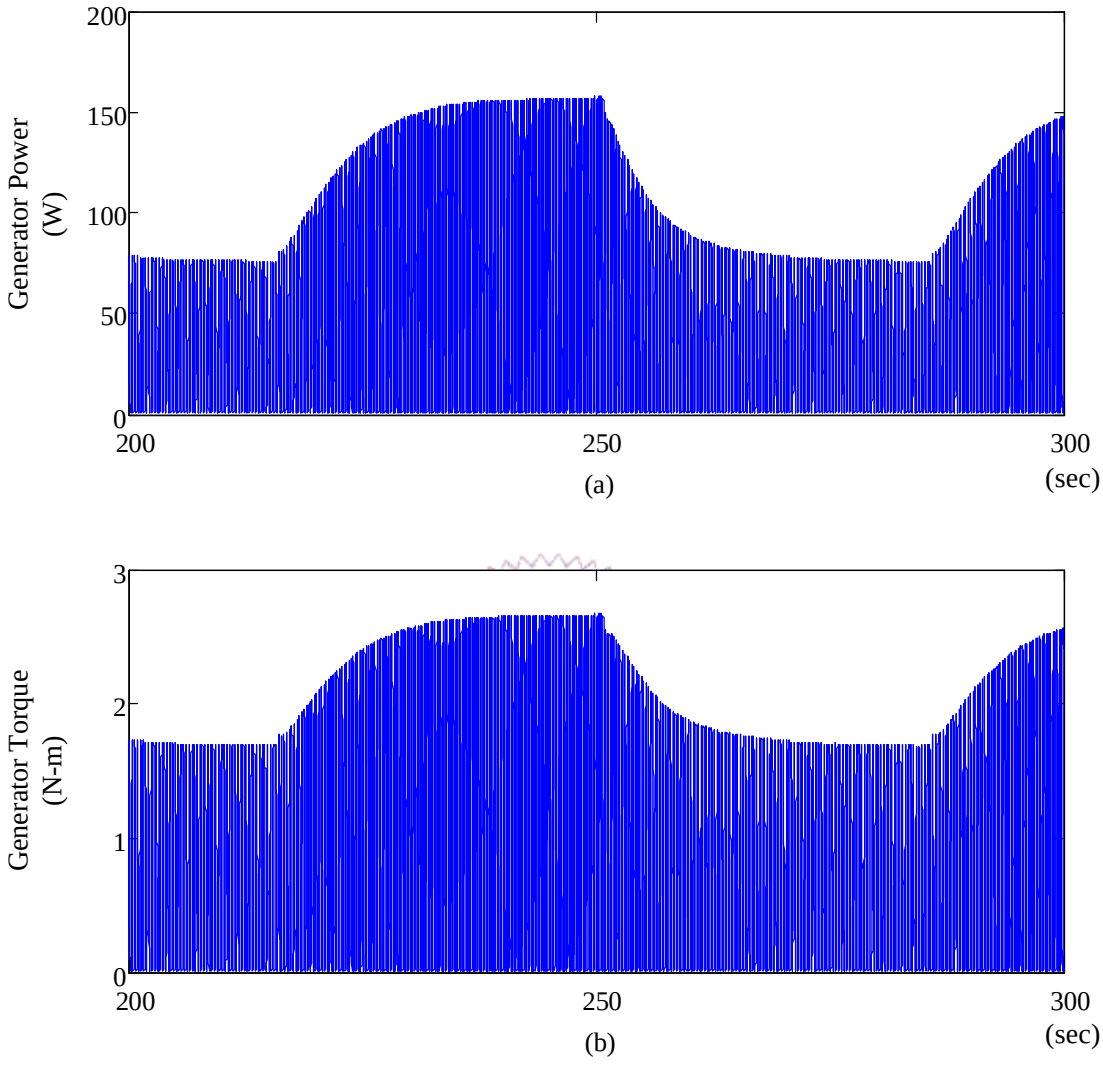

Fig. 2.15 Simulation waveforms. (a) Generator output power and (b) generator output torque.

CHAPTER 3

NOVEL SENSORLESS DYNAMIC MPPT CONTROLLER WITH ADJUSTABLE VIRTUAL INERTIA TECHNIQUE

3.1 Introduction

Due to the effect of the mechanical inertia, it is impossible to instantaneously track the maximum power point when the wind velocity is rapidly changing. This situation will become worse in the low speed region where the acceleration or deceleration torque is rather small if a conventional optimal torque or power MPPT controller is adopted. In consequence, the mechanical dynamic response will be poorer and the extracted wind energy will be less than the available maximum wind energy. To overcome this dilemma, a novel sensorless dynamic MPPT controller with adjustable virtual inertia technique is proposed in this chapter. Detailed illustration of the configuration and the principle of the proposed dynamic MPPT controller will both be described in the following sections.

In section 3.2, the operation principles of the proposed sensorless MPPT controller are first illustrated and then each element in the proposed controller is described respectively. The analysis of the proposed dynamic MPPT controller is made in section 3.3. Finally, some simulation and experimental results are given in section 3.4 to verify the validity and performance of the proposed controller.

3.2 Operation Principles of the Proposed Sensorless Dynamic MPPT Controller

The proposed sensorless dynamic MPPT controller is composed of three blocks as shown in Fig. 3.1. The first block, block A, is the phase and frequency estimator

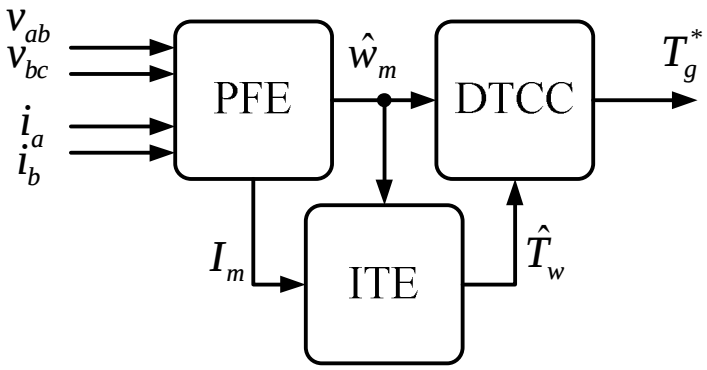

Fig. 3.1 Block diagram of the proposed dynamic MPPT controller

(PFE) that is used to estimate the phase and frequency of the generator back EMFs. Also, the wind turbine rotating speed can then be derived. Secondly, the block B is the input torque estimator (ITE) which is adopted to obtain the input torque from the wind power. The third block, block C, is the dynamic torque command calculator (DTCC) which is the core technique for determining the dynamic optimal torque command for the generator. Each of the three components will be illustrated in the following subsections in detail respectively.

3.2.1 The Phase and Frequency Estimator

Because the mechanical sensors, such as anemometers and encoders, are rather expensive, MPPT controllers without using mechanical sensors are always preferred in small scale systems. The wind speed information is inherently not necessary for the proposed MPPT controller. Furthermore, a phase and frequency estimator is adopted in the proposed controller to estimate the phase and frequency of the generator back EMFs. The rotating speed can then be derived as well. Usually, the phase and frequency can be obtained by using a phase locked loop (PLL) technique. PLL technique has been developed for many years and widely used in servo motor

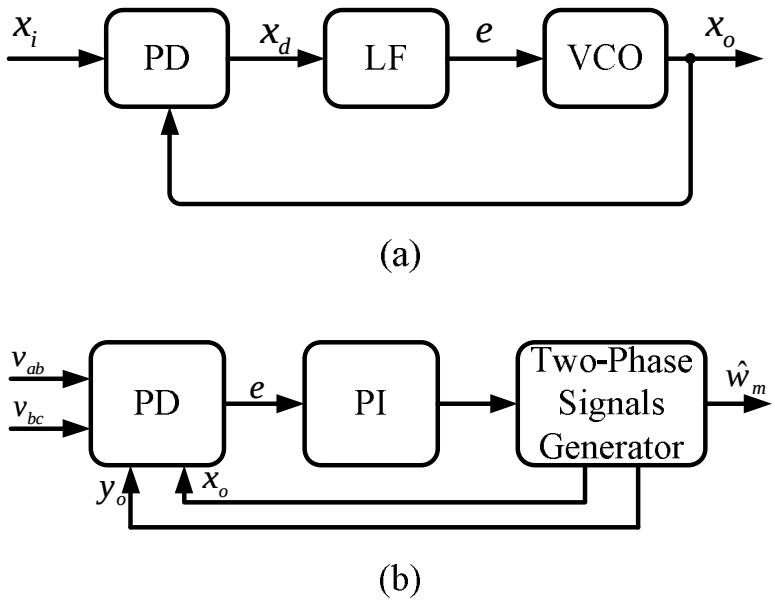

Fig. 3.2 Block diagrams of (a) basic phase lock loop and (b) the phase and frequency estimator of the proposed controller.

controllers. Fig. 3.2(a) shows the block diagram of a basic PLL. A conventional PLL is basically composed of three elements that are a phase detector (PD), a loop filter (LF) and a voltage-controlled oscillator (VCO). For sinusoidal applications, the input signal x_i and the VCO output signal x_o are considered as

$$\begin{aligned} x_i &= a_i \sin q_i \\ x_o &= a_o \cos q_o \end{aligned} \tag{3.1}$$

where a_i and q_i are the amplitude and phase of the input signal, a_o and q_o are the amplitude and phase of the VCO output signal. A multiplier is usually used as the PD and the output signal x_d can be expressed as

$$\begin{aligned} x_d = x_i x_o &= a_i a_o \sin q_i \cos q_o \\ &= \frac{1}{2} a_i a_o [\sin(q_i - q_o) + \sin(q_i + q_o)] \end{aligned} \tag{3.2}$$

Once the PLL is locked, the output signal frequency will then be equal to the input signal frequency. It can be seen from (3.2) that there are one low frequency term, $\sin(q_i - q_o)$, and one high frequency term, $\sin(q_i + q_o)$. To filter out the high frequency term, a low pass filter is usually used as the loop filter. The output signal of the LF is given as

$$e = \frac{1}{2} a_i a_o \sin(q_i - q_o) \tag{3.3}$$

Furthermore, if the phase difference $q_i - q_o$ is small enough, then (3.3) can be approximated as

$$e = \frac{1}{2} a_i a_o (q_i - q_o) \tag{3.4}$$

Then, the output signal of LF is fed into the VCO. The frequency of the VCO output signal will then be proportional to the phase error in (3.3). In other words, if the phase error is increasing, the frequency of the VCO output signal will be increased as well to keep the output signal closer to the input signal, vice versa. Consequently, under such a closed loop mechanism, the output signal will finally be kept to synchronous with the input signal. However, the major disadvantage of the conventional PLL is the limited bandwidth because of the low pass filter whose cut off frequency is only double of the input signal frequency. It turns out that the design of the low filter is rather difficult. Moreover, due to the variations of the frequency and amplitude of the generator back EMFs, the cut off frequency will not be constant so that the conventional PLL would not be suitable for WPGS.

Instead of using a conventional PLL technique, a two-phase type PLL [16][17] that is independent of frequency is adopted in the proposed controller. The block

diagram of the PFE is shown in Fig. 3.2(b). The terminal voltages, v_{ab} and v_{bc}, are sensed and transformed to the stationary reference frame as the two-phase input signals for the PFE. In a small-scale system, the phase and amplitude differences between the terminal phase voltage and the phase back EMF are small enough to be neglected. As a result, the terminal line voltages can be approximately expressed as

$$\begin{aligned} v_{ab} &\cong e_a - e_b = \sqrt{3}E\cos(q_e + \frac{p}{6}) \\ v_{bc} &\cong e_b - e_c = \sqrt{3}E\cos(q_e - \frac{p}{2}) \\ v_{ca} &= -(v_{ab} - v_{bc}) \end{aligned} \tag{3.5}$$

where e_a, e_b, e_c are the phase back EMFs of the generator and E is the amplitude of the phase back EMFs. Then, the voltages in the stationary reference frame can be derived as

$$\begin{bmatrix} v_a \\ v_b \end{bmatrix} = \begin{bmatrix} 1 & 0 \\ \frac{1}{\sqrt{3}} & \frac{2}{\sqrt{3}} \end{bmatrix} \begin{bmatrix} v_{ab} \\ v_{bc} \end{bmatrix} \cong \begin{bmatrix} \sqrt{3}E\cos(q_e + \frac{p}{6}) \\ \sqrt{3}E\sin(q_e + \frac{p}{6}) \end{bmatrix} \tag{3.6}$$

A two-phase type phase detector is integrated to obtain the phase error e and the corresponding analytical expression is given as

$$\begin{aligned} e &= v_b\cos q_o - v_a\sin q_o \\ &= \sqrt{3}E\sin[(q_e + \frac{p}{6}) - q_o] \end{aligned} \tag{3.7}$$

where q_o denotes the phase angle of the generated signals of the quadrature signal generator (QSG). When the phase angle of the generated signals is close to that of the PD input signals, i.e. $q_o \cong q_e + p/6$, the corresponding phase error can be

approximated as follows.

$$e \cong \sqrt{3}E[(q_e + \frac{p}{6}) - q_o] \tag{3.8}$$

After the refinement through a PI controller, the refined phase difference, namely Δq_o , is obtained from the PI controller as shown in block A. In this paper, the proposed controller is implemented by using a digital signal processor (TMS320 F2812) and the phase angle of the generated signals is based on the following difference equation.

$$q_o(k) = q_o(k-1) + \Delta q_o(k) \tag{3.9}$$

If the input signals are not in phase with the generated signals of QSG, i.e. $e \neq 0$, then the output signal of the PI controller will be varied for adjusting the phase angle and the frequency of the generated signals from the QSG. Hence, as the PLL is locked, Δq_o will remain constant and the corresponding electrical angular frequency and the rotor speed can be obtained as follows.

$$\hat{w}_e = \frac{P}{2}\hat{w}_m = \frac{\Delta q_o}{T_s} \tag{3.10}$$

where T_s is the sampling time. As a byproduct, the amplitude of the generator current can also be obtained according to the following equation.

$$I_m = \mathbf{i}_s^s \cdot e^{-jq_e} = (i_a + ji_b) \cdot e^{-j(q_o - \frac{p}{6})} \tag{3.11}$$

where $i_a = i_a$ and $i_b = (i_a + 2i_b)/\sqrt{3}$.

3.2.2 The Input Torque Estimator

In the proposed MPPT control algorithm, the information of the input torque from the wind turbine is required for determining the dynamic optimal torque command. For cost consideration, a well-known reduced order estimator [18][19] instead of a mechanical torque transducer is adopted to obtain the information of the input torque.

A basic system dynamic equation can be expressed as

$$\begin{bmatrix} \dot{x}_1 \\ \dot{x}_2 \end{bmatrix} = \begin{bmatrix} k_{11} & k_{12} \\ k_{21} & k_{22} \end{bmatrix} \cdot \begin{bmatrix} x_1 \\ x_2 \end{bmatrix} + \begin{bmatrix} h_1 \\ h_2 \end{bmatrix} \cdot u \tag{3.12}$$

$$y = \begin{bmatrix} 1 & 0 \end{bmatrix} \cdot \begin{bmatrix} x_1 \\ x_2 \end{bmatrix} \tag{3.13}$$

where x_1 is the known variable and x_2 denotes the unknown variable needed to be estimated. According to [18], the dynamic equation of the estimation of the unknown variable in reduced order estimator is given as

$$\dot{\hat{x}}_2 = k_{22}\hat{x}_2 + k_{21}y + h_2u + m(\dot{y} - k_{11}y - h_1u - k_{12}\hat{x}_2) \tag{3.14}$$

where $\hat{x}_2$ denotes the estimated value of x_2. Then, the estimation error can be defined as

$$\dot{x}_2 \equiv x_2 - \hat{x}_2 \tag{3.15}$$

From (3.12) to (3.15), the dynamic equation of the estimation error can be expressed as follows

$$\dot{x}_2 = (k_{22} - mk_{12})\dot{x}_2 \tag{3.16}$$

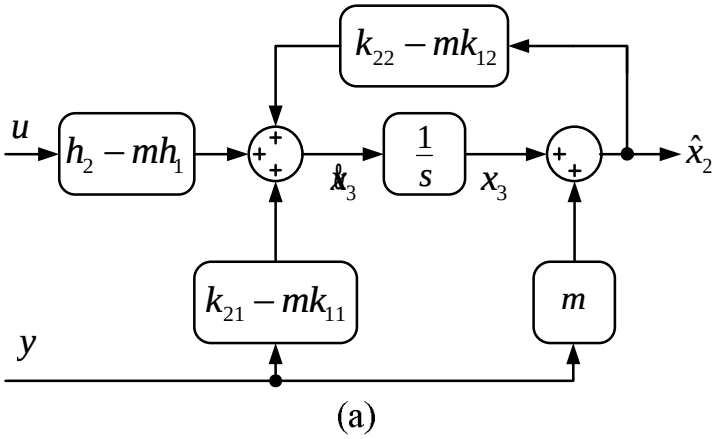

(a)

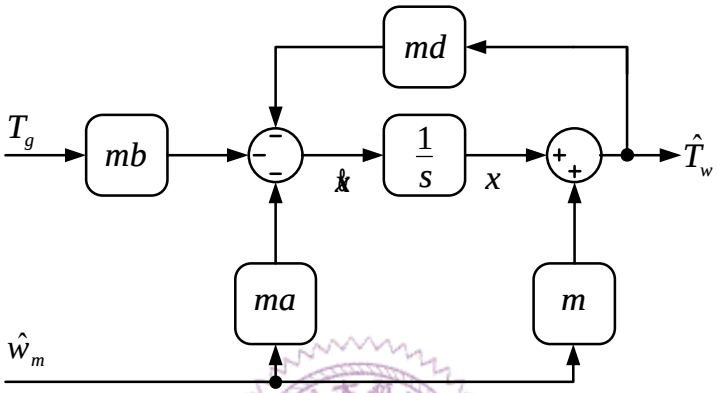

(b)

Fig. 3.3 Block diagrams of (a) reduced order estimator and (b) input torque estimator.

It is seen that the term $(k_{22} - mk_{12})$ is the eigenvalue of the estimation dynamic equation. Therefore, one can easily design the dynamics of the estimator by selecting coefficient m. After rearrangement of (3.14), one can then obtain

$$\dot{\hat{x}}_2 = (k_{22} - mk_{12})\hat{x}_2 + (k_{21} - mk_{11})y + (h_2 - mh_1)u + m\dot{y} \tag{3.17}$$

However, the derivate term in (3.17) is hardly implemented. It is well known that differentiation always amplifies undesired noise. Hence, to avoid this situation, a new controller variable is defined as follows to prevent using $\dot{y}$.

$$x_3 \equiv \hat{x}_2 - my \tag{3.18}$$

In terms of the new variable, the reduce order estimator can then be implemented with the following expression.

$$\dot{x}_3 = (k_{22} - mk_{12})\hat{x}_2 + (k_{21} - mk_{11})y + (h_2 - mh_1)u \tag{3.19}$$

The block diagram of the reduced order estimator is illustrated in Fig. 3.3(a). As a result, the derivation is no longer required in the estimator.

To apply the above mentioned reduced order estimator to obtain the input torque information, the relationship between the system dynamic equations should be realized. The mechanical dynamic equation of the wind turbine is given as

$$\begin{bmatrix} \dot{w}_m \\ \dot{T}_w \end{bmatrix} = \begin{bmatrix} a & d \\ 0 & 0 \end{bmatrix} \cdot \begin{bmatrix} w_m \\ T_w \end{bmatrix} + \begin{bmatrix} b \\ 0 \end{bmatrix} \cdot T_g \tag{3.20}$$

$$y = \begin{bmatrix} 1 & 0 \end{bmatrix} \cdot \begin{bmatrix} w_m \\ T_w \end{bmatrix} \tag{3.21}$$

where $a = -\frac{B}{J}$, $d = -b = \frac{1}{J}$. From (3.12), (3.13) and (3.17)-(3.21), one can directly obtain the estimator of the input torque expressed as follows.

$$\dot{x} = -md\hat{T}_w - maw_m - mbT_g \tag{3.22}$$

$$x = \hat{T}_w - mw_m \tag{3.23}$$

The block diagram of the input torque estimator is shown in Fig. 3.3(b).

3.2.3 The Dynamic Optimal Torque Command Calculator

In conventional optimal torque MPPT control, the generator torque command is

determined by the steady state optimal torque curve. Usually, the electrical dynamic response is much faster than the mechanical dynamic response. Hence, the generator output torque with a conventional MPPT controller can be expressed as

$$T_g \cong T_{gs}^* = k \cdot w_m^2 \tag{3.24}$$

where T_{gs}^* denotes the steady state optimal torque command. Then, the mechanical dynamic equation will become

$$T_w - T_{gs}^* = T_w - k w_m^2 = J \frac{dw_m}{dt} + B w_m \tag{3.25}$$

It can be seen that the dynamic response of the wind turbine is only affected by the input torque. However, in low wind speed region, the input torque becomes rather small so that the accelerating and decelerating torque difference will also be small. It turns out that the wind turbine dynamic response to the wind speed variation will become poor especially in low speed region.

In the proposed dynamic MPPT controller, a dynamic compensation element is added to the steady state optimal torque command. The resulting dynamic optimal torque command is then given as

$$T_{gd}^* = T_{gs}^* + \Delta T \tag{3.26}$$

where ΔT is the dynamic compensation element. By replacing the conventional torque command with the new one in (3.26), the mechanical dynamic equation will be

$$T_w - T_{gd}^* = T_w - T_{gs}^* - \Delta T = J \frac{dw_m}{dt} + B w_m \tag{3.27}$$

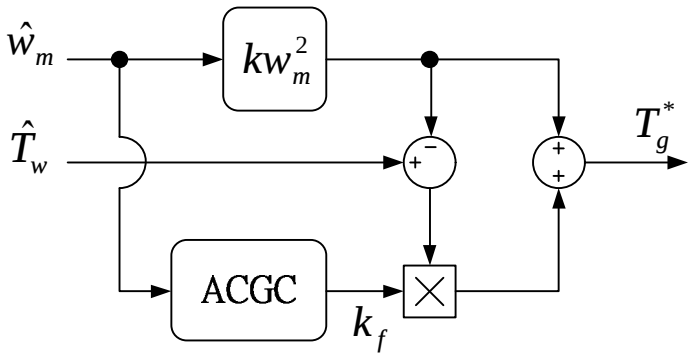

Fig. 3.4 Block diagram of the dynamic torque command calculator.

The dynamic compensation ΔT is defined as

$$\Delta T = k_f (\hat{T}_w - T_{gs}^*) \tag{3.28}$$

Then, by substituting (3.28) into (3.27), the resulting dynamic equation is

$$T_w - T_{gs}^* = J_V \frac{dw_m}{dt} + B_V w_m \tag{3.29}$$

$$J_V = \frac{J}{1-k_f} \tag{3.30}$$

$$B_V = \frac{B}{1-k_f} \tag{3.31}$$

where J_V and B_V are defined as the virtual inertia and virtual friction coefficient of the mechanical system respectively. The block diagram of the dynamic torque command calculator is shown in Fig. 3.4. Fig. 3.5 shows the loci of torque commands of conventional OT control and proposed dynamic OT control.

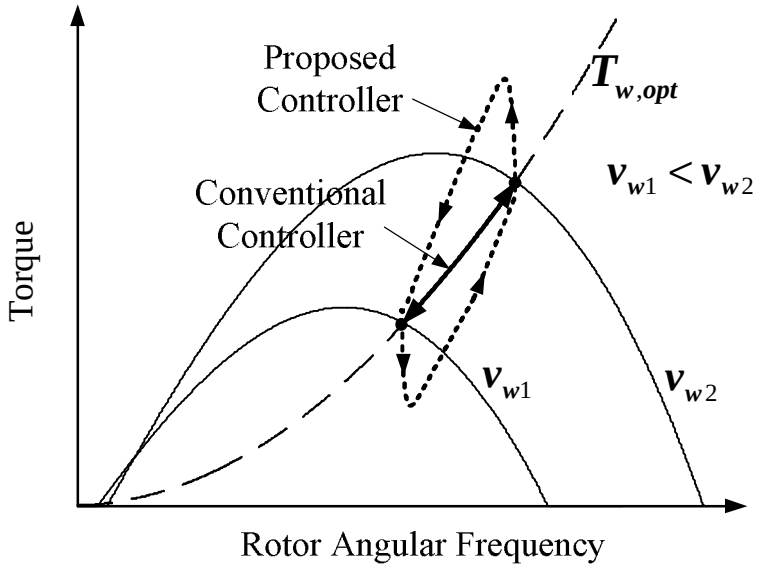

Fig. 3.5 Loci of torque commands of conventional OT control and proposed dynamic OT control.

3.3 Characteristics of the Proposed Sensorless Dynamic MPPT Controller

Because the dynamic response speeds of the two estimators and the generator current controller are much faster than that of the mechanical system, the following conditions can be assumed true after a short transient.

$$T_g \cong T_g^*, \quad \hat{T}_w \cong T_w, \quad \hat{w}_m \cong w_m \tag{3.32}$$

Hence, from (3.25), (3.29) and (3.32), one can get the resulting mechanical dynamic equation of the proposed WPGS as follows.

$$T_w - kw_m^2 = J_V \frac{dw_m}{dt} + B_V \tag{3.33}$$

To understand the merit of the proposed MPPT controller, one can consider the dynamic response of the mechanical system at different wind speed. Assume that the small signal disturbances around the operating points can be expressed as follows.

$$w_m = w_{mo} + \Delta w_m \tag{3.34}$$

$$v_w = v_{wo} + \Delta v_w \tag{3.35}$$

where w_{mo} and v_{wo} are the rotor speed and wind speed of the operating points, and Δw_m and Δv_w are considered as the small disturbance signals around the operating points, respectively. Also, the power coefficient can be approximated as a polynomial as follows.

$$C_p(d) = a_0 + a_1 d + a_2 d^2 + a_3 d^3 + a_4 d^4 \tag{3.36}$$

Then, by substituting (3.34)-(3.36) into (3.33) and taking linearization, the transfer function of Δv_w to Δw_m can be obtained as follows.

$$\frac{\Delta w_m(s)}{\Delta v_w(s)} = \frac{N}{s+M} \tag{3.37}$$

where

$$N \equiv (1-k_f)k_N w_{mo} \tag{3.38}$$

$$M \equiv (1-k_f)k_M w_{mo} + B/J \tag{3.39}$$

$$k_N \equiv \frac{r r^2 A}{2Jd_{opt}^2}(3a_0 + 2a_1 d_{opt} + a_2 d_{opt}^2 - a_4 d_{opt}^4) \tag{3.40}$$

$$k_M \equiv \frac{r r^3 A}{2Jd_{opt}^3}(a_0 - a_2 d_{opt}^2 - 2a_3 d_{opt}^3 - 3a_4 d_{opt}^4) + \frac{2k}{J} \tag{3.41}$$

One can see from (3.37) and (3.39) that the 3dB bandwidth $w_B (= M)$ is a function of k_f and w_{mo}. For a conventional OT control strategy, the bandwidth will become narrower in low wind speed range. The slow dynamic response due to the narrow bandwidth will result in reduced extracted wind energy during wind speed variation period. For the proposed dynamic MPPT controller, the bandwidth can be adjusted according to the rotor speed for obtaining more uniform dynamic response. Consequently, if the bandwidth is designed to be kept constant for achieving more uniform dynamics, the adaptive compensation gain should change with the rotor speed as follows.

$$k_f = f(w_m) = 1 - \frac{w_B - B/J}{k_M w_m} \tag{3.42}$$

In fact, the adaptive compensation gain calculator (ACGC) as shown in block C is implemented according to (3.42).

As an illustration of the merit of the proposed MPPT controller, consider the specific situation of the step change of wind velocity from V_{w1} to V_{w2} or vice versa. Due to the inertia of the WPGS, the generator speed cannot follow immediately the sudden speed change. For a conventional MPPT controller, the kw_m^2 command is adopted during the transient state as shown in Fig. 3.5. However, as the wind velocity is suddenly changed to V_{w2}, the truly optimal command is located at point B. In other words, the solid trajectory between A and B is not the truly optimal trajectory. Hence, by using the conventional MPPT controller, the WPGS will be accelerated only by the torque difference between the input wind torque and the kw_m^2 command torque. In other words, the dynamic response of accelerating to the truly optimal operation point B will be rather slow. On the other hand, by using the proposed MPPT controller, due

to the adaptive compensation, the torque command will be made smaller instantly than that of the conventional OT controller to increase the torque difference for faster accelerating to the truly optimal operation point B. Similarly, if the wind velocity is changed suddenly from V_{w2} to V_{w1}, contrast to the conventional OT controller, the torque command of the proposed MPPT controller will be made larger instantly for quickly decelerating the WPGS to the optimal point A. Consequently, the amount of the captured wind energy during the wind speed variation period can be increased significantly by using the proposed MPPT controller.

3.4 Simulation Results

To evaluate the performance of the proposed dynamic MPPT controller, the wind turbine, PM generator and proposed control algorithm are all established with Matlab/Simulink. First, the input torque estimator is simulated and some results are given in Fig. 3.6 to evaluation the performance under pulse changing wind speed. Then, to demonstrate the function of the proposed dynamic MPPT controller, the system is simulated under pulse changing wind speed and the corresponding simulation results is shown in Fig. 3.7. One can see that when the wind speed is changing from 6 m/s to 8 m/s, the generator torque command in the proposed MPPT controller is instantly kept smaller than that in the conventional OT controller. On the contrary, as the wind speed is slowing down, the torque command will become larger for more quickly decelerating the wind turbine. As a result, the dynamic response of the wind turbine will be greatly improved while the proposed controller is adopted. Fig. 3.7(c) and (d) show the respective recovery time to optimal value in rotating speed and power coefficient. The required recovery time of the system with proposed dynamic controller is obviously shortened. After one pulse changing period of wind speed, the total output energy of the wind turbine is increased about x% by using the

proposed controller.

Next, a more practical wind speed variation is given according to [20][21],

$$v_w(t) = 6.25[1 + 0.09\sin(\frac{2p}{20}t) + 0.15\sin(\frac{2p}{50}t)] \tag{3.43}$$

From (3.37), the mechanical dynamic bandwidth of the used wind turbine is obtained about 0.03 Hz. It turns out that the wind turbine with a conventional OT MPPT controller will be unable to track the high frequency term of wind speed variation in (3.43). The wind energy of the high frequency term will be lost. If the proposed dynamic MPPT controller is adopted, the bandwidth can then be extended by adjusting the virtual inertia with the dynamic compensation shown in Fig.3.4. The simulation results of proposed controller and conventional controller under wind speed variation in (3.43) are shown in Fig. 3.8. Not only the dynamic response but also the output energy are obviously improved if the proposed dynamic controller is aopdted.

Moreover, to further evaluate the performance of the proposed controller under gusty wind speed situation, a simulation case is carried out with the wind speed expressed as follows [21].

$$v_w(t) = V_w + v_g(t) \tag{3.44}$$

where V_w is the mean value of the wind velocity and $v_g(t)$ is the model of the wind gust which can be defined by the following equation.

$$v_g(t) = \frac{2v_{g\max}}{1 + e^{-4(\sin(w_g t)-1)}} \tag{3.45}$$

where $v_{g\max}$ is the gust amplitude and $w_g = 2p / T_g$ is the gust frequency. In this simulation, the mean value of the wind velocity is considered as 6 m/s, the gust amplitude is taken as 25% and the period, T_g, is chosen to be 10s. To make the simulation results more close to the implementation, the relative parameters are all chosen to follow closely the practical system parameters as shown in Table 3.1. Fig. 3.9 shows the simulated dynamic response of the proposed and the conventional systems to the gusty wind velocity as mentioned above. It is seen that the dynamic response of the rotor speed of the wind turbine is greatly improved and the resulting power coefficient of the proposed WPGS also can be maintained more closely to optimal value more rapidly.

Table 3.1
The system parameters of the proposed small WPGS

Radius of the wind turbine r	0.5 m
Total inertia J	0.4 $k_g \cdot m^2$
Viscous damping coefficient B	0.008
Rated Power	200 w
Rated wind speed	12.5 m/s
Stator inductance L_s	70 uH
Boost inductor L	22 uH
Filter capacitor C_f	4.7 uF
Maximum power coefficient $C_{p,max}$	0.2812
Optimal TSR d_{opt}	3.53

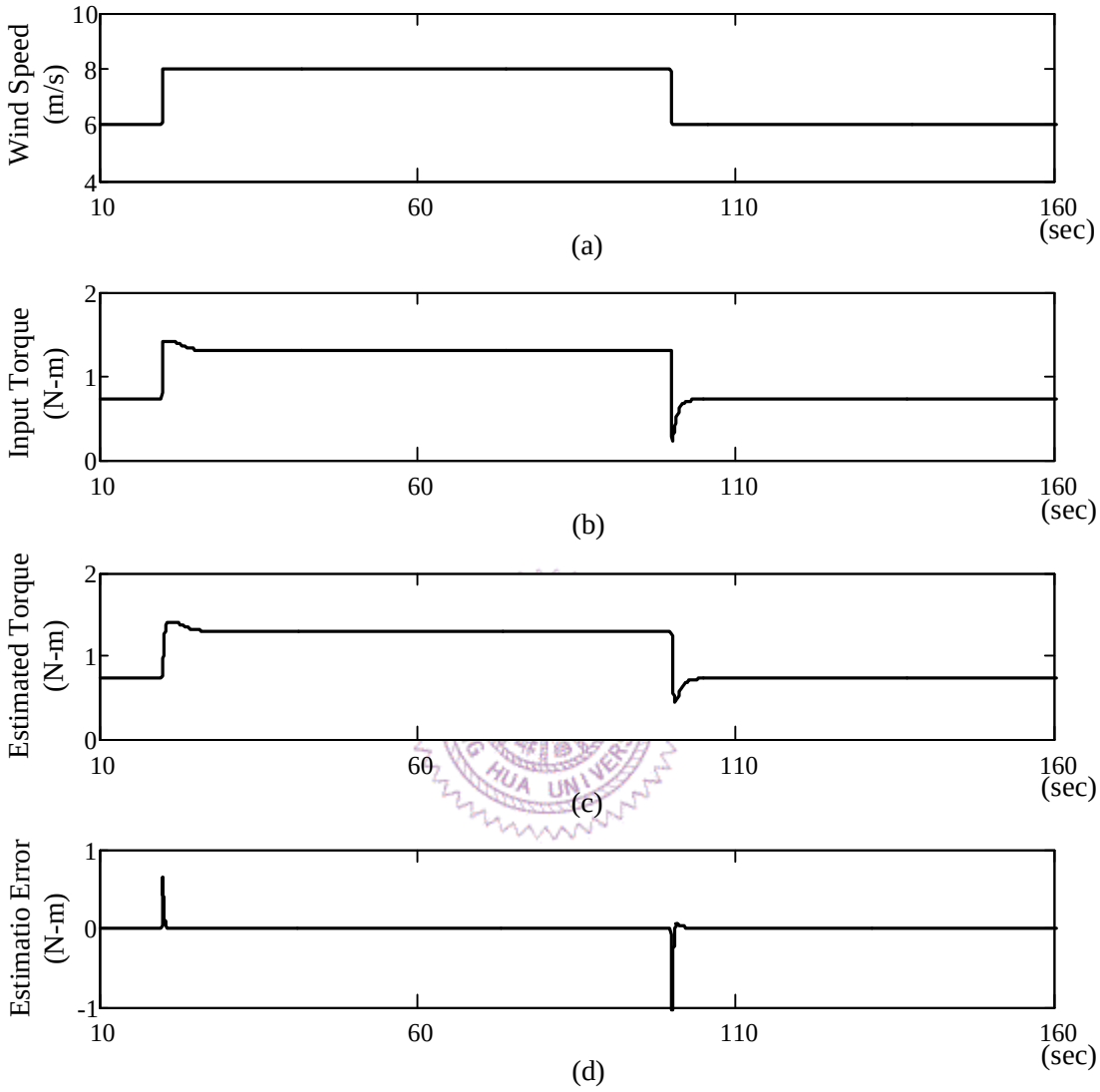

Fig. 3.6 Simulation results of the input torque estimator under step changing wind speed. (a) Wind speed (m/s), (b) actual input torque (Nm), (c) estimated input torque (Nm) and (d) estimation error of input torque (Nm).

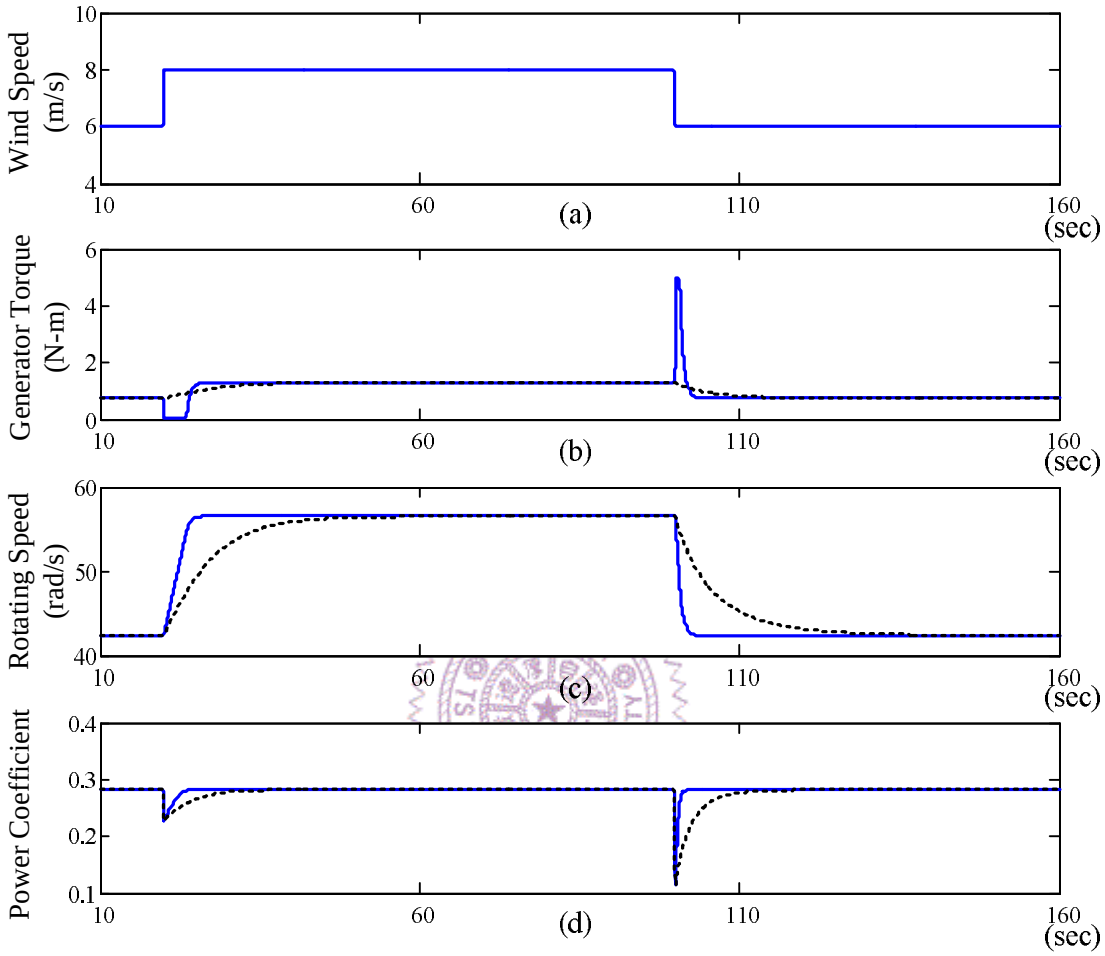

Fig. 3.7 Simulation results in pulse changing wind speed. (a) Wind speed (m/s), (b) generator torque (Nm), (c) rotating speed (rad/s) and (d) power coefficient. (Solid line: proposed controller, dashed line: conventional controller.)

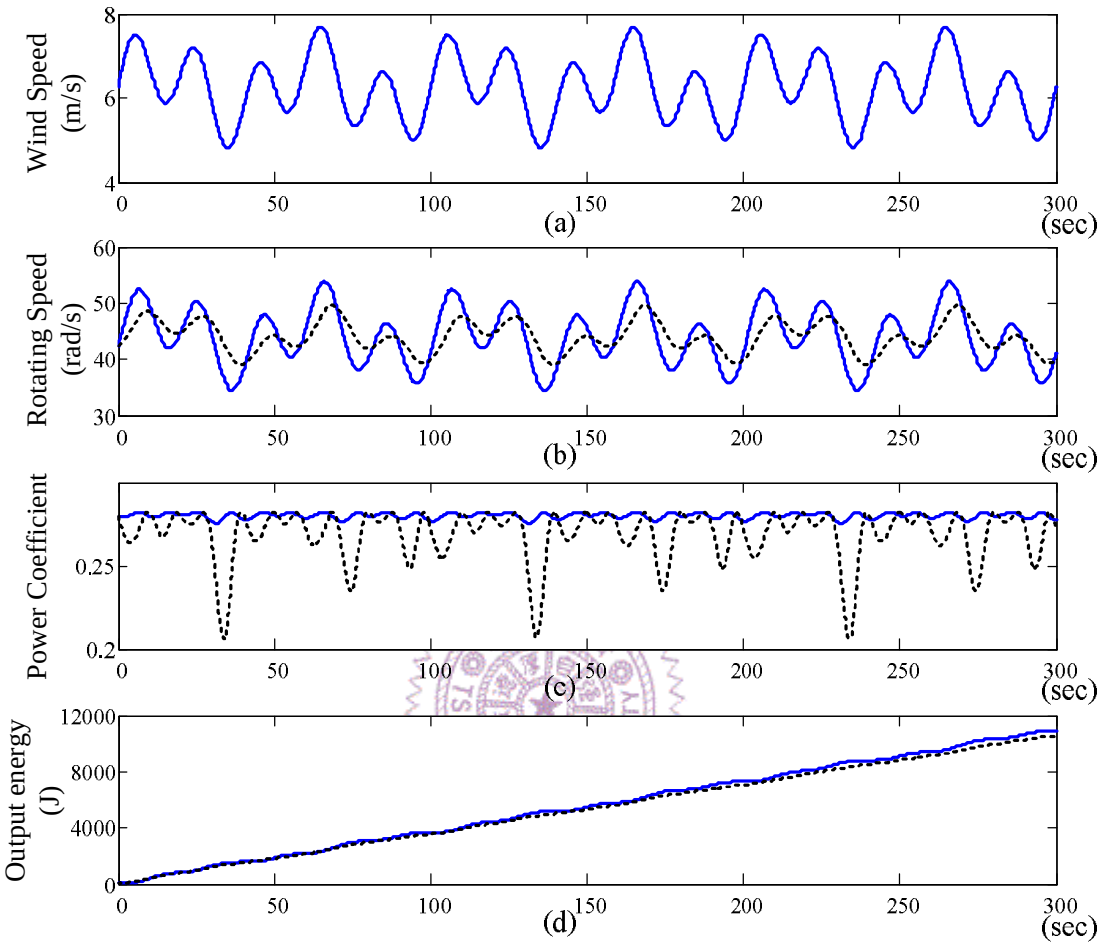

Fig. 3.8 Simulation results in wind speed variation. (a) Wind speed (m/s), (b) rotating angular speed (rad/s), (c) power coefficient Cp and (d) output energy (J). (Solid line: proposed controller, dashed line: conventional controller.)

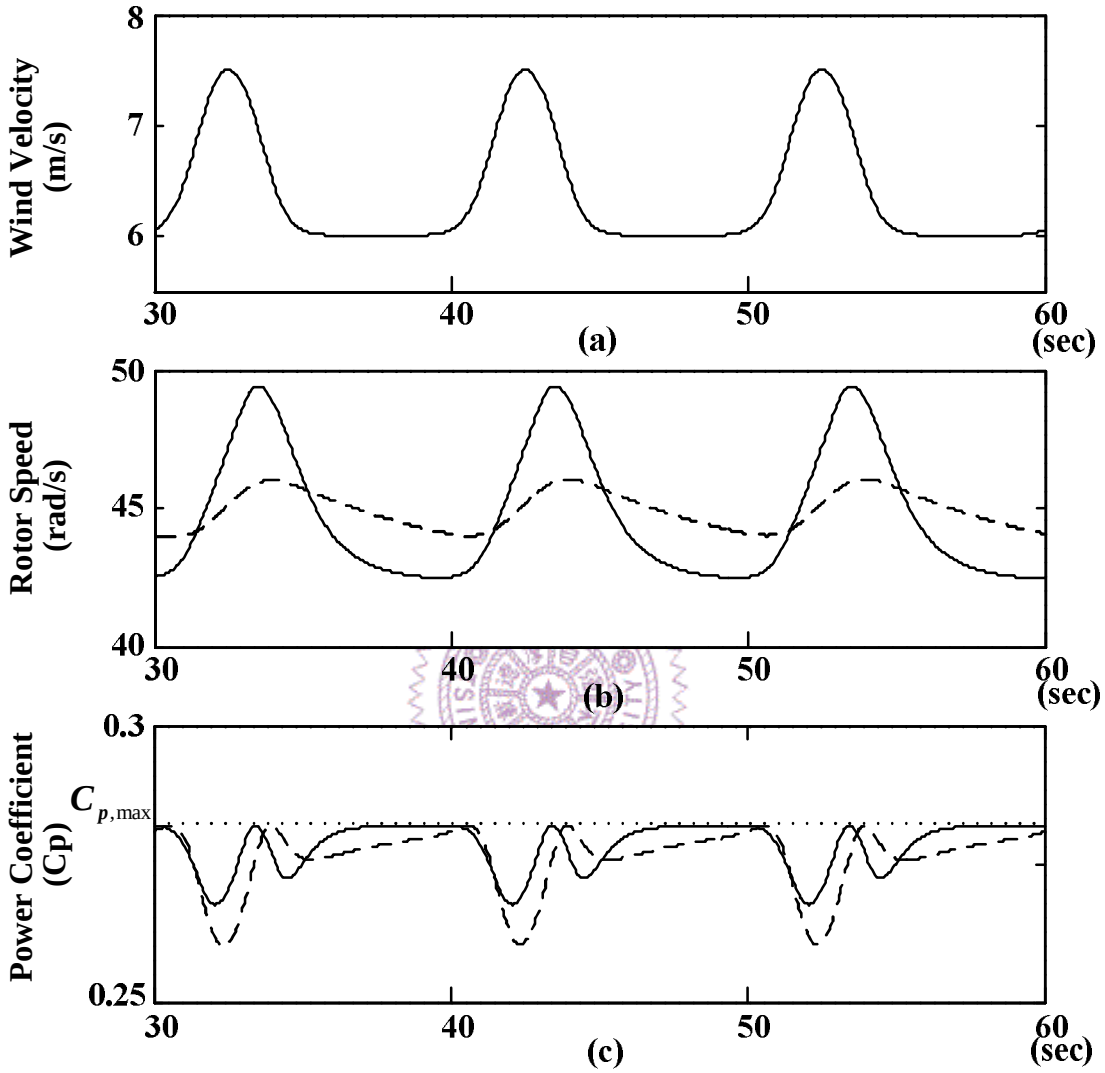

Fig. 3.9 Simulation results of the gusty wind speed variation. (a) Wind speed (m/s), (b) rotating speed (rad/s) and (c) power coefficient Cp. (Solid line: proposed controller, dashed line: conventional controller.)

CHAPTER 4

THREE PHASE SINGLE STAGE AC TO DC CONVERTER WITH QSR TECHNIQUE

4.1 Introduction

Although the two-stage converter composed of a three-phase full-bridge diode rectifier and a dc converter is simple and economical, the current harmonic distortion and power losses are rather significant. To eliminate these drawbacks of the conventional system and remain the simplicity and cheapness, a single-stage three-phase quasi-synchronous rectification (QSR) ac to dc converter is proposed in this chapter to replace the conventional two-stage converter. The operation principle of the proposed converter will be illustrated in the following paragraphs.

In section 4.2, the discontinuous conduction mode (DCM) power factor correction (PFC) technique and the configuration of the proposed converter are both introduced. Then, to further reduce the conduction losses of the body diodes, the QSR technique for controlling the proposed converter is proposed in the third section. Moreover, an alternative hybrid control methodology, namely the CCM/DCM integrated control, is also proposed for the proposed converter in section 4.4. Finally, some simulations and experiments are carried out to evaluate the validity and performance of the proposed converter.

4.2 Discontinuous Conduction Mode Power Factor Correction Technique

From the viewpoint of control, DCM PFC technique is more convenient and simpler than continuous conduction mode PFC technique. One basic topology of

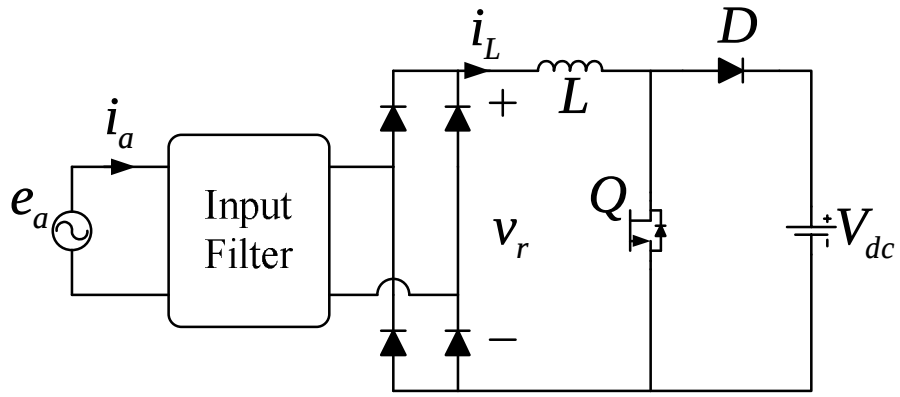

Fig. 4.1 Basic topology of a single phase DCM PFC converter.

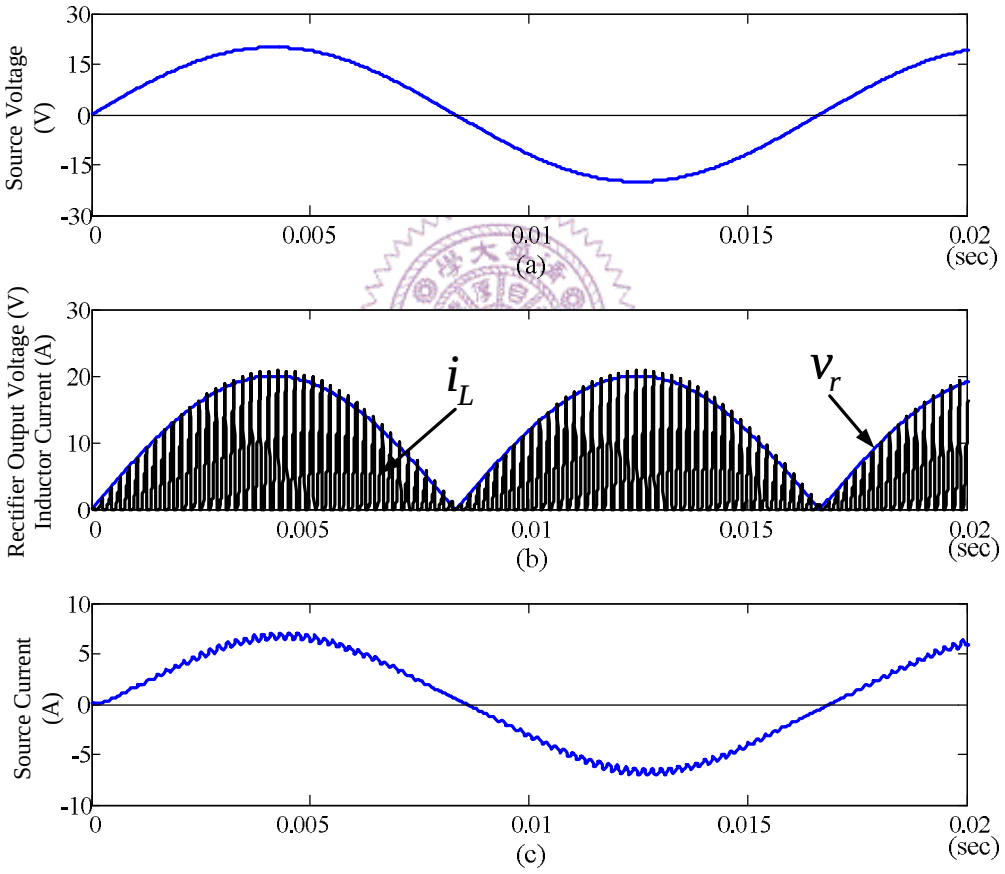

Fig. 4.2 Waveforms in single phase DCM PFC converter. (a) Source voltage e_a, (b) rectifier output voltage v_r and inductor current i_L, (c) Source inductor i_a.

single phase DCM active PFC converter is composed of an input filter, a diode rectifier and a boost dc converter as shown in Fig. 4.1 [22][23]. The inductor current

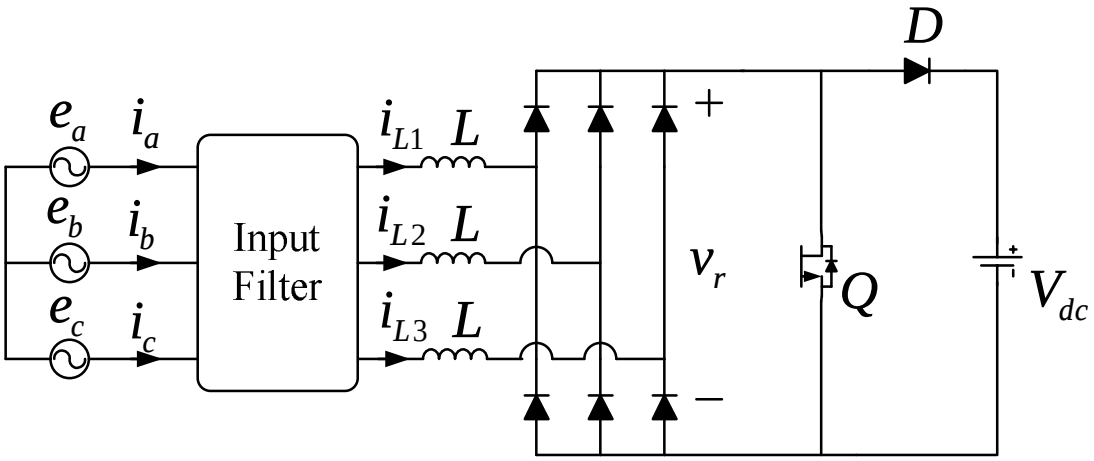

Fig. 4.3 Topology of a three phase single switch DCM PFC converter.

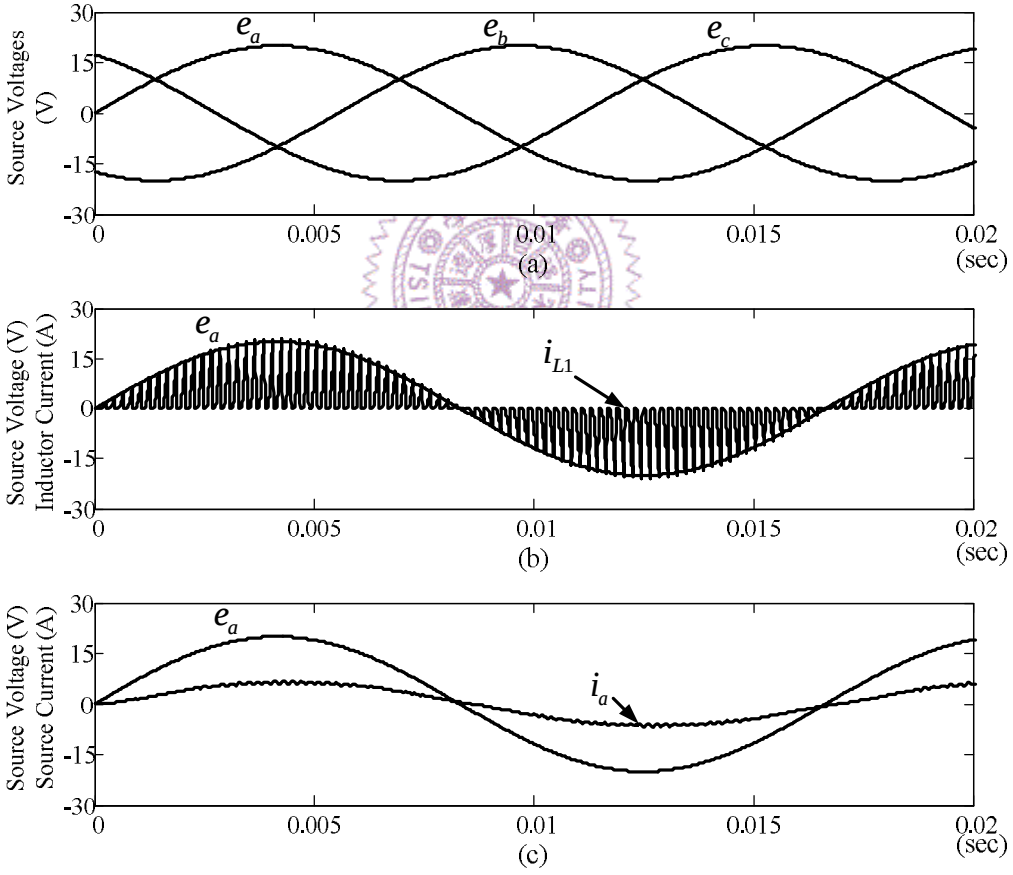

Fig. 4.4 Waveforms in the three phase single switch DCM PFC converter. (a) Three phase voltages, (b) source voltage and inductor current, (c) source voltage and source current.

is always controlled in DCM. Fig. 4.2 shows the relative waveforms of the single phase DCM PFC technique. In the positive half line cycle, diodes D_1, D_4 are turned on, and D_2, D_3 are turned off. While the active switch is turned on, the stored energy in the inductor will be increased, i.e., the inductor current will increase from zero with a rate proportional to the rectified voltage v_r. Then, the active switch is turned off to transfer the pre-stored energy in the inductor to the output. And the gating signal for turning on the active switch will be triggered after totally releasing pre-stored energy. As a result, if the duty ratio of the active switch is remained constant, the peak current will automatically follow the rectifier output voltage v_r. Then, the input current $i(t)$ will be nearly sinusoidal and unity power factor by filtering out the high frequency components with a input filter.

The single phase DCM PFC technique can be directly extended to the three phase systems as well. One of the well-known three phase DCM PFC technique is proposed in [24] and the configuration of the converter is shown in Fig. 4.3. The three phase rectifier is composed of a three phase input filter, three boost inductors, a three phase diode rectifier, an active switch, output diode, dc side capacitor and load. The input filter is used to prevent the current ripple components with switching frequency getting into the ac source. The boost inductor currents should be decrease to zero in each switching cycle before next turning on. During the turned on interval, the three boost inductors are shorted through diode rectifier and active switche. Then, the three phase voltage sources will increase the energy stored in the three inductors, the increasing rates of three inductors currents will be proportional to the three phase voltages respectively. When the active switch is turned off, the energy pre-stored in three inductors will be transferred to the load. Therefore, the peak currents will also be proportional to the respective phase voltages if the switch duty ratio is kept constant. It turns out that the fundamental components of the discontinuous currents

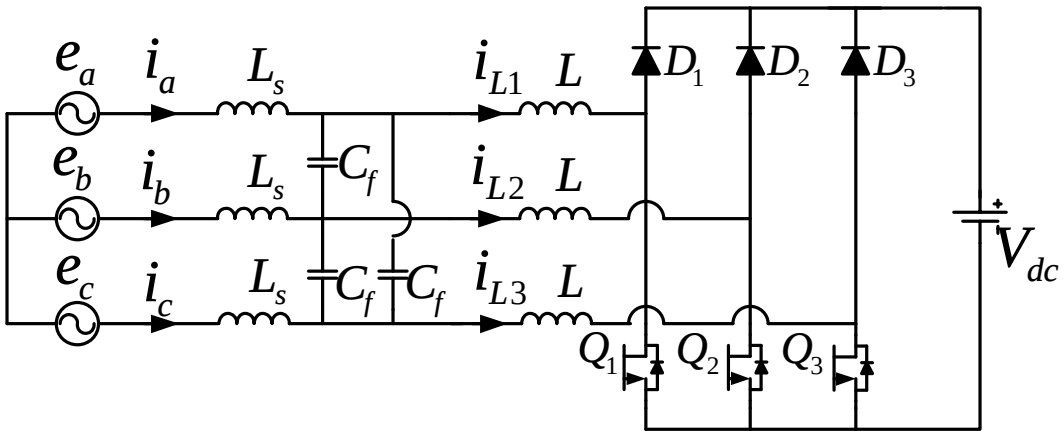

Fig. 4.5 Topology of the proposed three phase single stage DCM PFC converter.

will be nearly sinusoidal and be in phase with the phase voltages. The other high frequency components are undesired and harmful for the generator. Therefore, a three phase filter is integrated to filter out the high frequency components resulting from DCM operation. The design of the filter would not be difficult because the switching frequency is normally much higher than the line frequency. Fig. 4.4 shows the waveforms of the source voltage, current and the discontinuous current.

In the proposed WPGS, a half-controlled rectifier shown in Fig. 4.5 is adopted to reduce the conduction losses of the diodes by using three active switches to replace the low side diodes in single switch type rectifier. The half-controlled rectifier is composed of a three phase input filter, three boost inductors, three diodes and three active switches. With basic DCM operation, the three active switches are synchronously gated. In the turned on interval, the energy of the inductors is increased and the boost inductors are shorted only through three active switches to lower the conduction losses. However, during the energy transferring from the boost inductors to the output in the turned off interval, the currents will still flow through the up side diodes and the body diodes. To further reduce the conduction losses caused by the body diodes in the turned off interval, a novel quasi-synchronous rectification (QSR) technique is proposed and described in the next section.

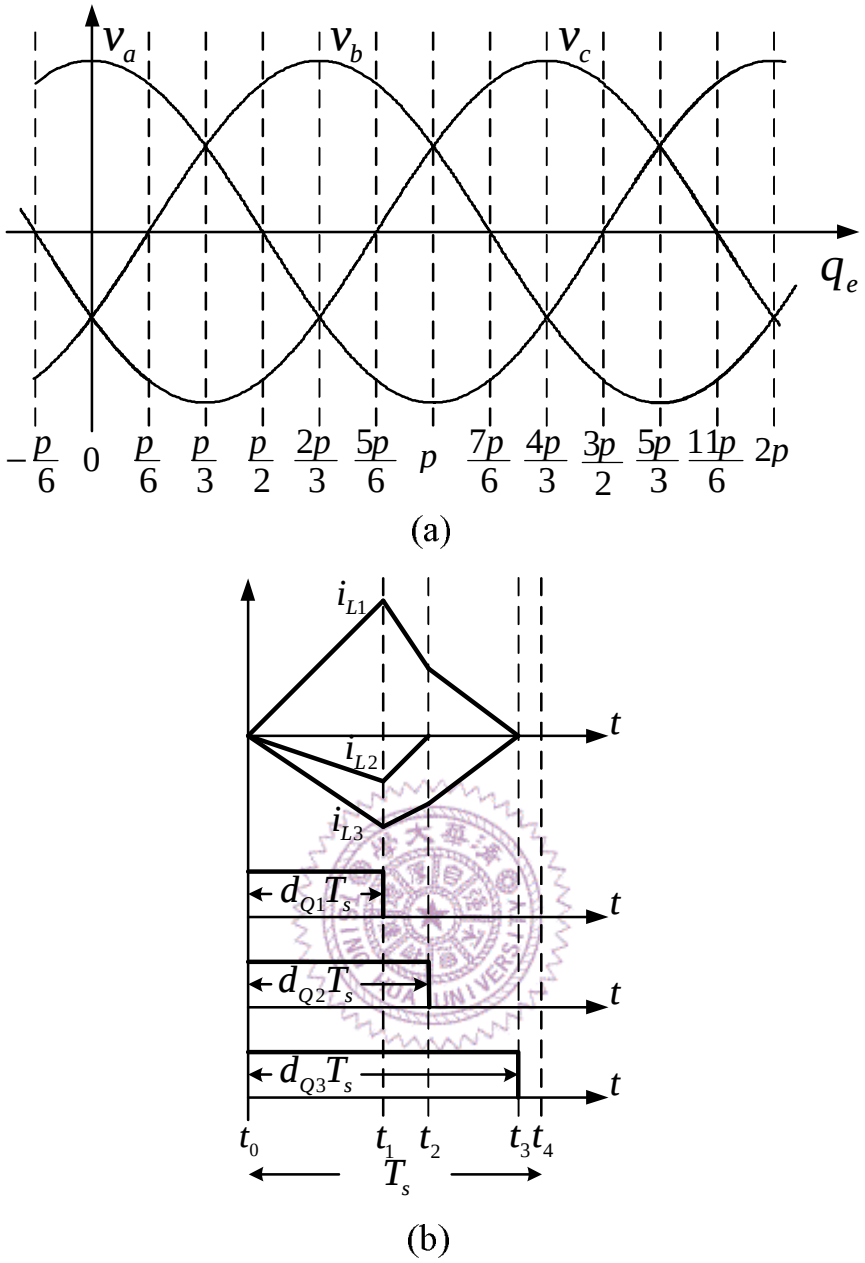

Fig. 4.6 Waveforms in proposed converter. (a) Twelve intervals, (b) three phase DCM currents and three active switch gating signals.

4.3 Operation Principles of the Quasi-Synchronous Rectification DCM Control

The novel QSR technique is proposed for extending the turned on time of corresponding active switches in DCM operation to further reduce the conduction

losses. For convenient illustration of the QSR technique, the following assumptions are given first.

(1) The switching frequency is much higher than the electrical frequency of the voltage sources.

(2) The devices are considered as ideal components except the forward voltage drop of the diodes.

(3) The terminal phase voltages can be approximated by three phase back EMFs.

The three phase voltages shown in Fig. 4.6(a) can be divided into twelve intervals. The proposed rectifier is analyzed in the interval $0 \le q_e \le p/6$ as an example to illustrate the proposed quasi-synchronous rectification technique for controlling the three active switches. The waveforms of the inductor currents and the gating signals in one switching period are shown in Fig. 4.6(b). There are four operation modes for the proposed rectifier in one switching period and the equivalent circuits of the operation modes shown in Fig. 4.7 are analyzed as follows.

(1) **Mode I ($t_0 \le t \le t_1$) :**

In the first operation mode, all the active switches are turned on simultaneously for increasing the energy stored in the three inductors. The corresponding equivalent circuit is shown in Fig. 4.7(a). Hence, the inductor currents can be expressed as follows.

$$\bar{\mathrm{i}}(t) = \frac{(t-t_0)}{L} \cdot \bar{\mathrm{v}}(t) \tag{4.1}$$

$$\bar{i}(t) = [i_1(t) \quad i_2(t) \quad i_3(t)]^T \tag{4.2}$$

$$\bar{\mathrm{v}}(t) = [v_a(t) \quad v_b(t) \quad v_c(t)]^T \tag{4.3}$$

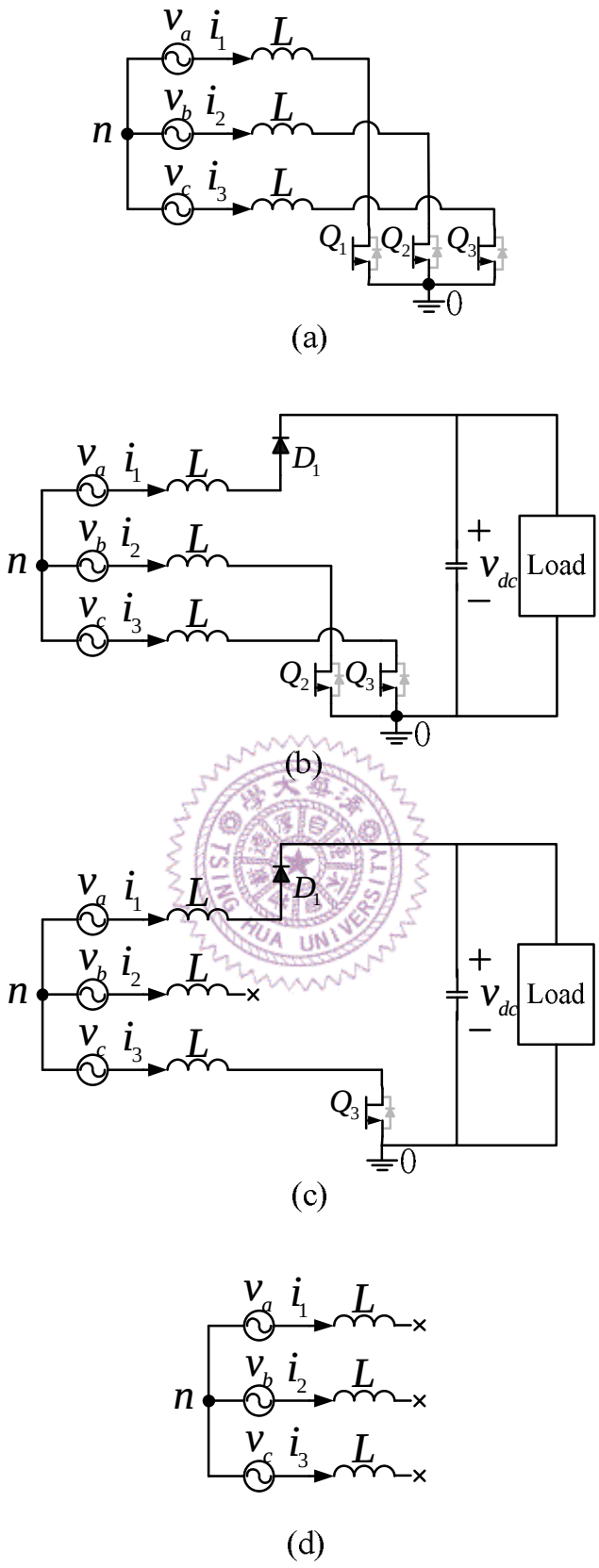

Fig. 4.7 Equivalent circuits of four operation modes in one switching period. (a) Mode I, (b) Mode II, (c) Mode III, (d) Mode IV.

The first operation mode is ended at $t = t_1$ and the peak value of the inductor currents is given by

$$\bar{i}(t_1) = \frac{d_1 T_s}{L} \cdot \bar{v}(t_1) \tag{4.4}$$

$$d_1 = (t_1 - t_0) / T_s \tag{4.5}$$

where d_1 is the duty ratio of the first operation mode and T_s denotes the switching period. According to (4.4), one can see that if the duty ratio d_1 is constant, the peak values of the three inductor currents will be proportional to the magnitude of the three phase voltages respectively as shown in Fig. 4.4. Therefore, after filtering out the high frequency components, the generator output currents will nearly be sinusoidal and in phase with the phase voltages.

(2) Mode II ($t_1 \le t \le t_2$) :

During the second operation mode, the active switch Q_1 is turned off but the other switches Q_2 and Q_3 are still turned on as shown in Fig. 4.7(b) to reduce the conduction loss caused by body diodes. The energy stored in the three inductors is decreased and the corresponding dynamic equations are given as follows.

$$L\frac{di_1}{dt} = v_a - V_{df} - V_{dc} - v_{on} \tag{4.6}$$

$$L\frac{di_2}{dt} = v_b - v_{on} \tag{4.7}$$

$$L\frac{di_3}{dt} = v_c - v_{on} \tag{4.8}$$

The three phase voltages are assumed to be balanced and the neutral point is floating. The voltage between the ground and the neutral point can be obtained as

$$v_{on} = -\frac{1}{3}(V_{df} + V_{dc}) \tag{4.9}$$

Then, by substituting (4.9) into (4.6)-(4.8), one can get the following expression.

$$L\frac{d\bar{i}(t)}{dt} = \bar{v}(t) + H \cdot V_{eq} \tag{4.10}$$

$$H = [-\frac{2}{3} \quad \frac{1}{3} \quad \frac{1}{3}]^T \tag{4.11}$$

where V_{df} is the forward voltage drop of the diode and $V_{eq} = V_{df} + V_{dc}$ is defined as the equivalent dc voltage. Consequently, the three inductor currents in the second mode are expressed as

$$\bar{i}(t) = \frac{t - t_1}{L}[\bar{v}(t) + \mathrm{H} \cdot V_{eq}] + \bar{i}(t_1) \tag{4.11}$$

The magnitude of the inductor current $i_2(t)$ will decrease to zero at $t = t_2$ and the second mode is ended at the same time. The duty ratio of the second operation mode can be derived as

$$d_2 = \frac{t_2 - t_1}{T_s} = \frac{-3v_b d_1}{V_{eq} + 3v_b} \tag{4.12}$$

At the end of the mode II, the active switch Q_2 is turned off and the values of the other inductor currents at $t = t_2$ can be obtained as

$$d_2 = \frac{t_2 - t_1}{T_s} = \frac{-3v_b d_1}{V_{eq} + 3v_b} \tag{4.13}$$

(3) Mode III ($t_2 \le t \le t_3$) :

In the third operation mode, the active switches Q_1 and Q_2 are turned off and

the other switch Q_3 is still turned on as shown in Fig. 4.7(c). The magnitudes of the inductor currents i_1 and i_3 are continuously decreased and the mathematical expressions are given as

$$L\frac{di_1}{dt} = v_a - V_{eq} - v_{on} \tag{4.14}$$

$$L\frac{di_3}{dt} = v_c - v_{on} \tag{4.15}$$

$$v_{on} = (v_a + v_c - V_{eq})/2 \tag{4.16}$$

Then the two inductor currents in the third mode can be derived as

$$i_1(t) = -i_3(t) = \frac{v_a - v_c - V_{eq}}{2L} \cdot (t - t_2) + i_1(t_2) \tag{4.17}$$

The magnitudes of the two inductor currents will be decreased to zero at the end of the third operation mode simultaneously. Then the duty ratio of the third operation mode $d_3 = (t_3 - t_2)/T_s$ can be derived as

$$d_3 = \frac{-2V_{eq}(v_b - v_c)}{(V_{eq} + 3v_b)(v_a - v_c - V_{eq})} \cdot d_1 \tag{4.18}$$

(4) Mode IV ($t_3 \le t \le t_4$) :

In the last mode, the three active switches are all turned OFF and the inductor currents become zero as illustrated in Fig. 4.7 (d).

The gating signals of the three active switches are shown in Fig. 4.6(b). The proposed quasi-synchronous rectification technique is to extend the turned on time of respective active switches for reducing the conduction loss. The mathematical

expressions of the duty ratio determined by the quasi-synchronous rectification technique in the interval $0 \le q_e \le p/6$ are summarized as follows.

$$d_{Q1} = d_1 \tag{4.19}$$

$$d_{Q2} = d_1 + d_2 = d_1 \frac{V_{eq}}{V_{eq} + 3v_b} \tag{4.20}$$

$$d_{Q3} = d_1 + d_2 + d_3 = d_1 \frac{V_{eq}}{V_{eq} - (v_a - v_c)} \tag{4.21}$$

Finally, according to the symmetrical characteristic of the three phase balance system, the analytic equations of the corresponding duty ratios in one line cycle can be expressed as follows. The extended turned-on time for the respective switches can be determined straightforward from the derived analytic equations of the duty ratios.

$$d_{Q1} = \begin{cases} d_1 & , \ 0 < \theta_e \le \dfrac{\pi}{2} \ and \ \dfrac{3\pi}{2} < \theta_e \le 2\pi \\ \dfrac{V_{eq}}{V_{eq} + 3v_a} d_1 & , \ \dfrac{\pi}{2} < \theta_e \le \dfrac{2\pi}{3} \ and \ \dfrac{4\pi}{3} < \theta_e \le \dfrac{3\pi}{2} \\ \dfrac{V_{eq}}{V_{eq} - (v_b - v_a)} d_1 & , \ \dfrac{2\pi}{3} < \theta_e \le \pi \\ \dfrac{V_{eq}}{V_{eq} - (v_c - v_a)} d_1 & , \ \pi < \theta_e \le \dfrac{4\pi}{3} \end{cases} \tag{4.22}$$

$$d_{Q2} = \begin{cases} \dfrac{V_{eq}}{V_{eq} + 3v_b} d_1 & , \ 0 < \theta_e \le \dfrac{\pi}{6} \ and \ \dfrac{7\pi}{6} < \theta_e \le \dfrac{4\pi}{3} \\ d_1 & , \ \dfrac{\pi}{6} < \theta_e \le \dfrac{7\pi}{6} \\ \dfrac{V_{eq}}{V_{eq} - (v_c - v_b)} d_1 & , \ \dfrac{4\pi}{3} < \theta_e \le \dfrac{5\pi}{3} \\ \dfrac{V_{eq}}{V_{eq} - (v_a - v_b)} d_1 & , \ \dfrac{5\pi}{3} < \theta_e \le 2\pi \end{cases} \tag{4.23}$$

$$d_{Q3}=\begin{cases}\dfrac{V_{eq}}{V_{eq}-(v_a-v_c)}d_1 \;,\; 0<\theta_e\le\dfrac{\pi}{3}\\ \dfrac{V_{eq}}{V_{eq}-(v_b-v_c)}d_1 \;,\; \dfrac{\pi}{3}<\theta_e\le\dfrac{2\pi}{3}\\ \dfrac{V_{eq}}{V_{eq}+3v_c}d_1 \;,\; \dfrac{2\pi}{3}<\theta_e\le\dfrac{5\pi}{6}\ and\ \dfrac{11\pi}{6}<\theta_e\le 2\pi\\ d_1 \;,\; \dfrac{5\pi}{6}<\theta_e\le\dfrac{11\pi}{6}\end{cases} \tag{4.24}$$

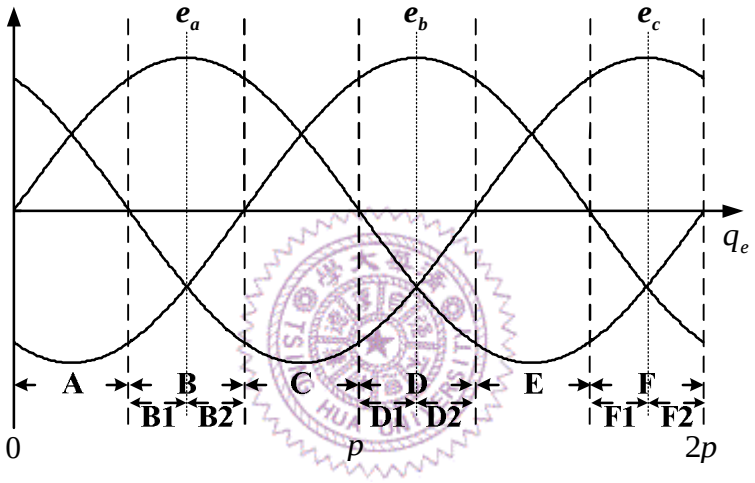

Fig. 4.8 The defined intervals in one line cycle.

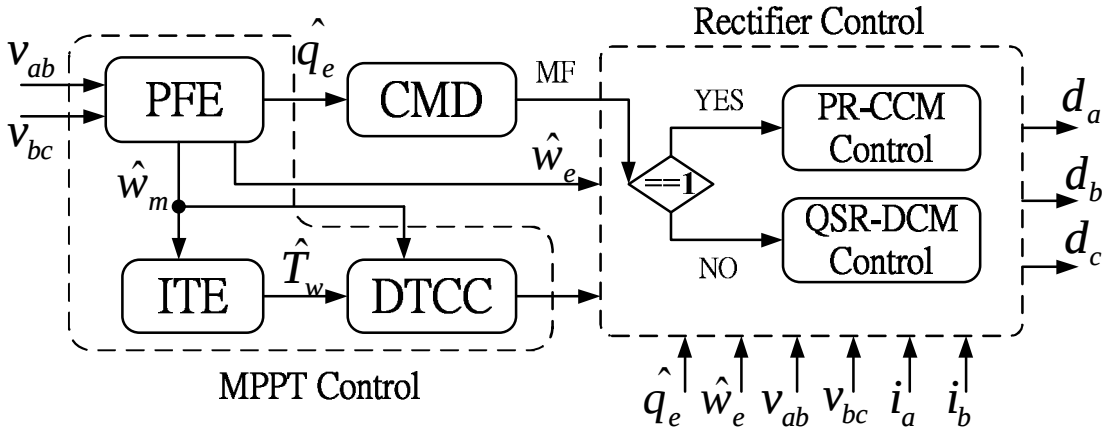

Fig. 4.9 The block diagram of proposed hybrid control.

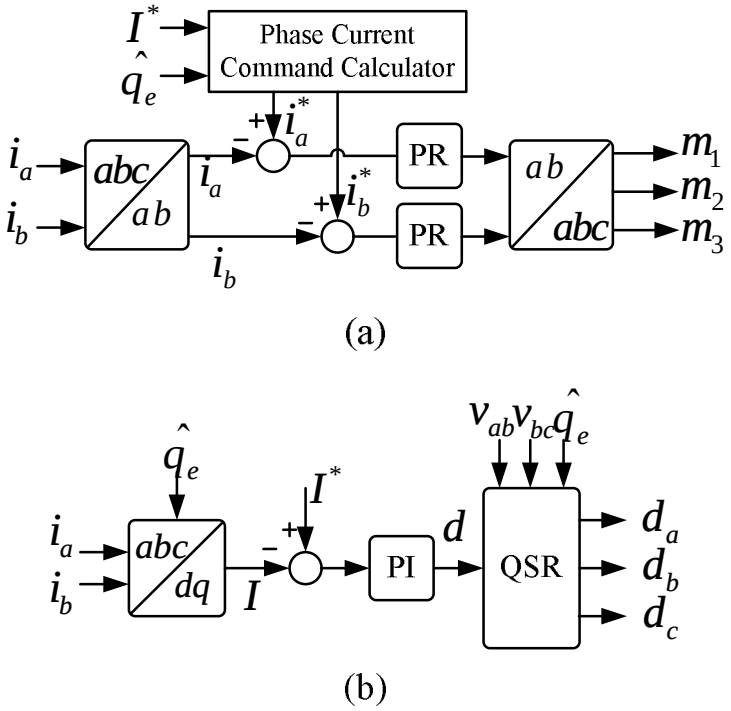

Fig. 4.10 The block diagrams of (a) CCM control with PR controller, (b) QSR-DCM control with PI controller.

4.4 A Novel Hybrid Control of CCM, DCM and QSR Techniques

While this half-controlled rectifier is controlled with CCM operation, it is seen that the phase currents are only controllable in the positive half cycle. In the negative half cycle, the phase currents cannot be fully controlled. To realize the operation principles, a line cycle can be divided into six intervals as shown in Fig. 4.8. The three phase currents are fully controllable with CCM control mode only in intervals A, C and E. While in the rest intervals, due to the unidirectional current flow capability of the diodes, the phase currents can no longer be controlled by Q_1, Q_2 and Q_3. Fortunately, as mentioned in previous section, the currents are all controllable even in the negative half interval. Therefore, one can change the operation mode of the rectifier into DCM control to make the negative currents automatically following the phase voltages. In other words, the proposed hybrid control is composed partial CCM

control and partial DCM control. The block diagram of the hybrid control is shown in Fig. 4.9. The rectifier is controlled with CCM operation in intervals A, C and F, and DCM operation in the rest intervals. While in the CCM operation, one of the three switches will be always turned on and the other two switches are controlling with PR controller to eliminate the tracking error. When in DCM operation, the three switches are controlled with DCM QSR technique and a PI controller is integrated to eliminate the steady state error of the current amplitude.

In the CCM control mode, the current ripple and switching losses are much less than that in the DCM control mode. However, in the CCM control mode each phase current is only controllable in the positive half cycle. Fig. 4.10(a) shows the block diagram of the CCM control mode. The transfer function of the adopted non-ideal proportional-resonant controller [25][26] can be expressed as follows.

$$G_{PR}(s) = K_p + \frac{2K_r w_c s}{s^2 + 2w_c s + w_r^2} \tag{4.25}$$

where K_p and K_r are the gain coefficients of the proportional and resonant controls respectively, w_r is the resonant frequency of the controller, and w_c is the cut-off frequency. The bandwidth can be appropriately adjusted by setting the cut-off frequency to improve the stability of the control loop. In this paper, a digital signal processor, namely TMS320 F2812, is adopted for implementing the proposed controller. By using the backward transformation technique ($1/s = T_s/(1-z^{-1})$), the z-domain transfer function of the PR controller for digital implementation can be obtained from (4.25) and expressed as follows.

$$G_{PR}(z) = K_p + \frac{Y(z)}{E(z)} = K_p + K_r \frac{a_0 + a_1 z^{-1}}{b_0 + b_1 z^{-1} + z^{-2}} \tag{4.26}$$

$$a_0 = -a_1 = 2w_c T_s$$

$$b_0 = 1 + 2w_c T_s + w_r^2 T_s^2$$

$$b_1 = -2 - 2w_c T_s$$

The corresponding difference equation of the resonant loop can be derived as follows

$$y[n] = \frac{\{K_r a_0 (e[n] - e[n-1]) - b_1 y[n-1] - y[n-2]\}}{b_0} \tag{4.27}$$

where n is the sampling point.

To describe the operation principle of the CCM control mode, interval A is taken as an example. In this interval, the phase voltages v_{an} and v_{cn} are in the positive half cycle so that the corresponding phase currents i_a and i_c can be controlled to follow the following commands.

$$i_a^* = I \sin q_e \tag{4.28}$$

$$i_c^* = I \sin(q_e + 2p\ /3) \tag{4.29}$$

The state averaged dynamic equations of the phase currents can be expressed as follows.

$$e_a = L_t \frac{di_a}{dt} + R_s i_a + v_{An} \tag{4.30}$$

$$e_c = L_t \frac{di_c}{dt} + R_s i_c + v_{Cn} \tag{4.31}$$

$$v_{An} = m_1 v_{dc} = (2v_{A0} - v_{C0})/3 \tag{4.32}$$

$$v_{Cn} = m_3 v_{dc} = (-v_{A0} + 2v_{C0})/3 \tag{4.33}$$

$$v_{A0} = \bar{d}_a v_{dc} = (1 - d_a) v_{dc} \tag{4.34}$$

$$v_{C0} = \bar{d}_c v_{dc} = (1 - d_c) v_{dc} \tag{4.35}$$

where $L_t = L_s + L$ is the effective total inductor, m_1 and m_3 are the equivalent modulation indices of phases a and c, d_a and d_c are the duty ratios of the respective active switches Q_1 and Q_3. Hence, from (4.28) to (4.35), the analytic closed form of the duty ratio d_a and d_c can be obtained as follows.

$$m_1 = M \sin(w_e t - f) \tag{4.36}$$

$$m_3 = M \sin(w_e t - f + 2p / 3) \tag{4.37}$$

$$d_a = 1 - (2m_1 + m_3) = 1 - \sqrt{3} M \sin(w_e t - f + p / 6) \tag{4.38}$$

$$d_c = 1 - (m_1 + 2m_3) = 1 - \sqrt{3} M \sin(w_e t - q + p / 2) \tag{4.39}$$

$$M = \sqrt{(E - R_s I)^2 + (w_e L_t I)^2} \Big/ v_{dc}$$

$$f = \tan^{-1}\left(\frac{w_e L_t I}{E - R_s I}\right)$$

In this interval, switch Q_2 can be always turned ON to reduce the conduction loss. Finally, the closed form of the corresponding duty ratios of the other two CCM intervals can be summarized in Table 4.1.

Table 4.1

The duty ratios in the CCM control intervals

Interval	Duty Ratios
A	$d_a = 1 - (2m_1 + m_3) = 1 - \sqrt{3} M \sin(w_e t - f + p / 6)$ $d_b = 1$ $d_c = 1 - (m_1 + 2m_3) = 1 - \sqrt{3} M \sin(w_e t - q + p / 2)$

Table 4.1 (Continued)

The duty ratios in the CCM control intervals

C	$d_a = 1-(2m_1+m_2) = 1-\sqrt{3}M\sin(w_e t - f - p/6)$ $d_b = 1-(m_1+2m_2) = 1-\sqrt{3}M\sin(w_e t - f - p/2)$ $d_c = 1$
E	$d_a = 1$ $d_b = 1-(2m_2+m_3) = 1-\sqrt{3}M\sin(w_e t - f - 5p/6)$ $d_c = 1-(m_2+2m_3) = 1-\sqrt{3}M\sin(w_e t - f + 5p/6)$

4.5 Simulation results

Some simulations of the proposed converter are made with the simulation software PSIM and the corresponding results are given to evaluate the performance of the proposed single stage converter. The parameters of the converter are list as follows.

$L_s = 300\,mH$ $\quad$ $L = 100\,mH$

$C_f = 14.7\,mH$ $\quad$ $w_e = 120p\ rad/\sec$

$E = 12.8V$ $\quad$ $R_{DS} = 13m\Omega$

$V_{df} = 0.6V$ $\quad$ $V_{dc} = 200V$

The generator electrical angular frequency w_e is set to simulate that the system is under steady state at wind speed $V_w = 6.5\,m/s$. First, to compare the performance between the conventional two-stage converter and the proposed converter, the simulation of the conventional converter is also carried out and the results are shown

in Fig. 4.11. From Fig. 4.11(b) and (c), one can see there is serious harmonic distortion in the input current. Fig. 4.12 shows the simulation results of the proposed converter controlled by fully DCM operation and QSR technique. It can be seen that the input current is nearly sinusoidal and unit power factor. The simulation results of the converter operated with hybrid control are shown in Fig. 4.13. From Fig. 4.13(b), one can see that the converter is operated with CCM for only three intervals and DCM for the other intervals in one line cycle. Fig. 4.14 shows the instantaneous input power of the conventional two-stage converter, the proposed fully DCM controlled converter and proposed hybrid controlled converter. It is obvious that either the fully QSR DCM control or the hybrid control can both provide excellent improvement of the input power pulsation. The corresponding current THD and efficiency are listed in Table 4.2. From Table 4.2, it can be seen that the efficiency of the hybrid controlled converter is higher than that of the fully QSR DCM controlled converter, however, the hybrid control algorithm is a little more complex than the fully QSR DCM control. Therefore, depending on one's major considerations, simplicity or efficiency, one can choose the most suitable control strategy.

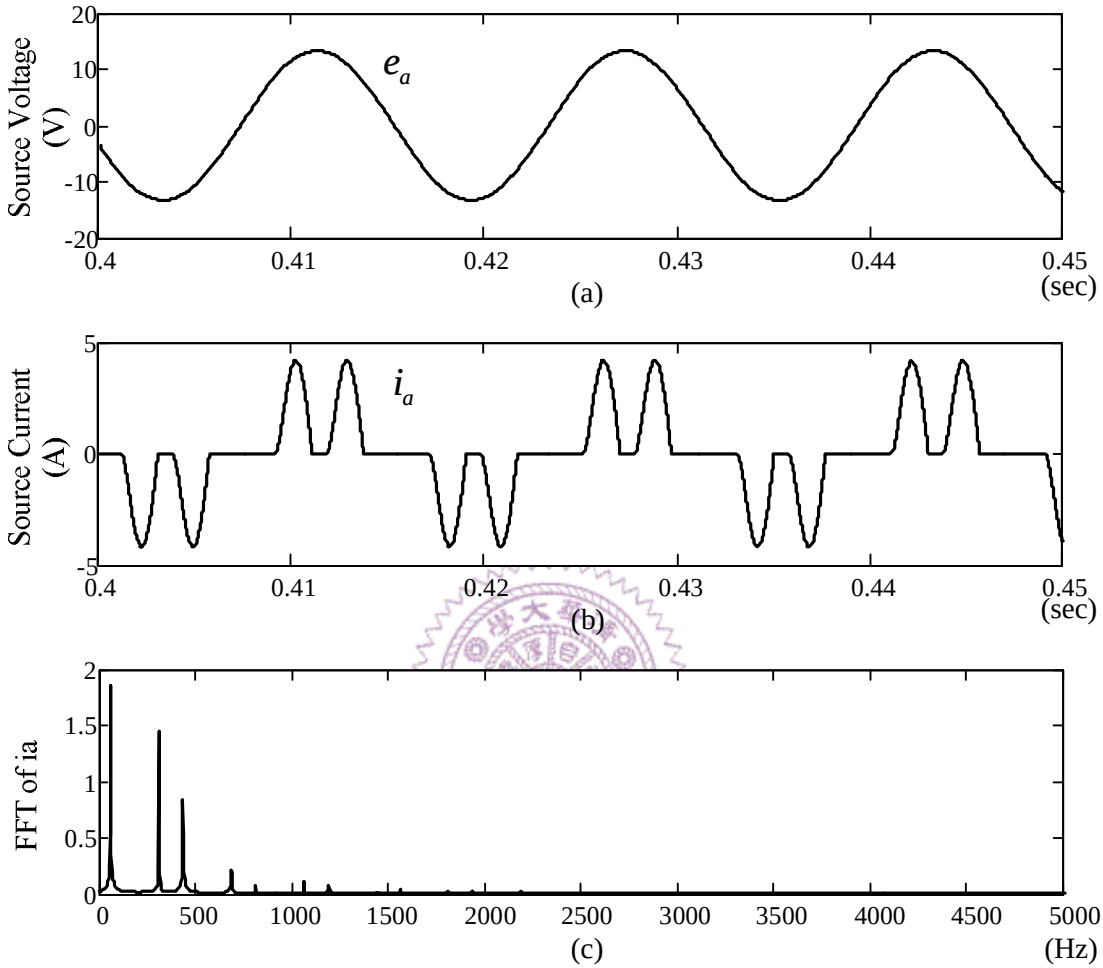

Fig. 4.11 Simulation results of the conventional two-stage converter. (a) Phase voltage, (b) input phase current and (c) FFT of the input phase current.

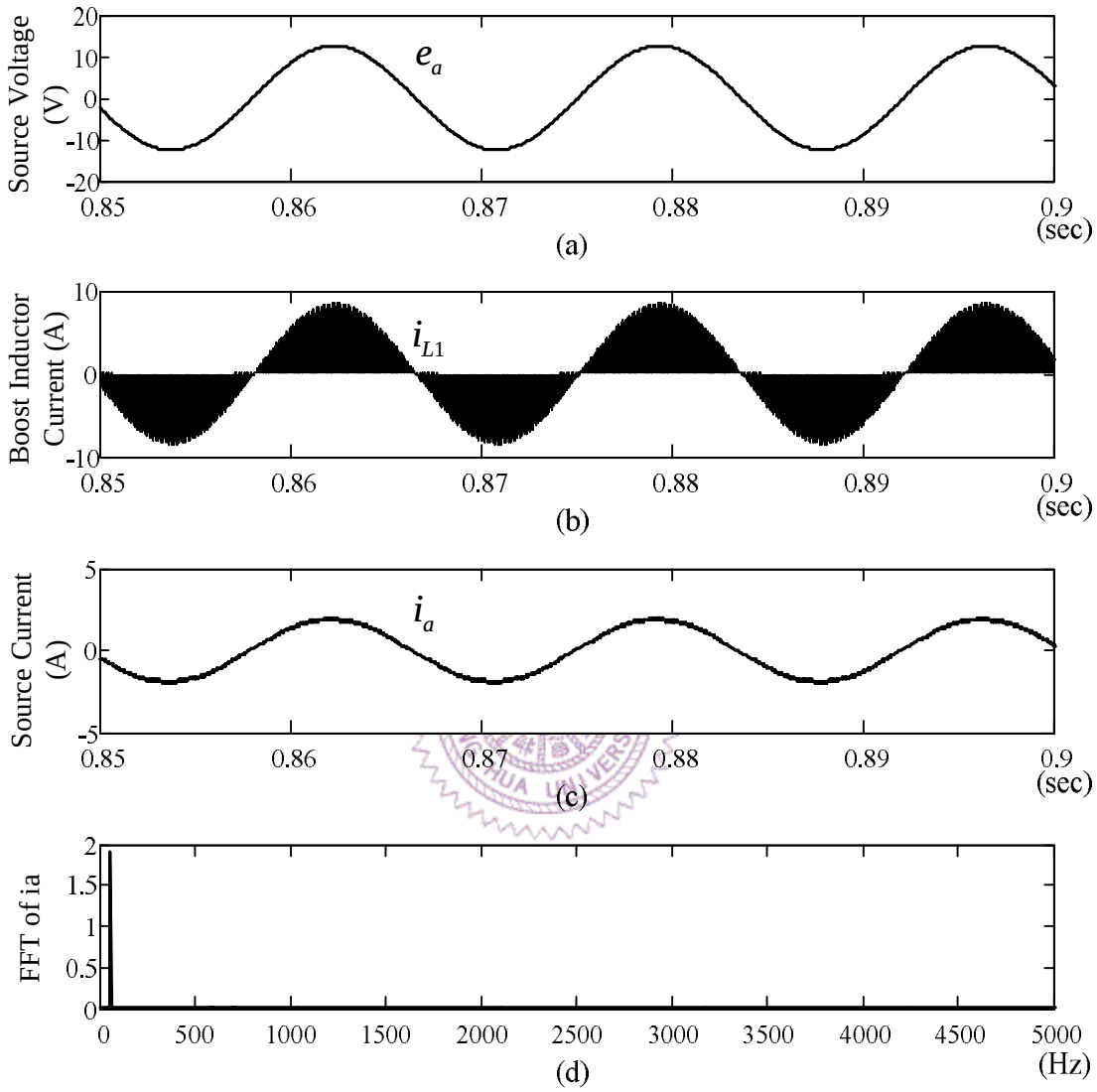

Fig. 4.12 Simulation results of the proposed converter with full DCM control. (a) Phase voltage, (b) boost inductor current, (c) source current and (d) FFT of source current.

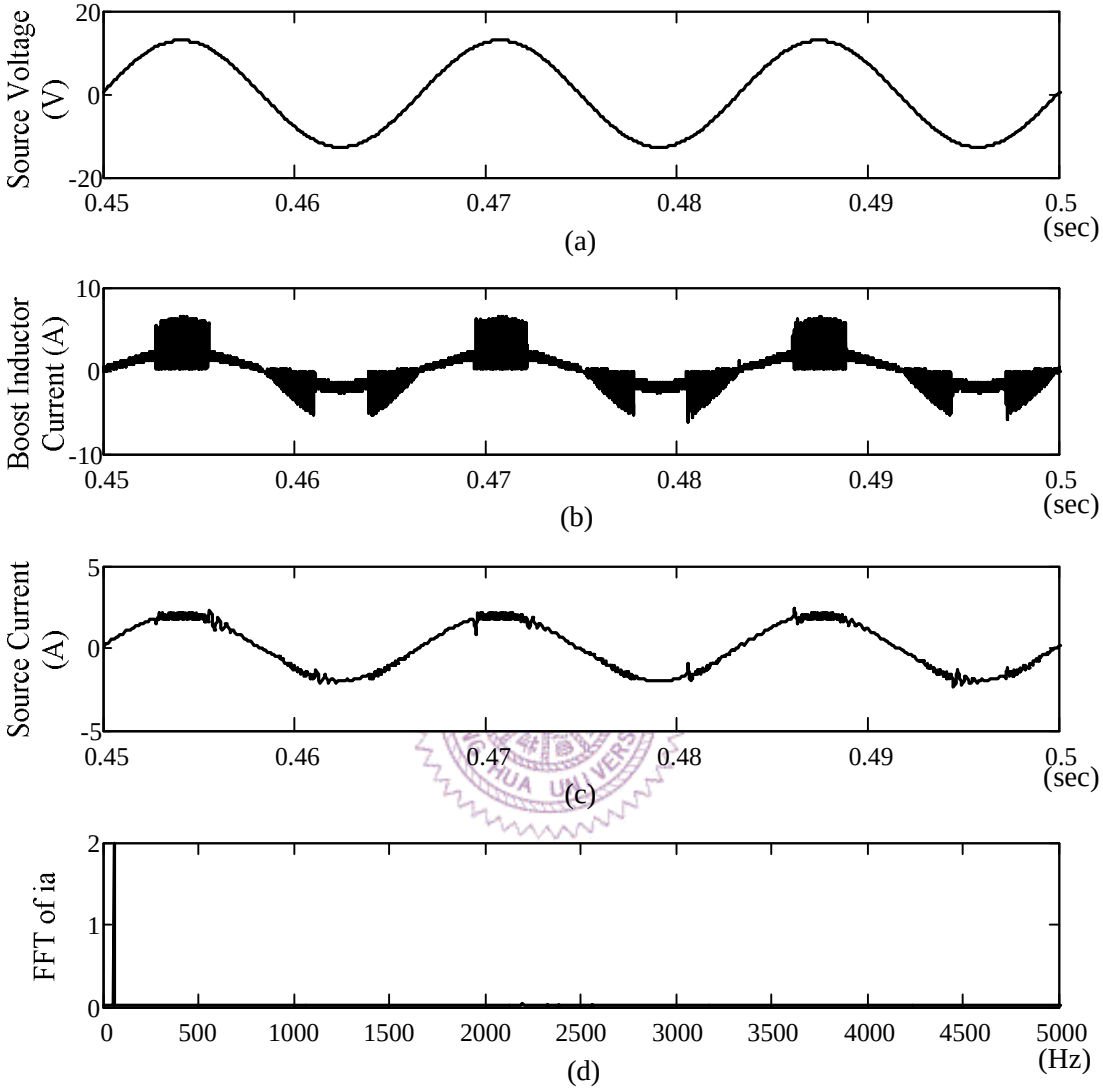

Fig 4.13 Simulation results of the proposed converter with hybrid control. (a) Phase voltage, (b) boost inductor current, (c) source current and (d) FFT of source current.

CHAPTER 5

IMPLEMENTATION AND EXPERIMENTAL RESLUTS

5.1 Introduction

From the previous chapters, it can be seen that the proposed dynamic MPPT controller with adjustable virtual inertia technique can effectively improve the dynamic response of the wind turbine and increase the amount of extracted wind power under wind speed variations. Moreover, to overcome the disadvantages of significant current THD and poor efficiency in the conventional two-stage ac to dc converter, a single-stage QSR converter is proposed.

To evaluate the performance of the whole system with the proposed dynamic MPPT controller and the single-stage QSR converter, a prototype system is implemented and a facility for testing the prototype is constructed as well. In this chapter, configuration of the testing facility is described in section 5.2. In the next section, the implementation of the prototype system is introduced in detail. Finally, some experimental results are given to verify the validity of the proposed system.

5.2 Description of the Testing Facility

Fig. 5.1 shows the configuration of the testing facility that is composed of a programmable centrifugal blower, a small vertical axial wind turbine, a measurement set and a power and control plane. To obtain the expression of the power coefficient which is usually not available from the manufacturer, a speed-controllable wind farm is required for testing the wind turbine. In the constructed facility, a centrifugal blower with a programmable driver is used to generate a speed-controllable wind farm. By setting the wind speed at different levels and then changing the loading of the

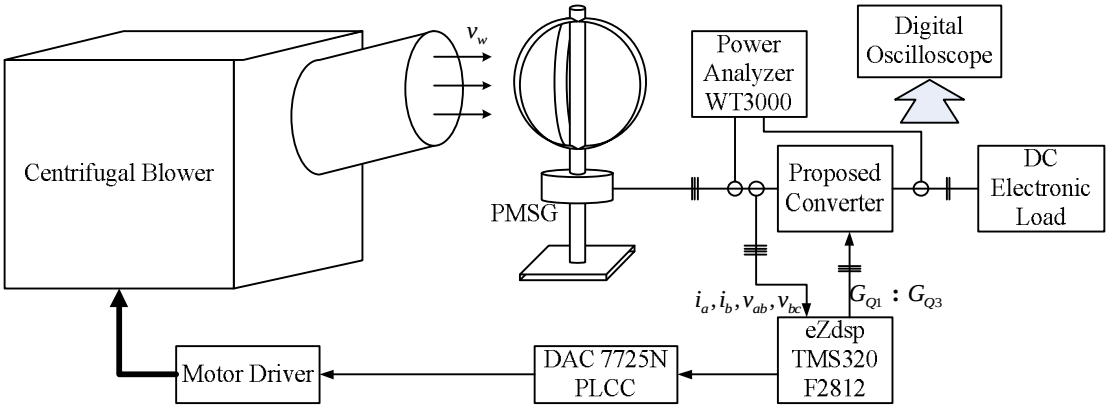

Fig. 5.1 Configuration of the facility for testing the small WPGS.

generator, one can measure the extracted wind power curve with respective to the rotating speed of wind turbine under various wind speeds. Then, the power coefficient of the wind turbine can be polynomial approximated according to the measured power curves.

The centrifugal blower consists of a centrifugal impeller, an induction motor and a programmable driver. The centrifugal impeller is driven by the induction motor which is controlled by the programmable driver. The high speed rotating impeller will change the airflow direction and accelerate the air stream. Part of the mechanical power of the impeller will be transferred into the air stream. In other words, the velocity of the wind output from the blower can be controlled by adjusting the rotating speed of the centrifugal impeller. In the constructed facility, a command signal is fed into the programmable driver for controlling the speed of the induction motor so that the rotating speed of the impeller can be adjusted accordingly.

The small vertical axial wind turbine, DS-200, used in the prototype system is manufactured by Hi-VAWT Technology Corporation. Fig. 5.2(a) shows the structure of the small wind turbine which is composed of Savonius type and Darrienus type blades as well as a coreless axial flux permanent magnet generator (AFPMG). The

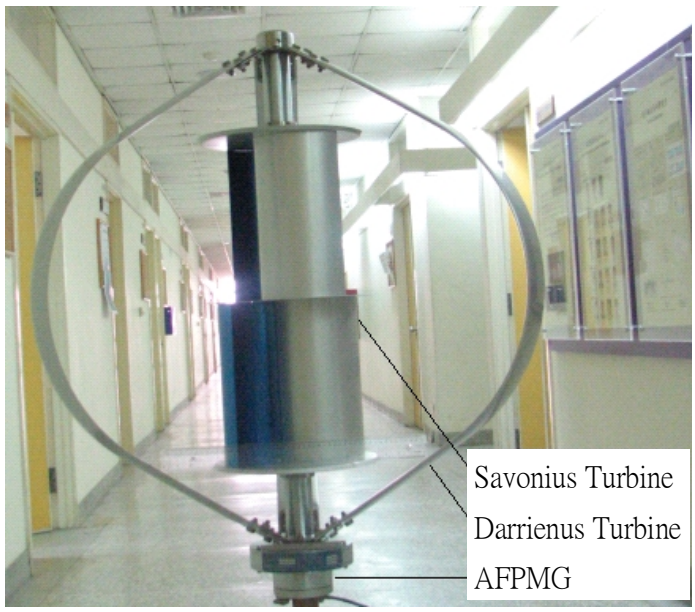

(a)

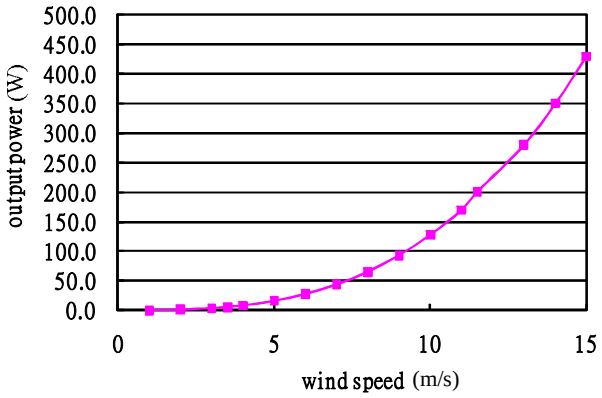

(b)

Fig. 5.2 (a) The small VAWT, DS200. (b) Output power curve of DS200.

maximum power curve with respect to the wind speed provided by the manufacturer is shown in Fig. 5.2(b). Due to the utilization of the coreless stator, the starting torque of the wind turbine is reduced which results in lower cut-in wind speed.

In order to measure and record the experimental data, a three-phase precision power analyzer, WT3000, and a digital oscilloscope are used as the measurement set

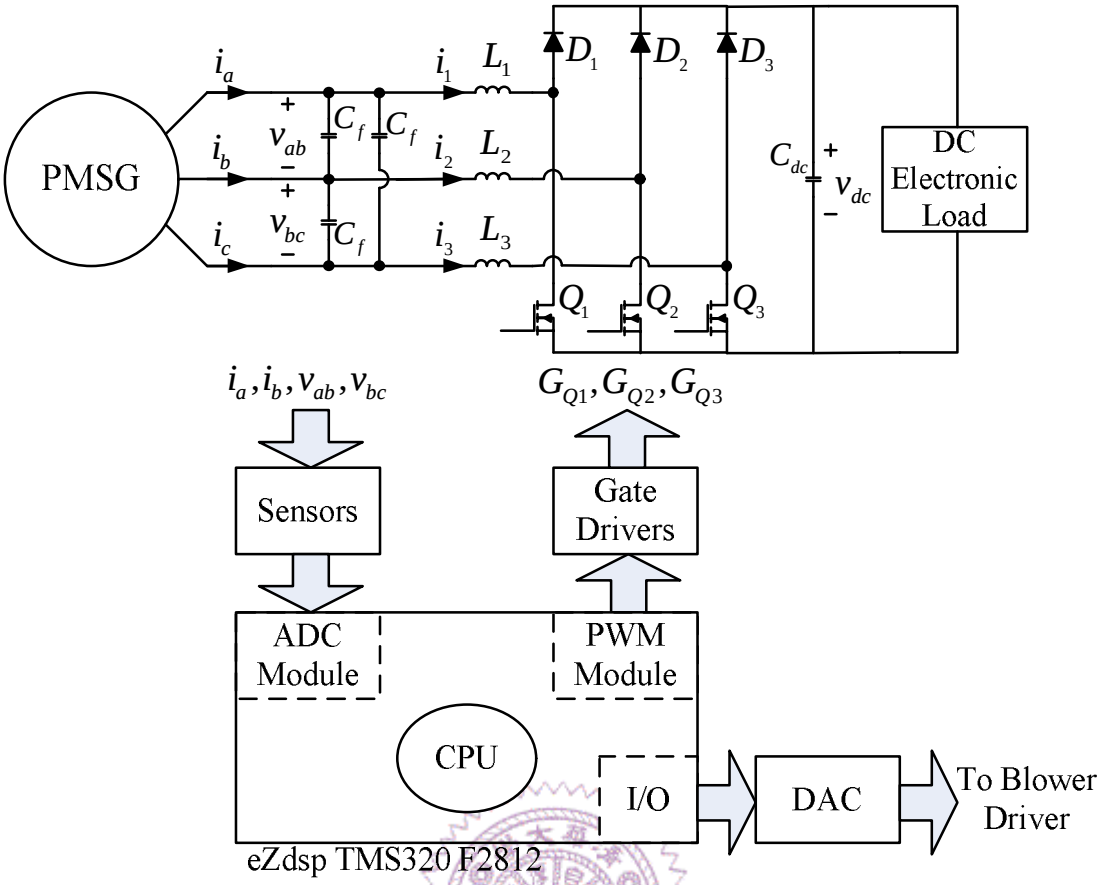

Fig. 5.3 Configuration of the power stage in the small WPGS.

in the testing facility. The precision power analyzer WT3000 is manufactured by Yokogawa Electric Corporation. The relative experimental data are first recorded in the memory or a flash peripheral, and then are analyzed by means of computing software Matlab on a personal computer.

Fig. 5.3 shows the configuration of the power and control plane which is composed of a three-phase ac to dc converter, a dc electric load and a control plane implemented with a eZdsp board, TMS320 F2812. For easy to implement the dc bus voltage regulation, the dc electronics load is operated at constant voltage mode to simulate the battery module and load demand. Both the proposed single-stage QSR converter and the conventional two-stage converter are implemented for comparing

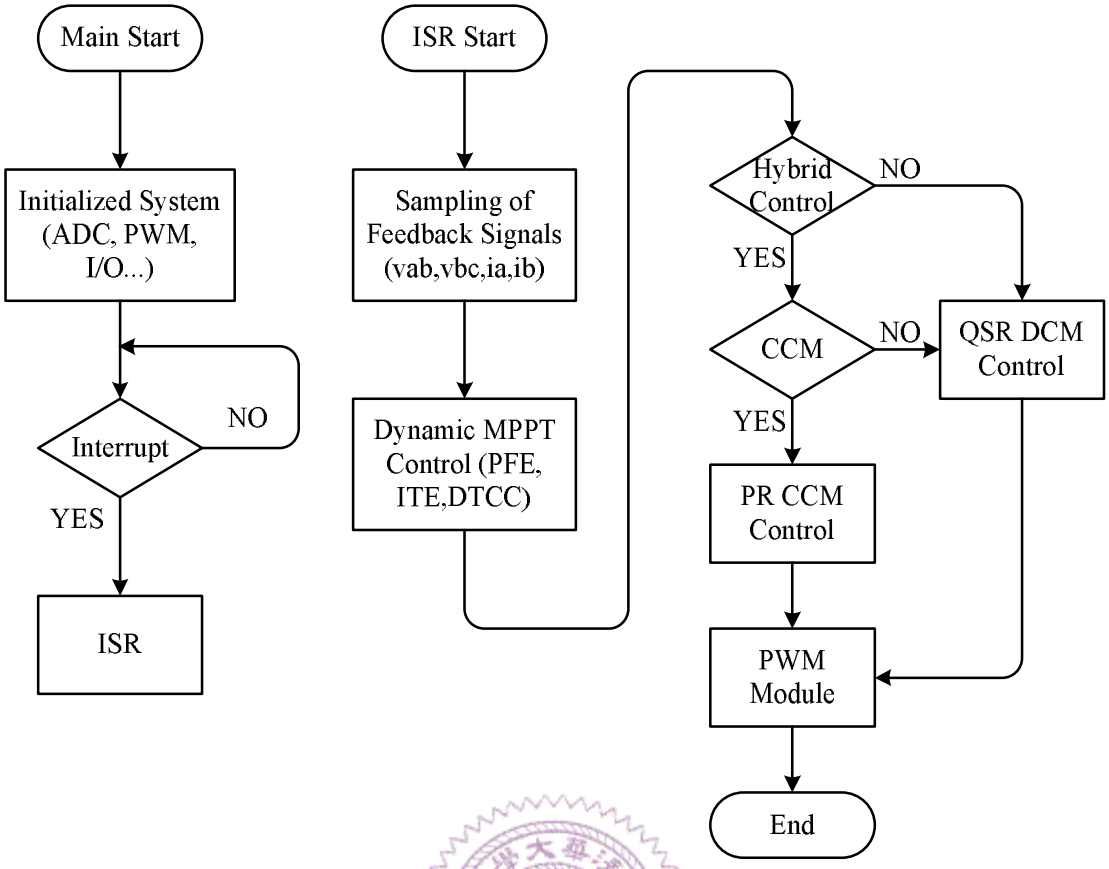

Fig. 5.4 The flowchart of the whole program of the proposed WPGS.

the performance. The implementation of the prototype is described in the next section in detail.

5.3 Implementation of the Proposed WPGS

The MOSFETs, IXFH 150N15P, and schottky diodes, DSSK60-02A, are adopted as the active switches and diodes for the converter. All the control algorithms, such as the dynamic MPPT controller, adjustable virtual inertia technique, QSR technique and hybrid control, are implemented with a digital signal processor, TMS320 F2812. The flowchart of the whole program is shown in Fig. 5.4. It can be seen from Fig. 5.4 that the program can be set as fully QSR DCM control or hybrid control depending on what is the major concern, performance or simpleness. The peripheral circuits are shown in Fig. 5.5 to Fig. 5.8. Fig. 5.5 shows two measurement circuits of the

generator line voltages v_{ab} and v_{bc} which are fed to the phase and frequency estimator to observe the information rotating speed of the wind turbine. Fig. 5.6 shows the measurement circuits of generator currents i_a and i_b. The current amplitude can then be calculated and fed back into the current control loop. Fig. 5.7 shows the circuit diagram of the digital to analog circuit which is constructed with a digital to analog converter (DAC) chip, DAC7725N PLCC. One major task of the DAC is to convert the digital wind speed command signal from the DSP into an analog signal for the programmable centrifugal blower. Also, the digital data in the DSP can be converted into analog signals for displaying on a oscilloscope as well. The digital wind speed command is calculated and output to the I/O port of the eZdsp TMS320F2812. Then, the DAC will output an analog signal to the programmable driver. The gate drive circuits are shown in Fig. 5.8. Because of the common source connection of the three active switches in the proposed converter, there is only one isolated power source required.

5.4 Experimental Results

Fig. 5.9 shows the photograph of the testing facility and the prototype WPGS. The parameters of the prototype system are given as follows:

Radius of the wind turbine	$r = 0.5\ m$
Rated Power	$P_{rated} = 200\ w$
Rated wind speed	$v_{w,rated} = 12.5\ m/s$
Maximum power coefficient	$C_{p,\max} = 0.282$
Optimal TSR	$d_{opt} = 3.53$
Generator side inductance	$L_s = 300\ uH$

Stator resistance	$R_s = 0.2\ \Omega$
Boost inductor	$L = 100\ uH$
Filter capacitor	$C_f = 14.7\ uF$
Mechanical inertia	$J = 0.4\ \ k_g \cdot m^2$
Friction coefficient	$B = 0.008$
Output DC voltage	$v_{dc} = 100\ V$

As mention in section 5.2, the power coefficient can be approximated with measured power curves. The polynomial approximated power coefficient of the wind turbine is given as follows.

$$C_p(d) = a_0 + a_1 d + a_2 d^2 + a_3 d^3 + a_4 d^4 \tag{5.1}$$

$$\begin{bmatrix} a_0 \\ a_1 \\ a_2 \\ a_3 \\ a_4 \end{bmatrix} = \begin{bmatrix} 3.27\times10^{-4} \\ -1.889\times10^{-2} \\ 6.1327\times10^{-2} \\ -4.614\times10^{-3} \\ -1.372\times10^{-3} \end{bmatrix}$$

First, to demonstrate the function of the proposed MPPT controller, the system is tested under changing wind speed situation and the corresponding experimental results are shown in Fig. 5.10. It is seen from Fig. 5.10(b) that as the wind speed steps up to a higher speed, the generator torque in the proposed system is instantly controlled to be smaller than that of the conventional system for achieving faster converging to the optimal operating point. On the contrary, as the wind speed steps down to a lower speed, the torque command will be instantly controlled to a larger magnitude for decelerating the wind turbine more rapidly to the optimal operating

point. Fig. 5.10(c) shows the corresponding power coefficients, which are calculated from the measured data with the approximate polynomial of the C_p function. It can be seen from Fig. 5.10(c) that as a result of the improved dynamic response, the regulation of the power coefficient of the wind turbine is greatly enhanced. Fig. 5.11 shows the corresponding loci of the generator torque with conventional OT control and proposed dynamic MPPT control respectively.

Next, to evaluate the performance of the proposed WPGS under wind speed variations, the wind speed pattern expressed in (3.43) is used as the command signal for the blower driver. According to (3.37), the bandwidth of the dynamic response of the conventional system is about 0.03 Hz. Therefore, the energy of the higher frequency wind speed variation term in (3.43) will not be fully extracted. However, the bandwidth of the proposed system can be extended to about 0.1Hz with adjustable virtual inertia technique. The rotor speed and the calculated power coefficient are shown in Fig. 5.12(a) and (b). It can be seen from Fig. 5.12(b) that due to the improved dynamic response the regulation of the power coefficient of the proposed WPGS is greatly improved. After an integration period of 500 seconds, under the wind speed variation as given in (53) the extracted wind energy of the proposed system and the conventional system are 4.570 Wh and 4.467 Wh respectively, which is increased about 2.3%. Hence, the proposed system can effectively extract more wind energy from the higher frequency wind speed variations.

The major disadvantage of the conventional two-stage converter is the significant THD of the generator current which is shown in Fig. 5.13(a) and (b). As a comparsion, the generator current of the proposed system with fully QSR DCM control is shown in Fig. 5.13(c) and the corresponding FFT of the generator current is shown in Fig. 5.13(d). The THD of the generator current is obviously greatly reduced in the

proposed system. Fig. 5.14 shows the current waveforms of the conventional WPGS and the proposed WPGS with hybrid control. Fig. 5.15 shows the current THD and efficiency of the conventional two-stage converter and the proposed converter with fully QSR DCM control as well as hybrid control under different power levels. From the experimental results, one can see that the proposed single stage rectifier with the proposed hybrid control is able to reduce the current THD to about 5% and increase the efficiency about 11%. Although the efficiency of the fully QSR DCM controlled converter is slightly poorer, the control algorithm of the QSR DCM control is simpler than that of the hybrid control. Hence, one can choose the most suitable control strategy according to the application demand.

In summary, compared with the conventional WPGS with steady state optimal torque MPPT control, the proposed WPGS can further increase the system efficiency from about 12% to 15% depending on the wind speed variations.

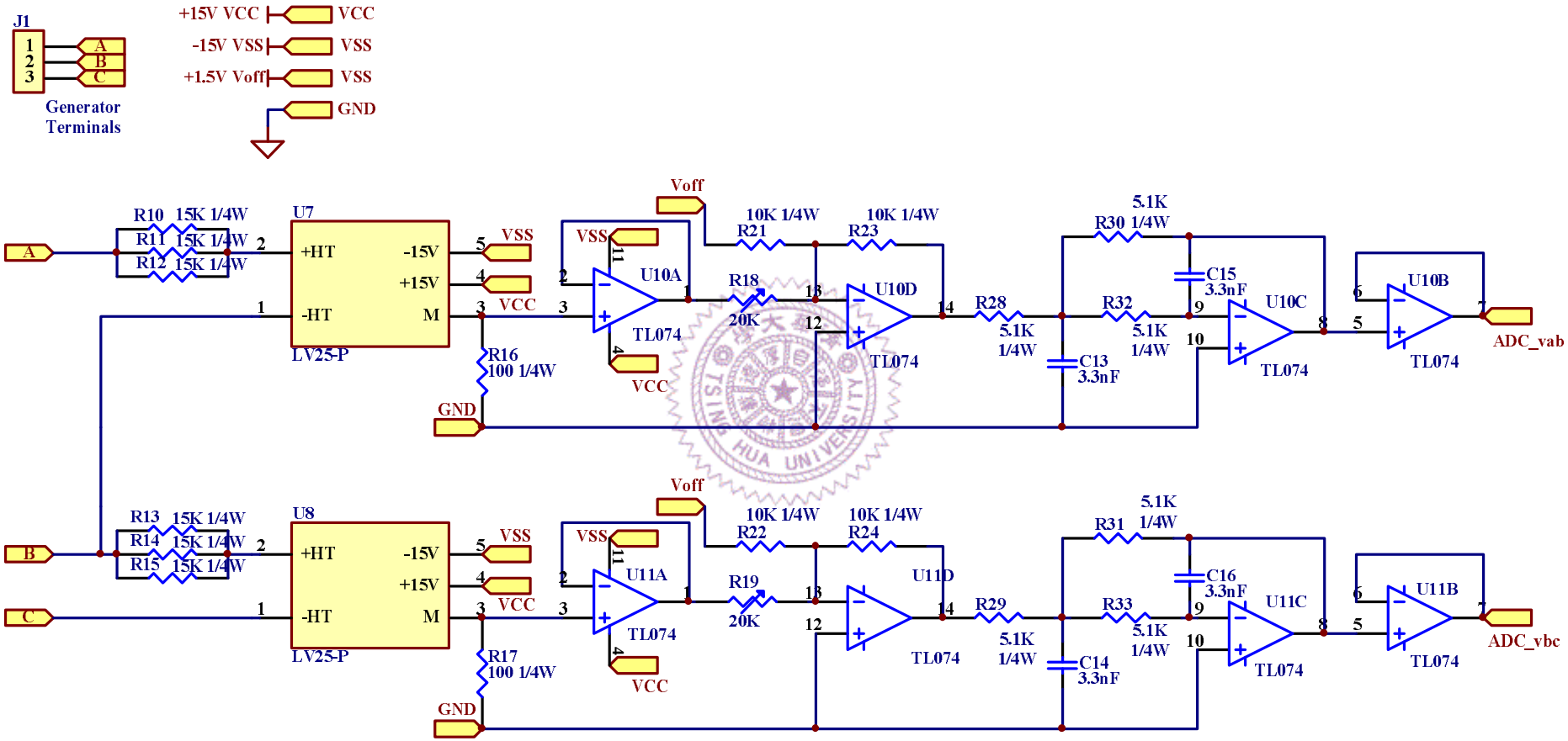

Fig. 5.5 The voltage sensor circuits for generator stator voltages v_{ab} and v_{bc}.

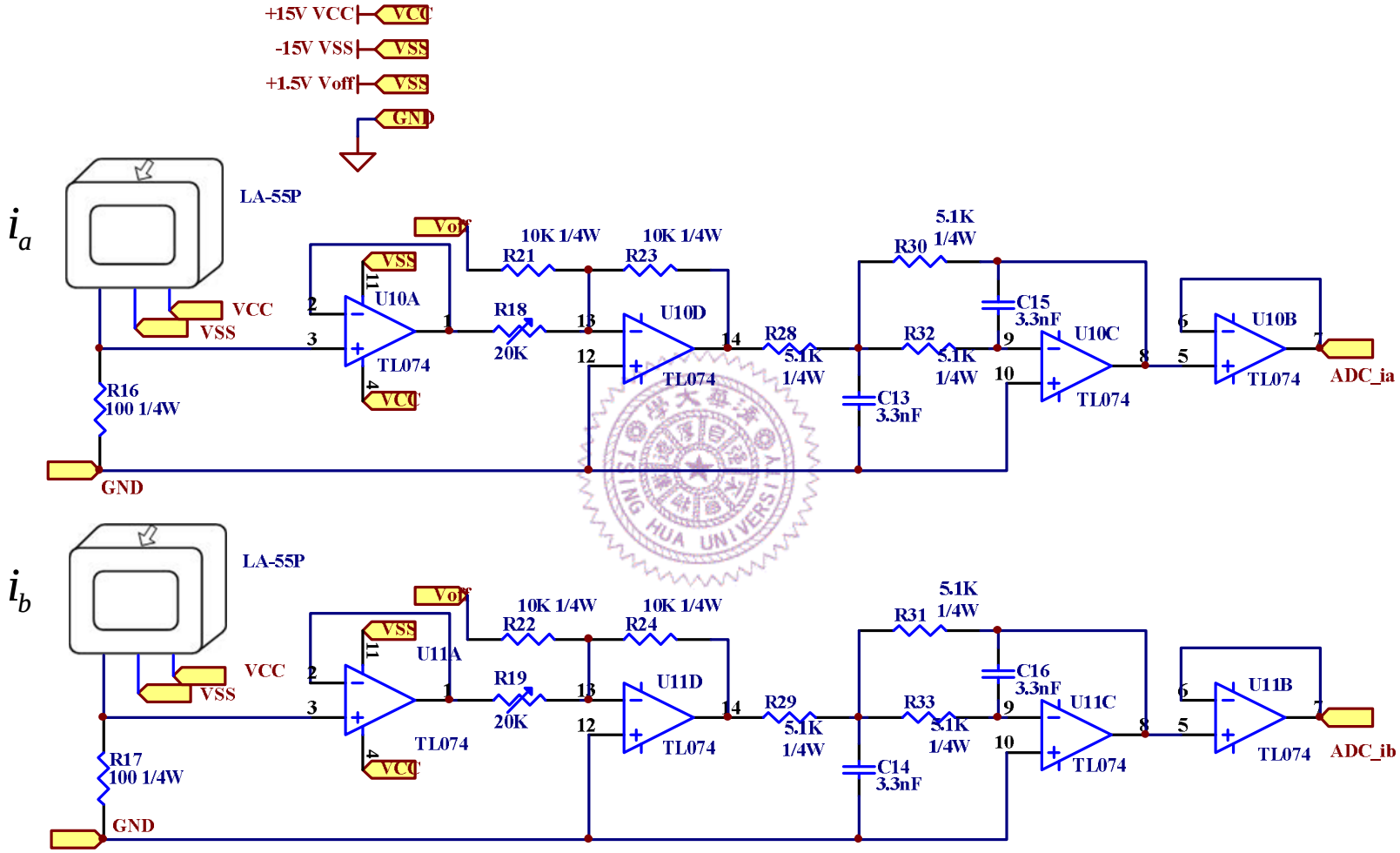

Fig. 5.6 Sensor circuits for generator currents i_a and i_b.

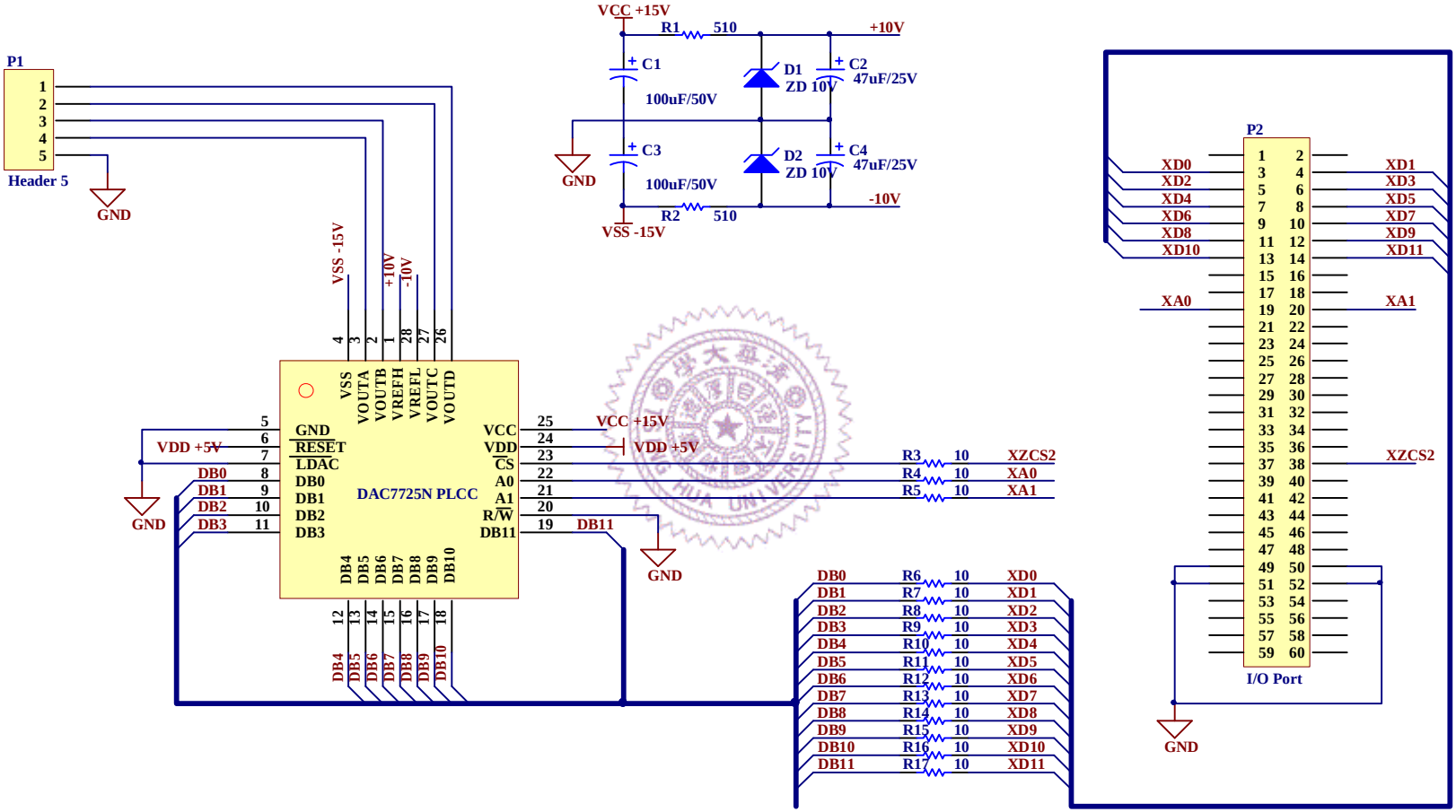

Fig. 5.7 Circuit diagram of the digital to analog circuit.

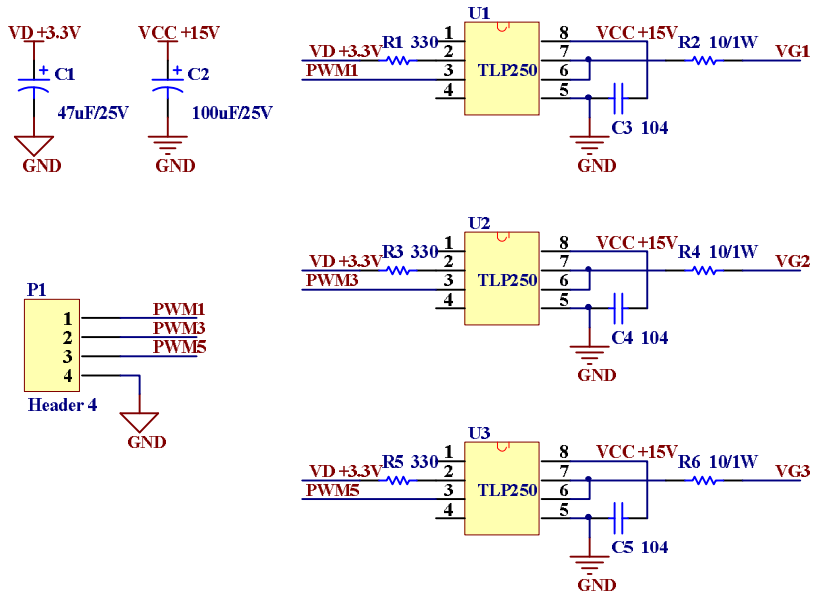

Fig. 5.8 Circuit diagram of isolated gate drives.

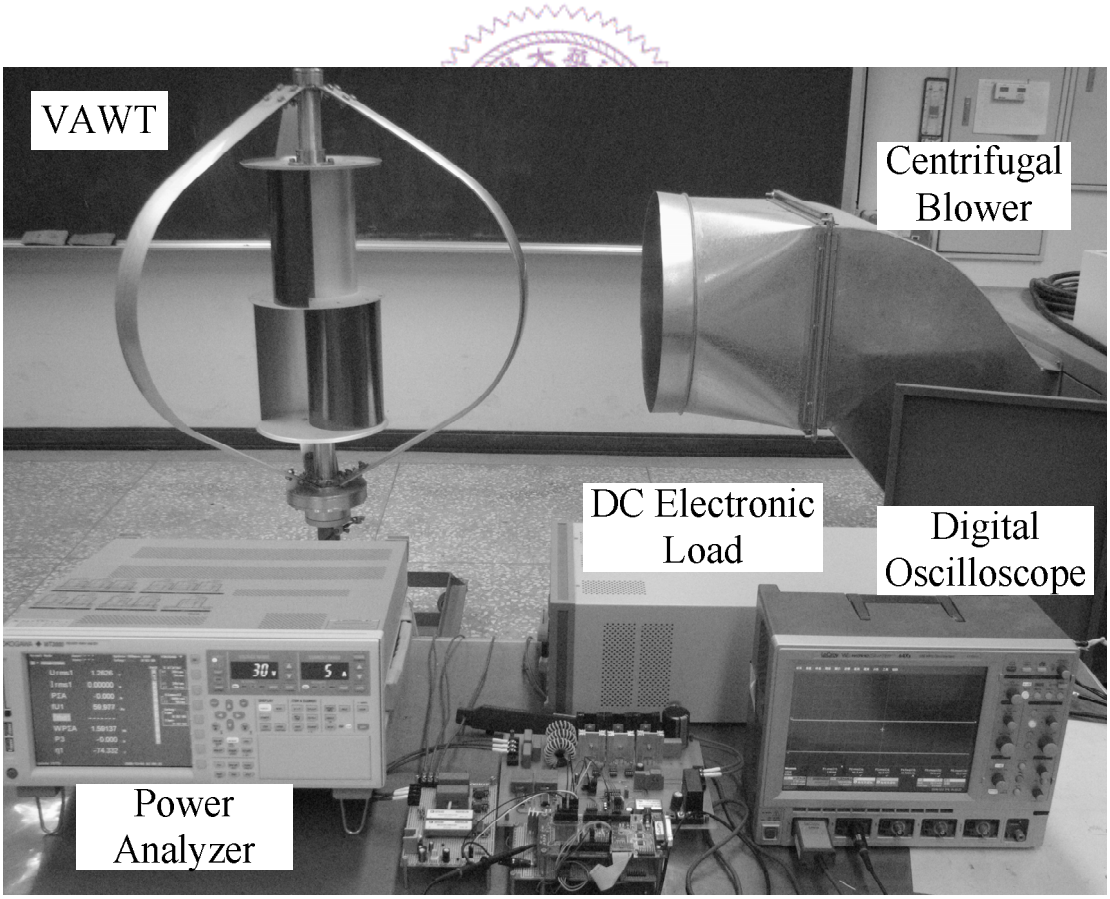

Fig. 5.9 Photograph of the testing facility.

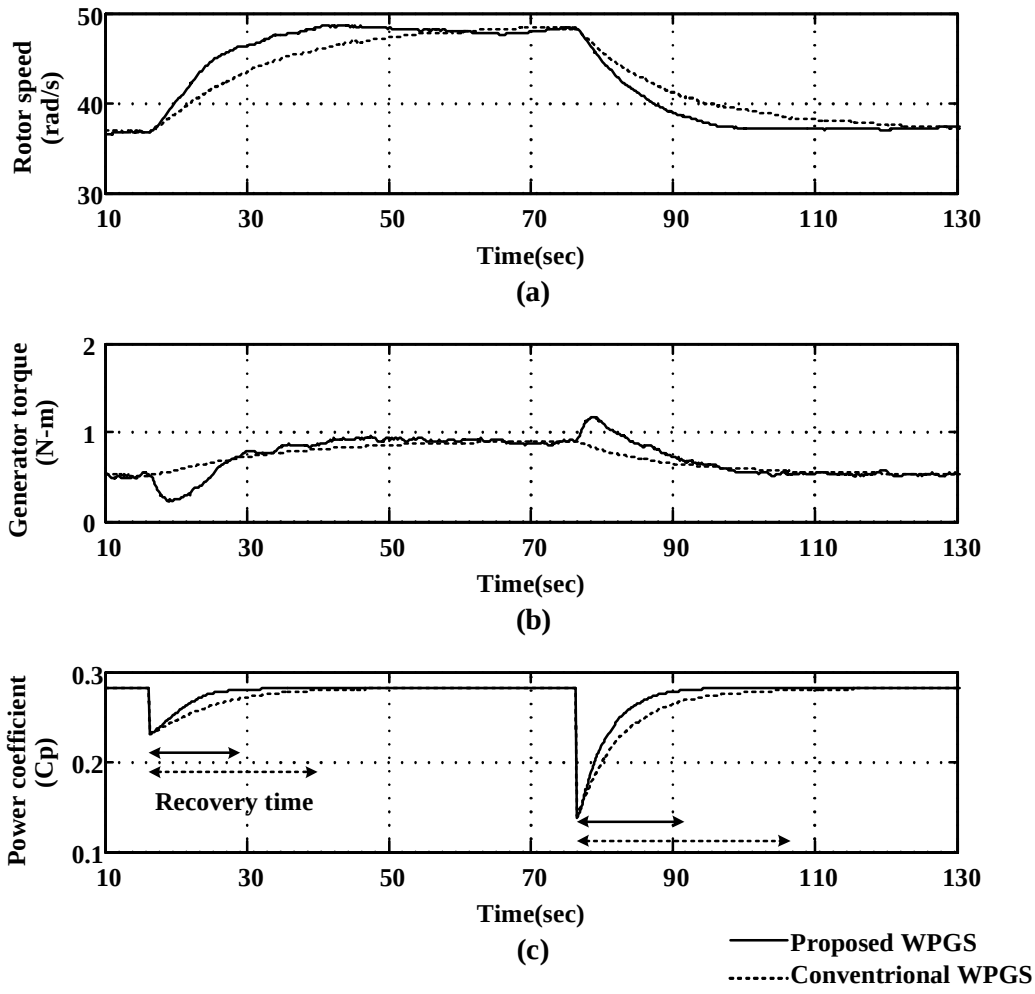

Fig. 5.10 Experimental results under pulse changing wind speed. (a) Rotor speed. (b) Generator torque. (c) Power coefficient.

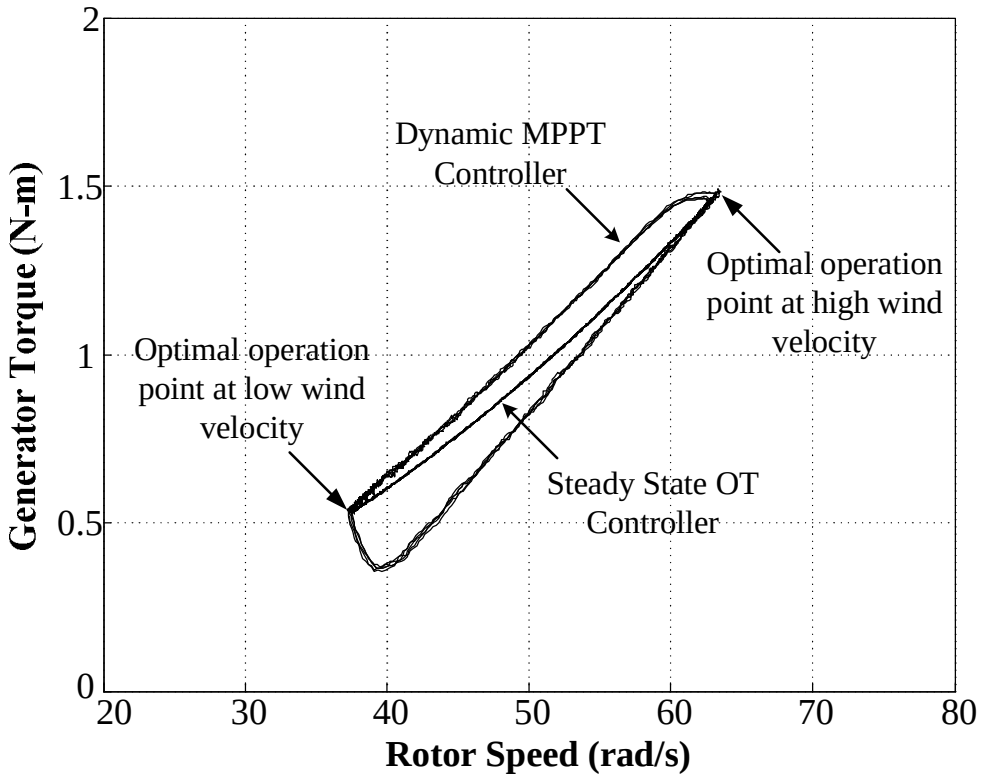

Fig. 5.11 The loci of the generator torque with conventional OT control and proposed dynamic MPPT control respectively.

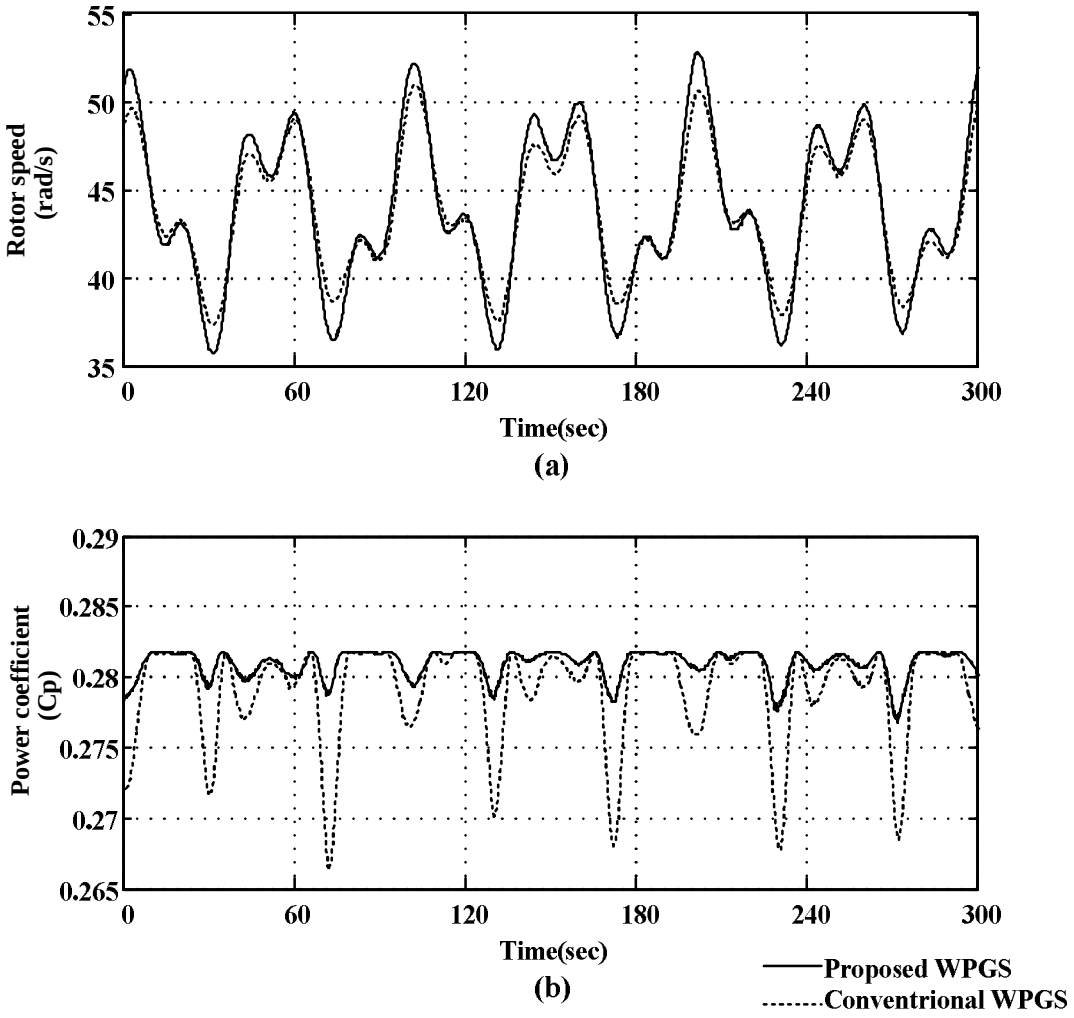

Fig. 5.12 Experimental results under continuously varying wind speed. (a) Rotor speed. (b) Power coefficient.

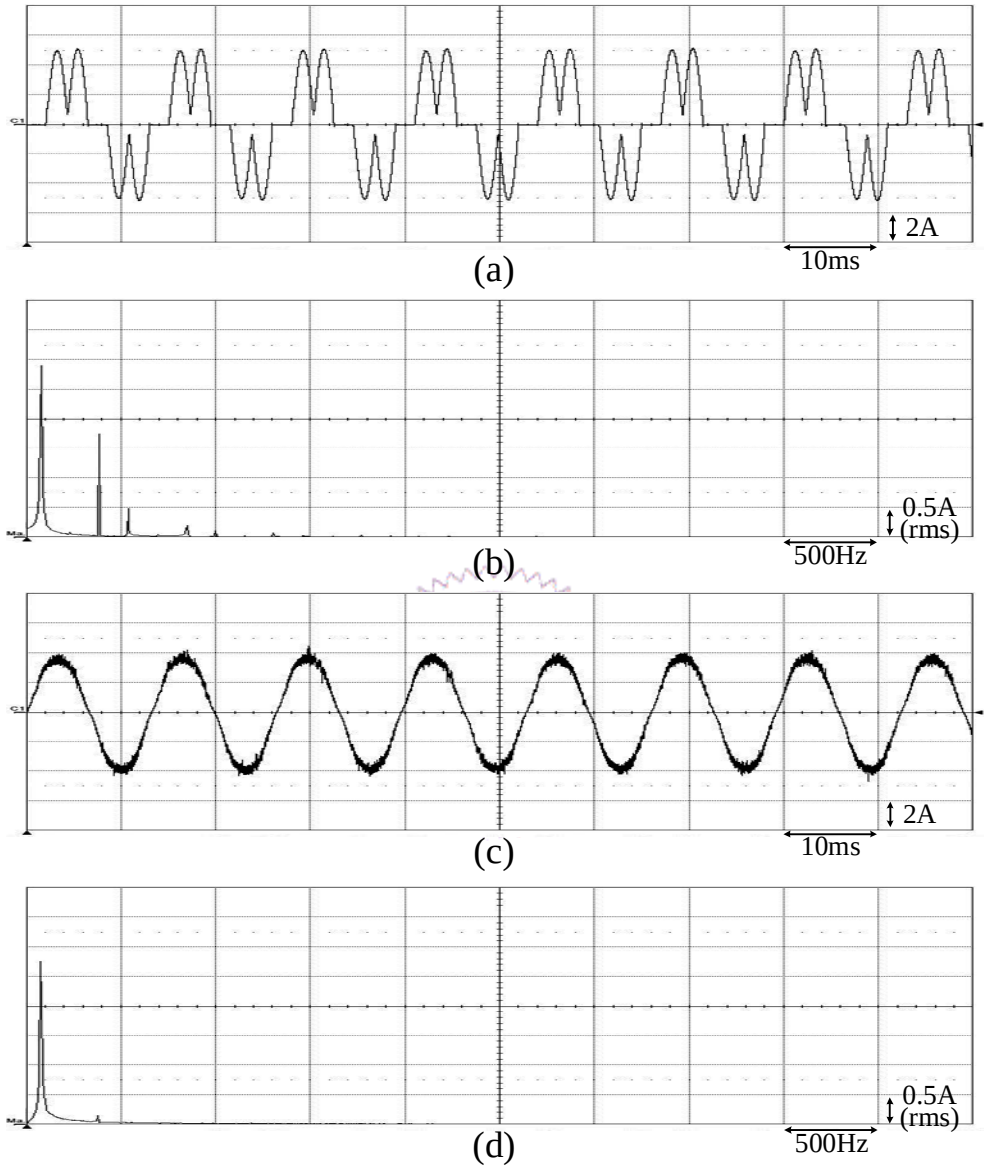

Fig. 5.13 Experimental results (10ms/div). (a) Generator current of the conventional system (2A/div). (b) FFT of the generator current (500Hz/div). (c) Generator current of the proposed system (2A/div). (d) FFT of the generator current in (c) (500Hz/div).

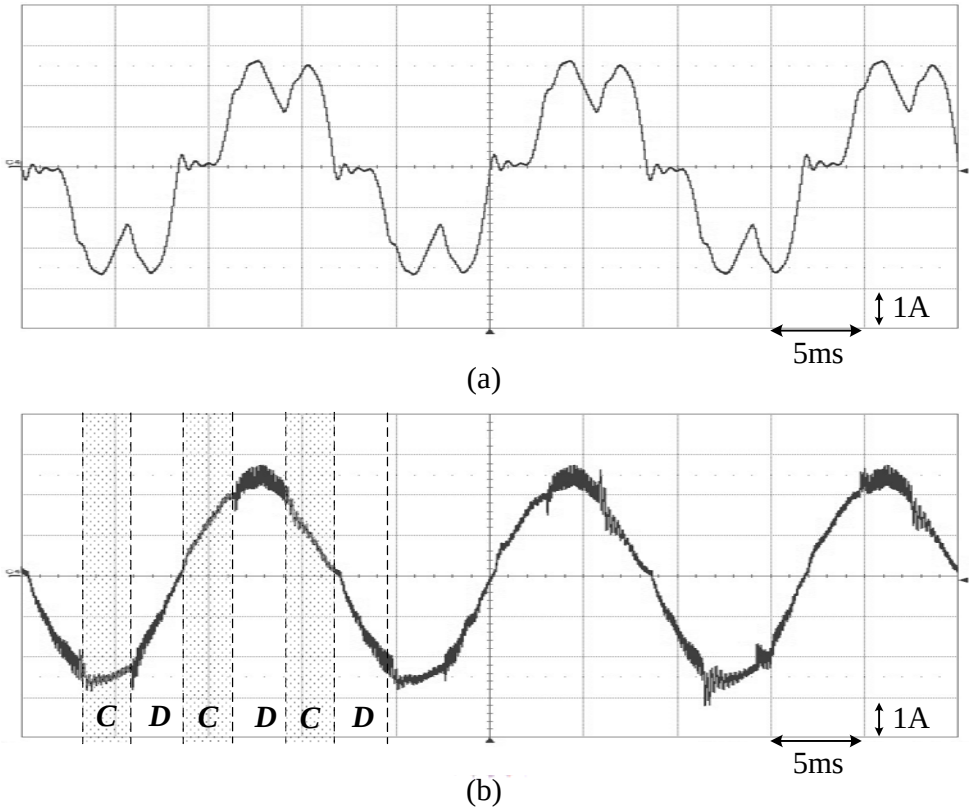

Fig. 5.14 The measured current waveforms of (a) the conventional WPGS and (b) the proposed WPGS (1A/div, 5ms/div). ***C***: CCM, ***D***: DCM.

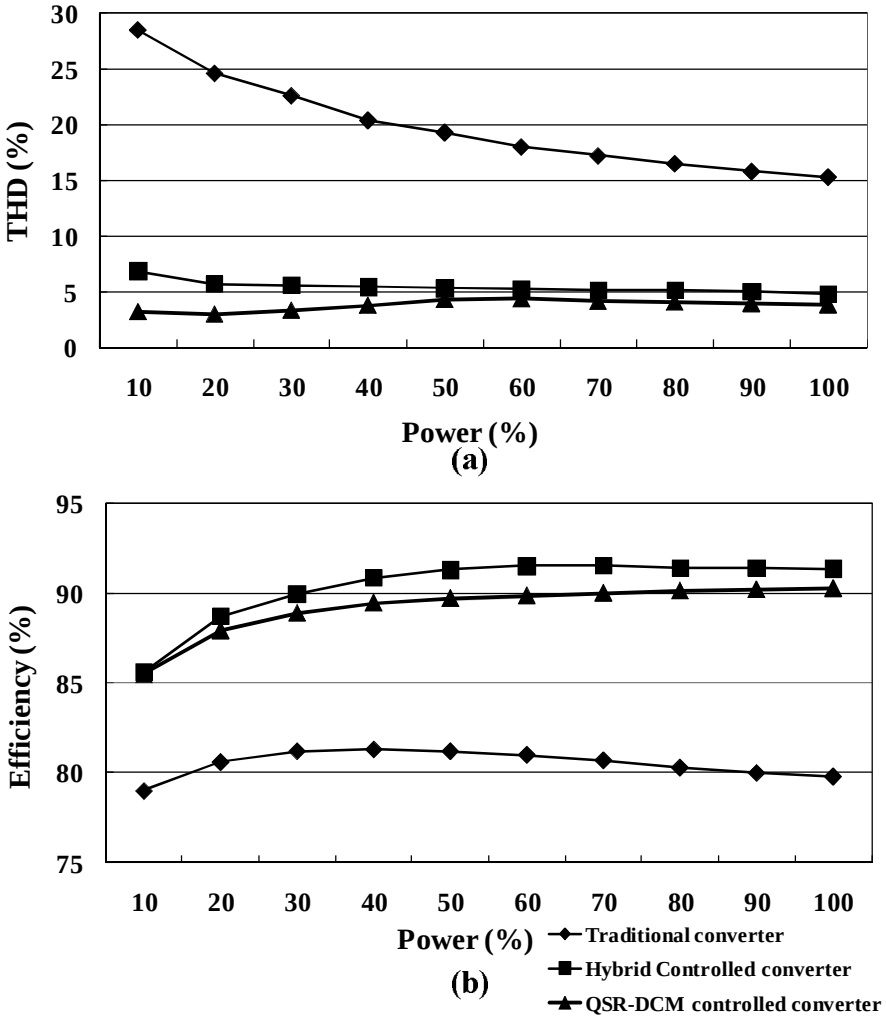

Fig. 5.15 The experimental data of the traditional two-stage converter, the single-stage converter with proposed QSR-DCM control and with proposed hybrid control. (a) The current THD and (b) the conversion efficiency.

CHAPTER 6

CONCLUSIONS

To the author's best knowledge, very few papers concern about the dynamic performance of the MPPT controller for a wind turbine. However, the poor dynamic response due to the mechanical inertia will cause reduction of the efficiency of the wind turbine under wind speed variations especially in low speed region. In this dissertation, a novel sensorless dynamic MPPT controller is proposed to deal with this problem. For cost and reliability considerations, there are no mechanical sensors such as anemometer and encoder used in the proposed controller. To improve the dynamic response, a dynamic optimal torque command calculator based on a novel adjustable virtual inertia technique is proposed. The regulation of the power coefficient of the wind turbine to the maximum value under wind speed variations is also improved because of the improved dynamic response. Also the amount of the extracted wind power can be increased greatly.

As to the three phase ac to dc converter in a small WPGS, due to the nonlinearity f the widely used two-stage ac to dc converter composed of a diode bridge rectifier and a dc converter, there will be significant current THD and power losses. The current THD will cause additional torque ripple, mechanical stress on the shaft and undesired acoustic noise. To overcome the above mentioned disadvantages, a single-stage ac to dc converter is proposed in this dissertation. A half-controlled topology composed of three active switches and three diodes is used to replace the existing two-stage topology for reducing the diode conduction loss and eliminating second time power conversion. When the converter is operated with DCM control, the generator current will be nearly sinusoidal and in phase with the EMF. To further reduce the conduction

losses caused by the body diodes, a novel quasi-synchronous rectification technique is proposed to extending the corresponding duty ratios of the switches in DCM operation. Also, the analytical expressions of the respective duty ratios are derived for easy implementation as well. Additionally, the CCM , DCM and QSR techniques are integrated into a novel hybrid control as an alternative control for the proposed single-stage converter. With the hybrid control algorithm, the efficiency of the converter can be further increased although the hybrid control is slightly more complicated.

To evaluate the validity and performance of the proposed MPPT controller and single-stage converter, a prototype wind power generation system is implemented. All the control algorithms, dynamic MPPT control, DCM control, QSR technique and hybrid control, are implemented with a digital signal processor TMS320 F2812. A facility for testing the WPGS is also constructed. In the facility, a programmable centrifugal blower is adopted to generate a speed-controllable wind farm. Some simulation and experimental results are given to demonstrate the performance of the proposed system. From the experimental results, one can see that not only the dynamic response of the wind turbine but also the efficiency of the whole system are greatly improved.

However, due to the limitation of time, there are still some possible objects worthy of further study which are listed as follows.

- Soft-switching technique can be applied to reduce the turn-off switching losses in DCM operation so that the converter efficiency can be further improved.
- An alternative approach to improve efficiency is to reduce the voltage stress of the active switches.
- The optimal power and torque curves will drift due to the variation of air

density. Therefore, robust control against to such variation should be applied.

- The robustness against to the uncertainties of inertia and friction coefficient should be improved.
- From the view point of whole system, coordinate control between the load demand, battery charging and MPPT of the wind turbine should be integrated.

REFERENCES

[1] AWEA. (2007, Jul.) "*AWEA Small Wind Turbine Global Market Study 2007,"* in the American Wind Energy Association Small Wind Systems [Online]. Available: http://www.awea.org/smallwind/

[2] AWEA. (2008, Jun.) "*AWEA Small Wind Turbine Global Market Study 2008,"* in the American Wind Energy Association Small Wind Systems [Online]. Available: http://www.awea.org/smallwind/

[3] A. M. Knight and G. E. Peters, "Simple wind energy controller for an expanded operation range," *IEEE Trans. Energy Convers.*, vol. 20, no. 2, Jun. 2005, pp. 459-466.

[4] S. Morimoto, H. Nakayama, M. Sanada, and Y. Takeda, "Sensorless output maximization control for variable-speed wind generation system using IPMSG," *IEEE Trans. Ind. Applicat.*, vol. 41, no. 1, Jan./Feb. 2005, pp. 60-67.

[5] K. Tan and S. Islam, "Optimum control strategies in energy conversion of PMSG wind turbine system without mechanical sensors," *IEEE Trans. Energy Convers.*, vol. 19, no. 2, Jun. 2004, pp. 392-399.

[6] F. Valenciaga and P. F. Puleston, "Supervisor control for a stand-alone hybrid generation system using wind and photovoltaic energy," *IEEE Trans. Energy Convers.*, vol. 20, no. 2, Jun. 2005, pp. 398-405.

[7] E. Koutroulis and K. Kalaitzakis, "Design of a maximum power tracking system for wind-energy-conversion applications," *IEEE Trans. Ind. Electron.*, vol. 53, no. 2, Apr. 2006, pp. 486-494.

[8] R. Datta and V. T, Ranganathan, "A method of tracking the peak power points for a variable speed wind energy conversion system," *IEEE Trans. Energy Convers.*,

vol. 18, no. 1, Mar. 2003, pp. 163-168.

[9] M. Stiebler, *Wind Energy Systems for Electric Power Generation*. London : Springer, 2008.

[10] P. Vas, *Vector Control of AC Machines*. New York: Oxford University Press, 1990.

[11] R. J. Wang, M. J. Kamper, K. V. der Westhuizen and J. F. Gieras, "Optimal design of a coreless stator axial flux permanent-magnet generator," *IEEE Trans. Magnetics*, vol. 41, no. 1, Jan. 2005, pp. 55-64.

[12] S. M. Hosseini, M. Agha-Mirsalim and M. Mirzaei, "Design, prototyping, and analysis of a low cost axial-flux coreless permanent-magnet generator," *IEEE Trans. Magnetics*, vol. 44, no. 1, Jan. 2008, pp. 75-80.

[13] R. J. Wang and M. J. Kamper, "Calculation of eddy current loss in axial field permanent magnet machine with coreless stator," *IEEE Trans. Energy Convers.*, vol. 19, no. 3, Sep. 2004, pp. 532-538.

[14] G. W. Carter, *Electromagnetic Field in Its Engineering Aspects*. London, U.K.: Longmans, 1954.

[15] N. Mohan, T. M. Undeland and W. P. Robbins, *Power Electronics: Converters, Applications, and Design (2nd edition)*. John Wiley, 1995.

[16] T. Emura and L. Wang, "A high-resolution interpolator for incremental encoders based on the quadrature PLL method," *IEEE Trans. Ind. Electron.*, vol. 47, no. 1, Feb. 2000, pp. 84-90.

[17] T. Emura, L. Wang, M. Yamanaka, and H. Nakamura, "A high-precision positioning servo controller based on phase/frequency detecting technique of two-phase-type PLL," *IEEE Trans. Ind. Electron.*, vol. 47, no. 6, Dec. 2000, pp. 1298-1306.

[18] G. F. Franklin, J. D. Powell, and A. Emami-Naeini, *Feedback Control of*

Dynamic Systems. New Jersey: Prentice Hall, 2002.

[19] P. Ioannou and J. Sun, *Robust Adaptive Control*. Prentice Hall, 1996.

[20] M. Karrari, W. Rosehart, and O. P. Malik, "Comprehensive control strategy for a variable speed cage machine wind generation unit," *IEEE Trans. Energy Convers.*, vol. 20, no. 2, Jun. 2005, pp. 415-423.

[21] Z. Lubosny, *Wind Turbine Operation in Electric Power Systems : Advance modeling*. Berlin Heidelberg: Spinger-Verlag, 2003.

[22] O. Garcia, J. A. Cobos, R. Prieto, P. Alou and J. Uceda, "Single phase power factor correction: a survey," *IEEE Trans. Power Electron.*, vol. 18, no. 3, May 2003, pp. 749-755.

[23] B. Singh, B. N. Singh, A. Chandra, K. Al-Haddad, A. Pandey and D. P. Kothari, "A review of single-phase improved power quality ac-dc converters," *IEEE Trans. Ind. Electron.*, vol. 50, no. 5, Oct. 2003, pp. 962-981.

[24] A. R. Prasad, P. D. Ziogas and S. Manias, "An active power factor correction technique for three-phase diode rectifier," *IEEE Trans. Power Electron.*, vol. 6, no. 1, Jan. 1991, pp.83-92.

[25] R. Teodorescu, F. Blaabjerg, M. Liserre, and P. C. Loh, "Proportional-resonant controllers and filters for grid-connected voltage-source converters," *IEE Proc.-Electr. Power Appl.*, vol. 153, no. 5, Sept. 2006, pp.750-762.

[26] J. Hu, Y. He, L. Xu, and B. W. Williams, "Improved Control of DFIG Systems During Network Unbalance Using PI-R Current Regulators," *IEEE Trans. Ind. Electron.*, vol. 56, no. 2, Feb. 2009, pp. 439-451.

[27] A. E. Feijoo, J. Cidras, and J. L. G. Dornelas, "Wind speed simulation in wind farms for steady-state security assessment of electrical power systems," IEEE Trans. Energy Convers., vol. 14, no. 4, pp. 1582–1588, Dec. 1999.

[28] G. Hua and Y. Geng, "A novel control strategy of MPPT taking dynamics of wind

turbine into account," in Proc. IEEE PESC '06, Jeju, Korea, Jun. 18-22, 2006, pp. 1-6.

[29] M. Chinchilla, S. Arnaltes, and J. C. Burgos, " Control of permanent-magnet generators applied to variable-speed wind-energy systems connected to the grid," *IEEE Trans. Energy Convers.*, vol. 21, no. 1, Mar. 2006, pp. 130-135.

[30] J. A. Baroudi, V. Dinavahi, and A. M. Knight, " A review of power converter topologies for wind generators," in *IEEE International Conference on Electric Machines and Drives*, May 15-18, 2005 ,pp. 458-465.

[31] F. S. Dos Reis, S. Islam, K. Tan, J. V. Alé, F. D. Adegas, and R. Tonkoski Jr, "Harmonic mitigation in wind turbine energy conversion systems," in *Proc. IEEE PESC '06*, Jeju, Korea, Jun. 18-22, 2006, pp. 2748-2754.

[32] F. J. Lin and Y. S. Lin, " A robust PM synchronous motor drive with adaptive uncertainty observer," *IEEE Trans. Energy Convers.*, vol. 14, no. 4, Dec. 1999, pp. 989-995.

[33] AWEA. (2002, Jun.) "*The U.S. Small Wind Turbine Industry Roadmap: A 20-years industry plan for small wind turbine technology*," in the American Wind Energy Association Small Wind Systems [Online]. Available: http://www.awea.org/smallwind/

[34] A. Mirecki, X. Roboam, and F. Richardeau, "Architecture complexity and energy efficiency of small wind turbines," *IEEE Trans. Ind. Electron.*, vol. 54, no. 1, Feb. 2007, pp. 660-670.

[35] B. Beltran, T. Ahmed-Ali, and M. E. H. Benbouzid, "Sliding mode power control of variable-speed wind energy conversion systems," *IEEE Trans. Energy Convers.*, vol.23, no. 2, Jun. 2008, pp.551-558.

[36] S. K. Chung, J. H. Lee, J. S. Ko, and M. J. Youn, "Robust speed control of brushless direct-drive motor using integral variable structure control," in *IEE*

Proc. Electr. Power Appl., vol. 142, no. 6. Nov. 1995, pp. 361-370.

[37] M. Malinowski, S. Stynski, W. Kolomyjski, and M. P. Kazmierkowski, "Control of Three-Level PWM Converter Applied to Variable-Speed-Type Turbines," *IEEE Trans. Ind. Electron.*, vol. 56, no. 1, Jan. 2009, pp. 69-77.

[38] J. Kikuchi, M. D. Manjrekar, and T. A. Lipo, "Performance Improvement of Half Controlled Three Phase PWM Boost Rectifier," in *Proc. 30th Annu. IEEE Power Electron. Spec. Conf.*, 1999, pp. 319-324.

[39] R. Cárdenas, R. Peña, P. Wheeler, J. Clare, and G. Asher, "Control of the Reactive Power Supplied by a WECS Based on an Induction Generator Fed by a Matrix Converter," *IEEE Trans. Ind. Electron.*, vol. 56, no. 2, Feb. 2009, pp. 429-438.

[40] J. J. Lee, J. M. Kwon, E. H. Kim, W. Y. Choi, and B. H. Kwon, "Single-Stage Single-Switch PFC Flyback Converter Using a Synchronous Rectifier," *IEEE Trans. Ind. Electron.*, vol. 55, no. 3, Mar. 2008, pp. 1352-1365.

[41] C. T. Pan and Y. H. Liao, "Modeling and Control of Circulating Currents for Parallel Three-Phase Boost Rectifiers," *IEEE Trans. Ind. Electron.*, vol. 55, no. 7, Jul. 2008, pp. 2776-2785.

[42] P. Bajec, B. Pevec, D. Voncina, D. Miljavec, and J. Nastran, "Extending the Low-Speed Operation Range of PM Generator in Automotive Applications Using Novel AC-DC Converter Control," *IEEE Trans. Ind. Electron.*, vol. 52, no. 2, Apr. 2005, pp. 436-443.

APPENDIX A DSP PROGRAM CODE

```
#include "DSP281x_Device.h"
#include "DSP281x_Examples.h"
#include "DSP281x_SinTable2048.h"

far int *DA_Porta;
far int *DA_Portb;
far int *DA_Portc;
far int *DA_Portd;

int16 Tcount1=0,Tcount2=0,temp4=0,step=0,sinwt_b=0,sinwt_c=0,iam=0,ibm=0;
int16 icm=0,id[2]={0,0},iq[2]={0,0};
int32 Uth=0,xo_p=0,yo_p=0,xo=0,yo=0,thida_err=0,sin_p=0,cos_p=0,sinwt=0,;
int32 coswt=0,m1=0,m2=0,m3=0,M2count=0,N=0,M=0,Nt=0, A1=15315;
int32 B1=4639,C1=4958,A2=3106,B2=29662,A3=1437,B3=13726,C3=22402;
int32 thida_a=0,thida_b=0,thida_c=0,Ie=0,Uv=0,pv=0,pi=0,d1=0,dQ1=0,dQ2=0;
int32 dQ3=0,Pin=0, temp3=0,step_count=0,Fe=0,count2=0,count3=0,temp1=0;
int32 temp2=0,duty_op=750, qv[2]={0,0},qi[2]={0,0},wm=0,wmsum=0,Im=0;
int32 KIm=291,Idc1=0,Idc2=0,Idc3=0,Itest=0,Idcsum=0,Idcavg=0,Pdc[2]={0,0};
int32 Kp_th=128,Ki_th=12800,pth=0,qth[2]={0,0},Kp_rpm=-28672,Ki_rpm=-10240;
int32 qrpm[2]={0,0},prpm=0, Kp_vo=300,Ki_vo=12000,Kp_vdc=-90,;
int32 Ki_vdc=-1800,Kp_i=350,Ki_i=70000,d1max=5000,vw=0,T1=30,f1p=0;
int32 T2=60,f2p=0,Rcounta=0,Sumiae=0,Avgiae[2]={0,0},ya[3]={0,0,0};
int32 Kp_c=-160,Ki_c=0,Ui=0,Ua=0,Ub=0,Uc=0,iaf[2]={0,0},ibf[2]={0,0};
int32 qa[2]={0,0},qb[2]={0,0},qc[2]={0,0},Kr=0,a0=6987,b1s=17522,b2s=12254;
int32 yb[3]={0,0,0},yc[3]={0,0,0},vabf[2]={0,0},vbcf[2]={0,0},iaf2[3]={0,0,0};
int32 Sumibe=0,Sumice=0,Avgibe[2]={0,0},Avgice[2]={0,0},Rcountb=0,Rcountc=0;
int32 ibf2[3]={0,0,0},vabf2[3]={0,0,0},vbcf2[3]={0,0,0};
int32 ia=0,ib=0,ic=0,ialfa=0,ibeta=0,vab[2]={0,0},vbc[2]={0,0},valfa=0,vbeta=0;
int32 stepf[2]={0,0},icf2[3]={0,0,0},iae[2]={0,0},ibe[2]={0,0},ice[2]={0,0};
int32 iaef2[3]={0,0,0},Imf2[3]={0,0,0},section=0,ma=0,mb=0,mc=0;
int32 ea=0,eb=0,ec=0,Ra=0,Rb=0,Rc=0,Dm=372,Da=0,Db=0,Dc=0,sin_da=0,;
int32 thida_Dm=0,thida_Da=0,thida_Db,thida_Dc=0,Imc=10240,sin_db=0,sin_dc=0;

interrupt void mppt(void);
void init_eva_timer1(void);
```

```
void CCM(void);
void DCM(void);
void Roffa(void);
void Roffb(void);
void Roffc(void);

void main(void)
{
    InitSysCtrl();
    InitGpio();
    DINT;
    InitPieCtrl();
    IER = 0x0000;
    IFR = 0x0000;
    InitPieVectTable();
    EALLOW;    // This is needed to write to EALLOW protected registers
    PieVectTable.T1UFINT = &mppt;
    EDIS;      // This is needed to disable write to EALLOW protected registers
    init_eva_timer1();
    InitAdc();

    DA_Porta=(far int *)0x080040;
    DA_Portb=(far int *)0x080041;
    DA_Portc=(far int *)0x080042;
    DA_Portd=(far int *)0x080043;

    AdcRegs.ADCTRL1.bit.CPS=0;
    AdcRegs.ADCTRL1.bit.ACQ_PS=0x8;
    AdcRegs.ADCTRL3.bit.ADCCLKPS=0x3;
    AdcRegs.ADCMAXCONV.all = 0x0003;            // Setup 3 conv's on SEQ1
    AdcRegs.ADCCHSELSEQ1.bit.CONV00 = 0x0;
    AdcRegs.ADCCHSELSEQ1.bit.CONV01 = 0x1;
    AdcRegs.ADCCHSELSEQ1.bit.CONV02 = 0x2;
    AdcRegs.ADCCHSELSEQ1.bit.CONV03 = 0x3;

     PieCtrlRegs.PIEIER2.all = (M_INT6);
     IER |= (M_INT2);
     EINT;      // Enable Global interrupt INTM
```

```
    ERTM;    // Enable Global realtime interrupt DBGM

    for(;;);
}

interrupt void mppt(void)
{
    DINT;
    IER=0x0000;
    IFR=0x0000;

//State Variable Sensoring
    AdcRegs.ADCTRL2.bit.RST_SEQ1 = 1; //reset SEQ1 to state CONV00
    AdcRegs.ADCTRL2.bit.SOC_SEQ1 = 1;
    while(AdcRegs.ADCST.bit.SEQ1_BSY==1);// wait for end of adc
    ia=(int32)(AdcRegs.ADCRESULT0>>4)-24-2048;   // Q11 15 A
    ib=(int32)(AdcRegs.ADCRESULT1>>4)-5-2048;
    vab[0]=(int32)(AdcRegs.ADCRESULT2>>4)-70-2048; //Q11 45V
    vbc[0]=(int32)(AdcRegs.ADCRESULT3>>4)-68-2048;

//per unit for current
    ia=ia*30;    //Q12 for 1 A
      ib=ib*30;
    ic=(int32)(0-ia-ib);

    vab[0]=(int32)vab[0]*15;    //Q11 for 3V
      vbc[0]=(int32)vbc[0]*15;

//Current and voltage LPF
    iaf2[0]=(C1*(((A1*ia+B1*iaf2[1])>>15)+2*ia+5*iaf2[1]-iaf2[2]))>>15;
    iaf2[2]=iaf2[1];
    iaf2[1]=iaf2[0];

    ibf2[0]=(C1*(((A1*ib+B1*ibf2[1])>>15)+2*ib+5*ibf2[1]-ibf2[2]))>>15;
    ibf2[2]=ibf2[1];
    ibf2[1]=ibf2[0];

    icf2[0]=(C1*(((A1*ic+B1*icf2[1])>>15)+2*ic+5*icf2[1]-icf2[2]))>>15;
```

```
        icf2[2]=icf2[1];
        icf2[1]=icf2[0];

        vabf2[0]=(C1*(((A1*vab[0]+B1*vabf2[1])>>15)+2*vab[0]+5*vabf2[1]
                -vabf2[2]))>>15;
        vabf2[2]=vabf2[1];
        vabf2[1]=vabf2[0];

        vbcf2[0]=(C1*(((A1*vbc[0]+B1*vbcf2[1])>>15)+2*vbc[0]+5*vbcf2[1]
                -vbcf2[2]))>>15;
        vbcf2[2]=vbcf2[1];
        vbcf2[1]=vbcf2[0];

//Two-Phase PLL
        valfa=vabf2[0];
        vbeta=((int32)(vabf2[0]+(2*vbcf2[0]))*18919)>>15;
        thida_err=((valfa*(int32)yo)>>15)+((vbeta*(int32)xo)>>15);

// PI controller for thida_err
        qth[0]=qth[1]+(thida_err*((Ki_th*70)>>12)>>10);
        Uth=((thida_err*Kp_th)+qth[0])>>10;

        if (Uth<0)
            step=0;
            else if (Uth>16384)
            step=16384;
            else
            {
               step=Uth;      //step is in Q11 format
               qth[1]=qth[0];
               }

        if (qth[0]>16777216)
            {
              qth[0]=0;
              qth[1]=0;
            }
```

```
   stepf[0]=((int32)A2*step>>15)+((int32)B2*stepf[1]>>15);
   stepf[1]=stepf[0];

step_count=step_count+stepf[0];

xo_p=step_count>>11;
if (xo_p>2047)
      {
      step_count=step_count-4194304;
      xo_p=xo_p-2048;
      }

yo_p=xo_p+512;
if (yo_p>2047)
    yo_p=yo_p-2048;

xo=SinTable[xo_p];
yo=SinTable[yo_p];

sin_p=xo_p+1877;
if (sin_p>2047)
    sin_p=sin_p-2048;

cos_p=xo_p+341;
if (cos_p>2047)
    cos_p=cos_p-2048;

sinwt=SinTable[sin_p];
coswt=SinTable[cos_p];

   thida_a=sin_p;
   thida_b=sin_p+1365;
   if (thida_b>2047)
   thida_b=thida_b-2048;

   thida_c=sin_p+683;
   if (thida_c>2047)
   thida_c=thida_c-2048;
```

```
        thida_Da=sin_p+2048-thida_Dm;
        if (thida_Da>2047)
           thida_Da=thida_Da-2048;

        thida_Db=sin_p+1365-thida_Dm;
        if (thida_Db>2047)
           thida_Db=thida_Db-2048;

        thida_Dc=sin_p+683-thida_Dm;
        if (thida_Dc>2047)
           thida_Dc=thida_Dc-2048;

//DQ Transformation ia ib => id iq for obtaining Im
        ialfa=iaf2[0];
        ibeta=((int32)(ibf2[0]-icf2[0])*18919)>>15;

        id[0]=(((int32)ialfa*coswt)+((int32)ibeta*sinwt))>>15;
        iq[0]=(((int32)ibeta*coswt)-((int32)ialfa*sinwt))>>15;

        Im=-iq[0];    //Im is in Q11 format

        Imf2[0]=(C3*(((A3*Im+B3*Imf2[1])>>15)+2*Imf2[1]-Imf2[2]))>>15;
        Imf2[2]=Imf2[1];
        Imf2[1]=Imf2[0];

// Rotor frequency calculation
        count2=count2+1;
        temp1=temp1+(((int32)step*25000)>>11);
        if (count2==2048)
           {
            count2=0;
            Fe=temp1>>22;
            temp1=0;
           }

        count3=count3+1;
        wmsum=wmsum+(((int32)step*25000)>>11);
```

```
        if (count3==150)
          {
           count3=0;
           wm=wmsum/150;    // Averged value of 32 times 2^5
              wm=wm*3217>>12;
              wm=wm>>7; //per unit to 128 rad/s(with Q12 operation) in Q11
              wmsum=0;
            }

//Mode Detector

      section=thida_a/342;

//Optimal Torque(Current) Controller

      if (section==0)
        {
          if (M2count<=Nt)
               DCM();
               else
                  CCM();
      }
      else if (section==1)
           DCM();
      else if (section==2)
        {
            if (M2count<=Nt)
                DCM();
                else
                   CCM();
        }
      else if (section==3)
          DCM();
      else if (section==4)
        {
            if (M2count<=Nt)
                DCM();
                else
```

```
                    CCM();
            }
          else if (section==5)
              DCM();


//Vw command calculator

      vw=650+((int32)120*SinTable[f1p]>>15)+((int32)120*SinTable[f2p]>>15);

//Output the data to DAC Board

      *DA_Porta=(iaf2[0]>>3)+2048;
      *DA_Portb=(ea>>3)+2048;
      *DA_Portc=iam+2048;
      *DA_Portd=vw;
      EvaRegs.EVAIFRA.all = 0xFFFF;
      PieCtrlRegs.PIEACK.all = PIEACK_GROUP2;
      EINT;     // Enable Global interrupt INTM
      ERTM;    // Enable Global realtime interrupt DBGM
      return;

}


void init_eva_timer1(void)
{
      EvaRegs.GPTCONA.all = 0;

      EvaRegs.T1PR = 1250;            // Period CLK=75MHz
      EvaRegs.T1CMPR = 0x0000;        // Compare Reg

      EvaRegs.EVAIMRA.bit.T1UFINT = 1;
      EvaRegs.EVAIFRA.bit.T1UFINT = 1;
      EvaRegs.T1CNT = 0x0000;
      EvaRegs.T1CON.all = 0x104A;

      EvaRegs.GPTCONA.bit.T1TOADC = 2;
```

```
    EvaRegs.ACTRA.all = 0x0666;
    EvaRegs.DBTCONA.all = 0x0102; // Setup the deadtime
    EvaRegs.COMCONA.all = 0xA600;
}

void CCM(void)
{
    sinwt_b=SinTable[thida_b];
    sinwt_c=SinTable[thida_c];

    sin_da=SinTable[thida_Da];
    sin_db=SinTable[thida_Db];
    sin_dc=SinTable[thida_Dc];

    iam=((int32)Imc*sinwt)>>15;
    ibm=((int32)Imc*sinwt_b)>>15;
    icm=((int32)Imc*sinwt_c)>>15;


    if (thida_a<1024)
    {

        iae[0]=iam-iaf2[0];

        if (Rcounta==0)
        {
            Avgiae[0]=Sumiae/8;
            ea=Avgiae[0]-Avgiae[1];
            ya[0]=((((Kr*a0)*ea)-(b1s*ya[1])+(b2s*ya[2]))>>21)+(2*ya[1])-ya[2];
            ya[2]=ya[1];
            ya[1]=ya[0];
            Avgiae[1]=Avgiae[0];
            Sumiae=0;
        }

        Sumiae=Sumiae+iae[0];
        Rcounta=Rcounta+1;
```

```
    if (Rcounta==8)
    {
        Rcounta=0;
    }

    Da=((int32)sin_da*Dm)>>15;
    ma=(((int32)iae[0]*Kp_c)>>12)+Da;//+ya[0];

}
else
{
    Ua=-626;
    Roffa();
}

if (thida_b<1024)
{
    ibe[0]=ibm-ibf2[0];

    if (Rcountb==0)
    {
        Avgibe[0]=Sumibe/8;
        eb=Avgibe[0]-Avgibe[1];
        yb[0]=((((Kr*a0)*eb)-(b1s*yb[1])+(b2s*yb[2]))>>21)+(2*yb[1])-yb[2];
        yb[2]=yb[1];
        yb[1]=yb[0];
        Avgibe[1]=Avgibe[0];
        Sumibe=0;
    }

    Sumibe=Sumibe+ibe[0];
    Rcountb=Rcountb+1;

    if (Rcountb==8)
    {
        Rcountb=0;
    }
```

```
    Db=((int32)sin_db*Dm)>>15;
    mb=(((int32)ibe[0]*Kp_c)>>12)+Db;//+yb[0];

}
else
{
    Ub=-626;
    Roffb();
}

if (thida_c<1024)
{
    ice[0]=icm-icf2[0];

    if (Rcountc==0)
    {
        Avgice[0]=Sumice/8;
        ec=Avgice[0]-Avgice[1];
        yc[0]=((((Kr*a0)*ec)-(b1s*yc[1])+(b2s*yc[2]))>>21)+(2*yc[1])-yc[2];
        yc[2]=yc[1];
        yc[1]=yc[0];
        Avgice[1]=Avgice[0];
        Sumice=0;
    }

    Sumice=Sumice+ice[0];
    Rcountc=Rcountc+1;

    if (Rcountc==8)
    {
        Rcountc=0;
    }

    Dc=((int32)sin_dc*Dm)>>15;
    mc=(((int32)ice[0]*Kp_c)>>12)+Dc;//+yc[0];

}
else
```

```
{
    Uc=-626;
    Roffc();
}

if (section==0)
{
    Ua=((int32)(2*ma+mc)*1250)>>12;
    Ua=1250-Ua;
    Uc=((int32)(ma+2*mc)*1250)>>12;
    Uc=1250-Uc;
}

if (section==2)
{
    Ua=((int32)(2*ma+mb)*1250)>>12;
    Ua=1250-Ua;
    Ub=((int32)(ma+2*mb)*1250)>>12;
    Ub=1250-Ub;
}

if (section==4)
{
    Ub=((int32)(2*mb+mc)*1250)>>12;
    Ub=1250-Ub;
    Uc=((int32)(mb+2*mc)*1250)>>12;
    Uc=1250-Uc;
}

if (Ua<0)      //limiter for duty ratio
    m1=0;
    else if (Ua>1250)
    m1=1250;
    else
    m1=Ua;

if (Ub<0)
    m2=0;
```

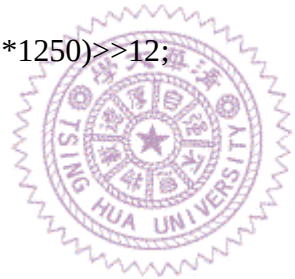

```
        else if (Ub>1250)
        m2=1250;
        else
        m2=Ub;

    if (Uc<0)
        m3=0;
        else if (Uc>1250)
        m3=1250;
        else
        m3=Uc;


    EvaRegs.CMPR1=m1;
    EvaRegs.CMPR2=m2;
    EvaRegs.CMPR3=m3;
}

void DCM(void)
{
    Roffa();
    Roffb();
    Roffc();

    iam=((int32)Imc*sinwt)>>15;

    if (M2count==1)
    {
        //Current PI controller Ts=1/10000 in Q19
        Ie=Imc-Imf2[0];

        d1max=(Imf2[0]*2)+1500;
        if (d1max>7000)
            d1max=7000;

        qi[0]=qi[1]+(Ie*((Ki_i*70)>>12)>>10);

        Ui=((((int32)Ie*Kp_i)+qi[0])>>12);
```

```
    Ui=((int32)Ui*7500)>>12;

    if (Ui<0)
        d1=0;
        else if (Ui>d1max)
        d1=d1max;
        else
        {
            d1=Ui;
            qi[1]=qi[0];
        }

    if (qi[1]>46080000)
        qi[1]=0;

    N=d1/1250;
    M=d1-(1250*N);
    Nt=d1/2500;
}

if (M2count<=N)
{
    EvaRegs.CMPR1=1251;
    EvaRegs.CMPR2=1251;
    EvaRegs.CMPR3=1251;
}

if (M2count==(N+1))
{
    EvaRegs.CMPR1=M;
    EvaRegs.CMPR2=M;
    EvaRegs.CMPR3=M;
}

if (M2count>(N+1))
{
    EvaRegs.CMPR1=0;
    EvaRegs.CMPR2=0;
```

```
        EvaRegs.CMPR3=0;
    }

    M2count=M2count+1;

    if (M2count>6)
        M2count=1;
}

void Roffa(void)
{

    if (Rcounta==0)
    {
        Avgiae[1]=0;
        Avgiae[0]=0;
        ya[0]=(((b2s*ya[2])-(b1s*ya[1]))>>21)+(2*ya[1])-ya[2];
        ya[2]=ya[1];
        ya[1]=ya[0];
    }

    Rcounta=Rcounta+1;

    if (Rcounta==8)
    {
        Rcounta=0;
    }
}

void Roffb(void)
{

    if (Rcountb==0)
    {
        Avgibe[1]=0;
        Avgibe[0]=0;
        yb[0]=(((b2s*yb[2])-(b1s*yb[1]))>>21)+(2*yb[1])-yb[2];
        yb[2]=yb[1];
```

```
        yb[1]=yb[0];
    }

    Rcountb=Rcountb+1;

    if (Rcountb==8)
    {
        Rcountb=0;
    }
}
void Roffc(void)
{

    if (Rcountc==0)
    {
        Avgice[1]=0;
        Avgice[0]=0;
        yc[0]=(((b2s*yc[2])-(b1s*yc[1]))>>21)+(2*yc[1])-yc[2];
        yc[2]=yc[1];
        yc[1]=yc[0];
    }

    Rcountc=Rcountc+1;

    if (Rcountc==8)
    {
        Rcountc=0;
    }
}
```